Alma Mater Studiorum – Università di Bologna

DOTTORATO DI RICERCA IN

Chimica

Ciclo XXIX

Settore Concorsuale di afferenza: 03/A2

Settore Scientifico disciplinare: CHIM02

Beyond the rigid static models for liquid crystals: Flexible or active particles

Presentata da: **Renato Ferreira de Souza**

Coordinatore Dottorato

Prof. Aldo Roda

Relatore

Prof. Claudio Zannoni

Esame finale anno 2017

Acknowledgments

I am very thankful to many people that helped me during this journey. I would like to start thanking my family, which were always present.

I would like to thank all my friends: Italo, Dani, Natalia, Eduardo, Pomodoro, Otello, Mattia, Matteo, Lara, Mulla, Isa, and Silvia. I am very grateful for all of you for the acceptance, it was due to you that i didn't feel alone in foreign lands. An special thanks to Silvia, Lara and Otello for reviewing my manuscript.

I would like to thank Prof. Zannoni for the guidance, stimulating discussions and mainly for the patience.

I'm also very thankful to Prof. Evangelista for all the mentoring, teachings and support.

I would like to thank CAPES foundation for the financial support.

Abstract

In the present work we study the dynamics of non-rigid or of active particles dispersed in liquid crystals. This is important to develop the theoretical tools needed to interpret experimental data from a variety of techniques, such as fluorescence depolarization and magnetic resonance.

In the first part of the thesis the dynamics of non-rigid particles is studied in the roto-diffusional framework, where the particle movements are described by a random walk in an anisotropic medium. The interaction between the solvated particles and the liquid crystal host is handled through an effective field potential, which is, in turn, shape dependent. This treatment allowed us to develop expressions to calculate any time correlation function related to changes in shape and/or orientation. We expect that the availability of this framework will provide an incentive for the development of experimental techniques in this field.

Until a few years ago the study of particles dispersed in liquid crystals was confined to inert ones, whose time evolution was determined by some sort of anisotropic stochastic motion. However, a fascinating new class of systems, where the particles can be in addition self propelled has recently became of great interest. These systems of active particles can give rise to new non equilibrium organizations corresponding to well defined stationary states, stable as long as the propelling of the active particles is maintained. Most of the studies available until now on these unconventional liquid crystals have been of the continuum, hydrodynamic type, while here we have been interested in developing a microscopic, molecular level, approach. Thus, in the second part of the thesis, a study of active particles suspended in a liquid crystal host, formed from normal non active mesogens, was performed using molecular dynamics simulations. We modelled both type of particles as uniaxial ellipsoids interacting with a Gay-Berne potential. The distinction between active and passive particles is done by adding a propelling non conservative force to the equation of motion of the former. We found that the long range order of the liquid crystals host can induce the self assembly of active particles in lanes, clusters of particles flowing in the same direction. We also showed that the thermal energy added by the active particles increases the sample temperature, which in turn reduce the orientational order of the

host. In particular no laning is obtained from active particles in an isotropic host.

Contents

1 Introduction **1**

1.1 Liquid Crystals 1

1.2 Shape changing particles 4

1.3 Active matter 5

1.4 Outline of the thesis 8

I Rotational-Diffusion of Shape Switching particles **9**

2 The Rotational-Diffusion problem **10**

2.1 Experimental observables 12

2.2 Correlation Functions 13

2.3 Evolution operator 21

3 Uniaxial particles in uniaxial nematic liquid crystals **25**

3.1 Evolution equation 26

3.2 Numerical formulation 29

3.3 Estimating the shape dependence of the diffusion coefficients and of the effective field potential 32

3.4 Results 35

4 Uniaxial particles dispersed in biaxial liquid crystals **40**

4.1 Evolution Operator 41

4.2 Eigenfunction expansion 43

4.2.1 Shape change operator 47

4.2.2 Roto-diffusion operator 52

4.3 Numerical Implementation details 56
4.4 Model parameters 58
4.5 Results 59

II Active particles **69**

5 Introduction to Molecular Dynamics Simulations **70**
5.1 Molecular Dynamics Simulations 72
5.2 Modelling rigid particles 75
5.3 Interaction with an external reservoir 80
5.3.1 Interaction Potential 82
5.3.2 Self Propelling Force 88
5.4 Integration of the equations of motion 89

6 Simulations of Active particles suspended in liquid crystals **93**
6.1 Model parameters 94
6.2 Sample preparation 95
6.3 Results 97
6.3.1 Aggregation of self-propelled particles 97
6.3.2 Ordering and activity 104

7 Concluding Remarks **110**
7.1 Shape Changing particles 110
7.2 Active particles 111

A Clustering with DBSCAN **113**

References **117**

Chapter 1

Introduction

1.1 Liquid Crystals

Liquid crystals (LC) are a class of intermediate phases of matter between solid crystals, that possess three dimensional positional order as well as orientational long range order, and isotropic liquids which lack both. Liquid crystals phases exhibit instead orientational order and no positional order (nematics) or reduced one dimensional order (smectics). Nematics can flow like liquids, but their constituents particles have their axis aligned on average along a common direction, the director. More importantly, the alignment direction is usually maintained for lengths much larger than inter-particle distances. As a consequence, a series of phenomena connected to the molecular organization anisotropy typically observed in crystalline solids, are also observed in liquid crystals [1]. However, differently from them, in liquid crystals these properties can be controlled by externals perturbations, for example, electric or magnetic fields, but also surface forces or flow. These characteristics make LC very versatile materials with diverse kind of applications, ranging from the ubiquitous LC displays to biological sensors [2]. A sketch of the particles organization in a liquid crystal, a crystalline solid and a isotropic liquid is shown in Fig. 1.1.

The sub-classes of liquid crystals phases are classified by the type and degree of ordering, geometry of their constituents and by the features responsible for their phase transition. For example, liquid crystals formed by elongated rods are named calamitic, while the ones formed by flat disks-like molecules are named discotic. In the classification based on the phase transition, there are two main groups: ther-

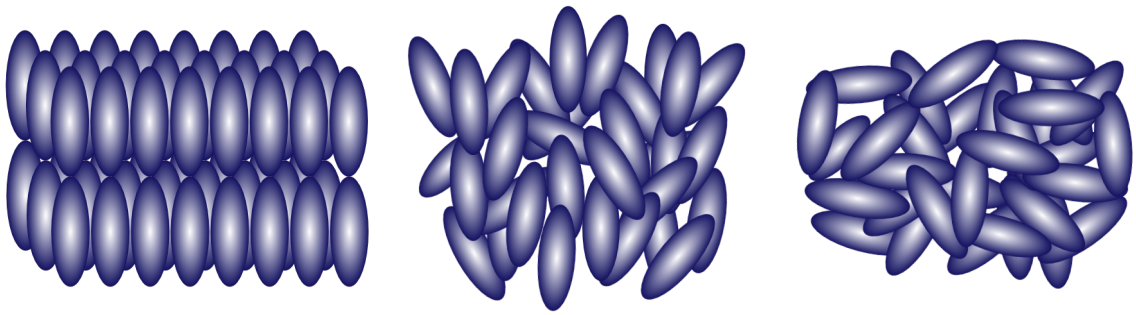

(a) **(b)** **(c)**

Figure 1.1: Sketch of the constituents organization of the phases (a) solid crystalline, (b) liquid crystalline and (c) isotropic liquid. In the sketches, each ellipsoid represents a particle forming the phase.

motropics, where the phase transitions take place due to a change in temperature and lyotropics solute-solvent systems, where the phase transitions are caused by a variation in the concentration of the mixture.

The main groups in terms of ordering category are (as already mentioned) the nematics and smectics. In nematics, the centre of mass of the particles forming the phase are distributed as in a fluid, however the particles are aligned over domains of a few hundreds nm along a common direction. Furthermore, the application of a weak external field (e.g. electric field $\sim 1V/\mu m$ or magnetic field $\sim 1T$) can easily align the domains and form a uniformly aligned sample. We can further subdivide nematics by the number of preferred directions. Systems with just one preferential orientation (the usual case) are named uniaxial nematics while systems possessing a preferential orientation also around a secondary, transversal, axis are called biaxial nematics.

The smectic phases posses essentially the same kind of orientational order present in nematics, but their defining feature is to also have some type of positional order. Indeed the particles forming a smectic phase are organized in layers, which are approximately equally spaced and parallel. The sub-divisions of smectics is based first on the tilt angle between the director and the layer normal (e.g. smectic A and smectic B have the director perpendicular to the layer and smectic C have it tilted). The second element of classification for smectics is the positional order inside the layers (none for smectic A and hexagonal for smectic B). A sketch illustrating the similarities and differences between nematics and smectics is shown in Fig. 1.2.

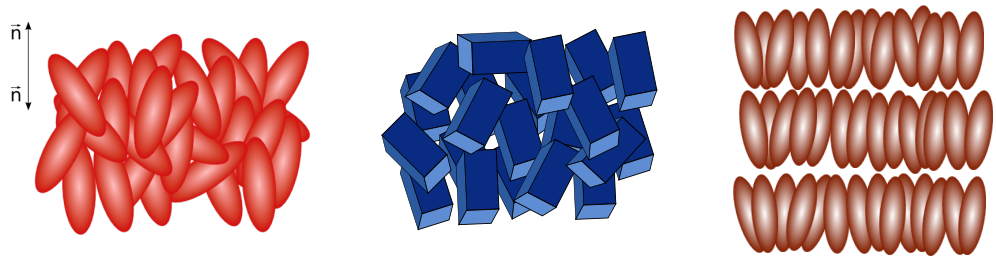

(a) **(b)** **(c)**

Figure 1.2: Representation of the liquid crystals phases: (a) uniaxial nematic, (b) biaxial nematic and (c) smectic A. In the sketches the ellipsoids represents uniaxial constituents, while the boxes represents biaxial ones.

The microscopic description of a nematic phase requires in general the specification of the preferential alignment direction, $\hat{\mathbf{n}}$, and of the probability distribution $P(\hat{\mathbf{n}}\cdot\hat{\mathbf{u}})$ of finding the axis of a molecule, $\hat{\mathbf{u}}$, assumed to be rod-like for simplicity, at a certain orientation from the director. As the distribution is normally not available to be determined in full from experiments, the orientational order can be quantified using the first few moments of the probability distribution. The simplest and more common order parameter is obtained from just the first non vanishing moment of the distribution, the second one $\langle(\hat{\mathbf{n}}\cdot\hat{\mathbf{u}})^2\rangle$, as

$$\langle P_2\rangle = \langle P_2(\hat{\mathbf{n}}\cdot\hat{\mathbf{u}}\rangle = \frac{1}{2}\langle 3(\hat{\mathbf{n}}\cdot\hat{\mathbf{u}})^2 - 1\rangle \tag{1.1}$$

where $P_2 \equiv P_2(\cos\beta)$ is the second Legendre polynomial and the angular brackets indicate an average over all particles. Notice that $\langle P_2\rangle$ is one for complete order and goes to zero in the isotropic phase. One of the most interesting features of liquid crystals is that guest particles dissolved in them tend to follow the ordering present in the phase. For example, particles dissolved in nematics tends to align along the same direction as the host. This property has long been used in technological applications, e.g. one of the first display prototypes, dating back from 1968, was based on the reorientation of dye molecules doping a nematic liquid crystal [3]. Nowadays, liquid crystals materials are being applied as tunable solvents. The possibility of easily varying their orientational order is then being used to organize synthetic and biological suspensions [2,4,5]. Furthermore, their average orientational direction can also

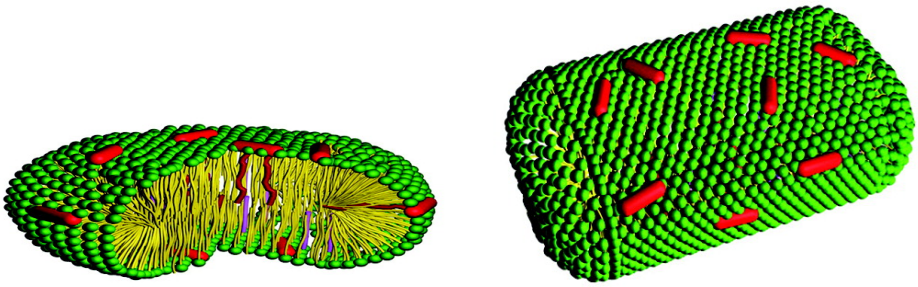

Figure 1.3: Representation of micelles formed by amphiphilic molecules. Adapted with permission from Qingkun Liu; Corinne Beier; Julian Evans; Taewoo Lee; Sailing He; Ivan I. Smalyukh; Langmuir 2011, 27, 7446-7452. Copyright 2011 American Chemical Society

be used to guide *self-propelled* particles and living micro organism [6, 7].

1.2 Shape changing particles

The assumption nearly invariable made in modelling the orientational order and the dynamics of LC mesogens as well as of particles suspended in ordered phases is that of assuming them to be rigid uniaxial or biaxial objects. While this is a very successful simplification in a number of cases, it is clearly inadequate to treat two classes of problems that we wish to investigate in this thesis. The first is the case of particles hosted in anisotropic solvents, that rather than maintaining the same rigid shape while reorienting, can actually change from a shape to another. In practice this can be appropriate for a variety of systems. For instance, anisotropic micelles whose overall, envelope, shape is the result of the aggregation of a number of flexible amphiphilic molecules [8](see Fig. 1.3) or temperature responsive gel micro-particles [9, 10] (see Fig. 1.4).

Here we developed the theory needed to describe various limiting cases of particles of uniaxial ellipsoidal shape that can switch from an elongated to spherical to oblate aspect ratio, while reorienting in a uniaxial or biaxial LC host.

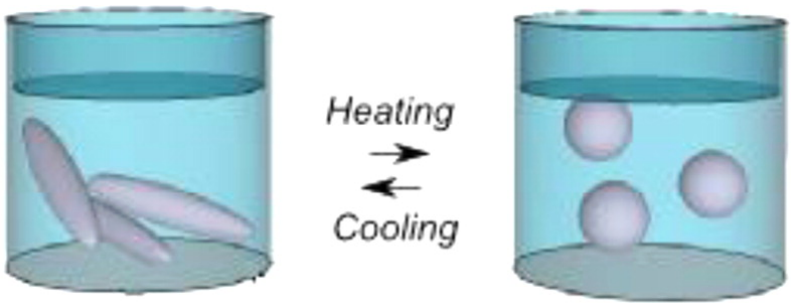

(a)

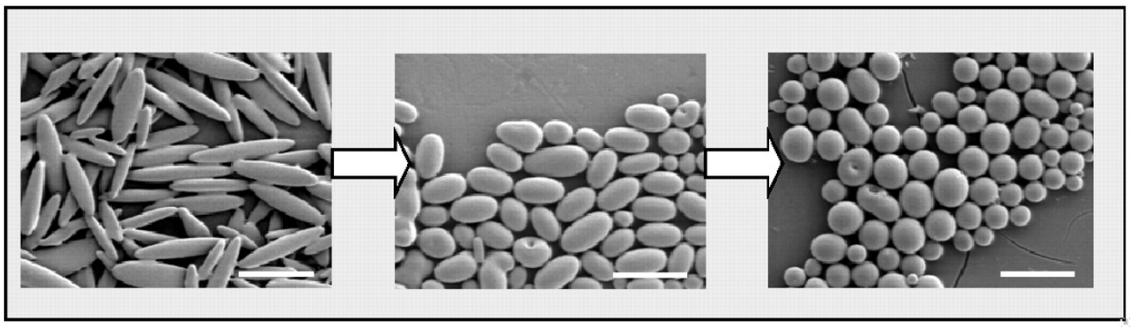

(b)

Figure 1.4: Example of non-rigid temperature responsive micro-particles . (a) Liquid crystals elastomers which change shape in response to variation in the environment temperature. (b) PLGA particles that change shape in response to temperature and environment PH. Figure (a) was reprinted with permission from Jean E. Marshall; Sarah Gallagher; Eugene M. Terentjev; Stoyan K. Smoukov; J. Am. Chem. Soc. 2014, 136, 474-479. Copyright 2013 American Chemical Society and figure (b) was reprinted with permission from [9].

1.3 Active matter

Apart from rigidity another assumption normally made on particles embedded in a LC solvent is that they are passive, I.e. not capable of autonomous propulsion. However there are system, named active system, whose components can extract energy from external sources and convert it into motion. This general definition comprises a wide range of systems with length scales varying from nano to macroscopic. For instance, groups of living beings such as bacterial suspensions, schools of fish and flocks of birds fit well into this category, but so also do synthetic particles like certain Janus colloids, motor driven cytoskeletal filaments and shaken granular rods.

The source of activity has very different origins and forms for each specific system. In living matter, it usually comes from the consumption of some kind of food. For example fishes or birds extract energy needed for movement from the food consumed, or in bacterial suspensions the energy source comes from the consumption

of ATP [6]. In the synthetic counterpart, the mechanism of conversion is more intricate. For example, Janus particles can be endowed with different chemical affinities on the two hemispheres [11](see Fig. 1.5). When they are illuminated by a source of light, a reaction is induced in just one of its poles. In another example platinum is deposited on one of the Janus faces and this, when the particles are immersed in H_2O_2 act as a catalytic agent for a chemical reaction generating oxygen. This reaction, in turn, produces a flow of matter which propels the particles forward. In a system of granular rods, the vibrations of its container shakes the particles, putting them in motion [12].

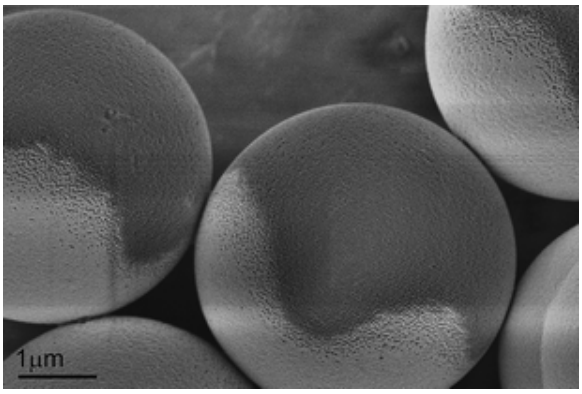

(a)

Figure 1.5: SEM image of silanated silica particles (one type of Janus particles) showing that one of its pole its is coated with gold. reproduced with permissions from [11].

Even though active matter comprises a huge set of different systems, some unifying characteristic can still be identified. Due to the presence of non -conservative interactions, these system are intrinsically out of equilibrium. Moreover, the balance between the interactions with the environment and the system activity can generate coherent movement, which in turn can organize the system in various sorts of ordered structures. For instance, schools of fish assembly themselves in flocks with polar order, while the granular rods can show nematic order [13](see Fig. 1.6) .

Besides the orientational ordering, active particles can also show positional organization, for example, Janus particles can organize themselves in clusters when illuminated by light [14] (i.e. see Fig. 1.7), while schools of fish can organizes themselves in "lanes".

In systems of this type a problem of great interest that we shall tackle here, is to

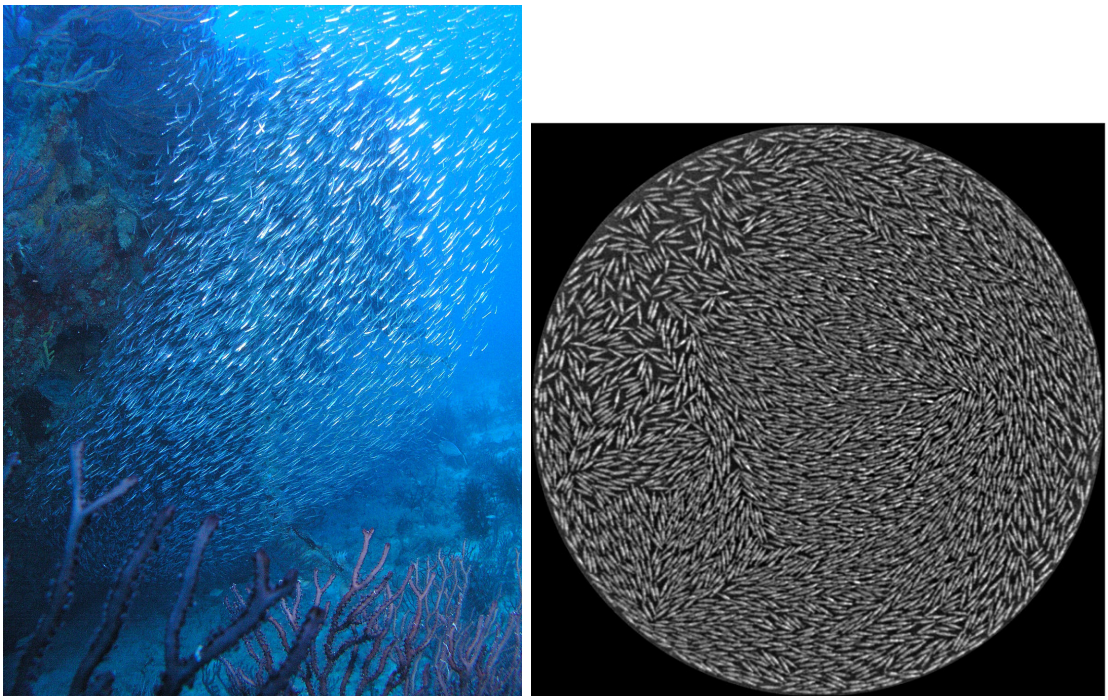

(a) (b)

Figure 1.6: Examples of orientational ordering formed in active system. In figure (a) a school of fishes organizes in polar order, while in (b) a system of shaken granular rods are organized with polar order. Photo (a) taken by Matthew Hoelscher (Flickr) and Figure (b) was reprinted from ref. [13].

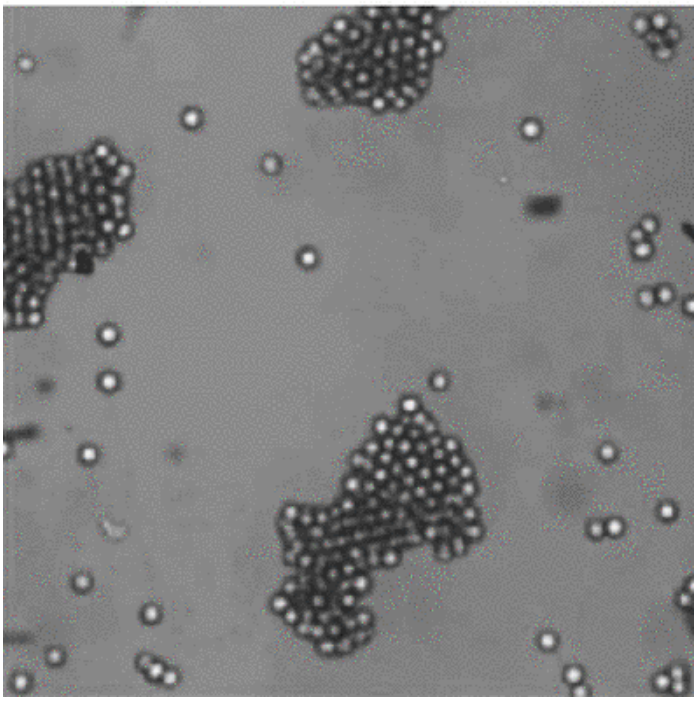

Figure 1.7: Aggregation of Janus particles in clusters. Figure reproduced with permissions from [14].

examine the possibility of novel non-equilibrium ordered organization which can be stable as long as the external energy lasts.

1.4 Outline of the thesis

As already mentioned the present thesis is divided in two parts. In the first part we study the rotational-diffusion of shape switching particles suspended in nematic liquid crystal environments. In chapter 2, we develop the theoretical framework to study the rotational-diffusion of a shape changing particle in nematic environments. We apply the framework to study the dynamics of a uniaxial particle solvated in an uniaxial solvent in chapter 3, and to study uniaxial particles solvated in a biaxial nematic in chapter 4.

In the second part, we used molecular dynamics simulations to study active particles suspended in liquid crystals phases. In chapter 5 we review the techniques of molecular dynamics, which in turn are used in chapter 6 to study the active particles suspended in smectic and nematic liquid crystals phases with different degree of ordering.

Part I

Rotational-Diffusion of Shape Switching particles

Chapter 2

The Rotational-Diffusion problem

The interpretation of a variety of experimental results dealing with the dynamics of molecules, proteins, or colloidal nanoparticles in liquids, liquid crystals, membranes, or soft polymers relies on assuming some model for the reorientation of the particle in its environment [15–18]. Classical assumptions are that reorientation takes place according to some kind of Markov process by small angular displacements or alternatively by large uncorrelated jumps, the so-called strong collision model [19]. In the first case, the stochastic evolution equation for the conditional probability $P(\Omega_0|\Omega,t)$ of finding the particle, assumed to be rigid, at a certain orientation Ω at time t if it was at Ω_0 at time t_0 (as illustrated in Fig. 2.1), can be written as a "local in space", differential equation describing a rotational diffusion process. If the process occurs with finite orientational jumps, a first order kinetic equation with a transition matrix giving the probability of leaping from one state to another can be set up.

The rotational diffusion problem has been treated in detail in what are now clas-

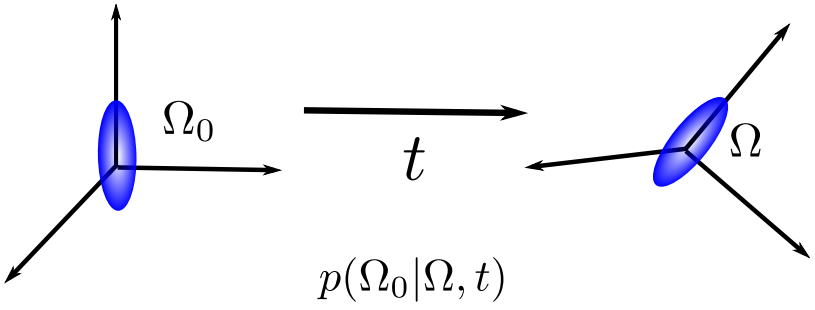

Figure 2.1: Conditional probability $P(\Omega_0|\Omega,t)$

sical papers for liquids [20, 21] and liquid crystals [19]. The procedure, assuming that the motion of the particle whose evolution is followed, takes place in an effective mean field potential describing the overall effect of the anisotropic solvent, e.g. a liquid crystal or a membrane bilayer, has been pioneered by Nordio et al. [19, 22] and Freed et al. [23, 24] who dealt with uniaxial molecules reorienting in a uniaxial solvent. This approach has been widely used to interpret results from Electron Spin Resonance (ESR) [22, 23, 25], Dielectric Relaxation [22], Fluorescence Depolarization [26] etc. Generalizations applicable to uniaxial particles reorienting in a biaxial nematic [27] or to molecules of arbitrary symmetry reorienting in a uniaxial [28] or biaxial [29] phase have also been put forward. A variety of experimental observables for biaxial molecules dissolved in liquid crystals, ranging from Nuclear Magnetic Resonance spectral densities [30,31] to Fluorescence Polarized intensities [32], have been interpreted using this approach, allowing the determination of the molecular rotational diffusion tensor components and correlation times. The determination of diffusion coefficients for other systems, e.g. macromolecules, can also be obtained by other optical techniques like Fluorescence Correlation Spectroscopy [33, 34].

It is important to stress that all the theories and applications mentioned concern rigid molecules, or rather molecules that can be approximated with rigid particles, where a centre of mass and a Cartesian frame can be rigorously defined. On the other hand, there are various important problems that defy this simplification. One classical molecular example is that of internal conformational motions being important [35, 36], for instance due to the presence of flexible alkyl chains or other internal mobile moieties [36]. More generally, this happens for many macromolecules, for proteins [37] and polymers [9], but also for deformable vesicles [38, 39], gel particles [40, 41] and red blood cells [42, 43]. Recently, the rigid particle rotational model was extended to include non-conserving shape dynamics but with a theory that is applicable only to particles dissolved in an isotropic environment [44, 45].

In this chapter we develop a theoretical framework suitable for studying the dynamics of soft particles that can switch shape while tumbling. These could be for instance micro- or nano-size gel particles that can change from an elongated to a discoidal shape while embedded in a nematic. We do not discuss here the origin of the shape change in details, but possible mechanisms could be spontaneous fluc-

tuations, taking place in a particle or a micelle with some internal core structure or even fluctuations driven by some external event. For instance, we could imagine micro-particles formed by a liquid crystal elastomer [46] containing photosensitive azobenzene moieties [47, 48] that can change their shape following a more or less random sequence of UV light bursts.

2.1 Experimental observables

We will study the effect of the complex motion of a non-rigid particle on correlation functions and correlation times and, as far as possible, try to present our results in a way suitable for future comparison with experiments (e.g. NMR or Fluorescence Depolarization). Indeed, even if we are currently not aware of experimental data for shape switching particles in anisotropic environments, we expect these to become available, e.g. for proteins in membranes, extending the work presented by various groups on isotropic environments [44, 45].

The measurements of observable dynamical quantities are performed in the laboratory frame H, although the equations can be expressed more conveniently in the particle fixed frame P. According to linear response theory, dynamic observables can normally be written in term of correlation functions between some properties of system [49], which we can generically call $\mathbf{A}$ and $\mathbf{B}$, at different times:

$$C_{AB}(t) = \langle \mathbf{A}_H(0)\mathbf{B}^*_H(t)\rangle, \tag{2.1}$$

where the angular brackets indicate an average over time.

According to the model just described which assumes the particle to switch between "rigid for a while" shapes, we can consider $\mathbf{A}$ and $\mathbf{B}$ for each shape as tensor properties, that we further write in their spherical representations [50] in the lab frame as $A^{L,m}_H$, $B^{L,m\,*}_H$, where L is the tensor rank of the property and m a specific component. We can then write the spherical components in the lab frame in terms of

those in the particle fixed frame as

$$\begin{aligned}&\langle A_H^{L,m}(0) B_H^{L',m'\,*}(t)\rangle \\ &= \sum_{n,n'} \langle D_{m,n}^{L\,*}(\Omega_0) D_{m',n'}^{L'}(\Omega) A_P^{L,n}(\chi_0) B_P^{L',n'\,*}(\chi_t)\rangle \end{aligned} \tag{2.2}$$

where $D_{m,n}^{L}(\Omega_t) \equiv D_{m,n}^{L}(\Omega_{P(t)-H})$ are Wigner rotation matrices and $\Omega = (\alpha, \beta, \gamma)$ represents the set of three Euler angles giving the orientation of the particle starting from the laboratory frame [50]. We notice that the components $A_P^{L,n}$, $B_P^{L',n'}$ cannot be brought outside the average, as for rigid molecules, since they are still changing with time as the particles shape switches.

The number of relevant correlation functions depends on the symmetry of the probe particle and of the anisotropic solvent studied. In this thesis, we study the process under different symmetries for the host and the "solute" particles.

2.2 Correlation Functions

Even though the full calculation of the particle motions involved in processes like the ones specified in Eq. (2.2) is possible in principle, e.g. from fully atomistic molecular dynamics simulations, practical applications require a different approach. Here we will treat the problem within a probabilistic framework.

Stochastic processes are described by a set of variables $\mathbf{x} = \{x_0, x_1, \ldots, x_n\}$ whose values are taken randomly from a probability distribution $P(\mathbf{x}, t)$. The variables x_i can be any physical parameter, for example, the 3 coordinates of the centre of mass of a particle. Since we are studying dynamic processes, the probability distribution for one or more variables will generally change with time t.

Processes specified for the Eq. (2.2) require not only the probability of finding a stochastic variable at a certain time, but also the probability of finding it other values later. To take this into consideration, we define the joint probability $W_n(\mathbf{x}^0, t_0; \ldots; \mathbf{x}^n, t_n)$ as the probability of finding $\mathbf{x}$ at $\mathbf{x}^0$ at time t_0, $\mathbf{x}^1$ at time t_1 and further until $\mathbf{x}^n$ at t_n.

The joint probability possess the properties of being always positive [51]:

$$W_n(\mathbf{x}^0, t_0; \ldots; \mathbf{x}^n, t_n) \geq 0 \quad \forall \quad \mathbf{x}^0, \ldots, \mathbf{x}^n, \tag{2.3}$$

normalized

$$\int\int \ldots \int W_n(\mathbf{x}^0, t_0; \ldots; \mathbf{x}^n, t_n) d\mathbf{x}^0 \ldots \mathbf{x}^n = 1 \tag{2.4}$$

and reducible

$$W_{n-1}(\mathbf{x}^0, t_0; \ldots; \mathbf{x}^{n-1}, t_{n-1}) = \int W_n(\mathbf{x}^0, t_0; \ldots; \mathbf{x}^n, t_n) d\mathbf{x}^n, \tag{2.5}$$

here we integrated over the last term $\mathbf{x}^n$ for simplicity, but the reduction can be performed over any stochastic variable $\mathbf{x}^i$. As a consequence, with the knowledge of $W_n(\mathbf{x}^0, t_0; \ldots; \mathbf{x}^n, t_n)$ we can recover any lower distribution desired applying the rule in Eq. (2.5) repeatedly. Moreover, knowing $W_n(\mathbf{x}^0, t_0; \ldots; \mathbf{x}^n, t_n)$ allows us to calculate any time correlation function involving the stochastic variables $\mathbf{x}$. Suppose $Y(\mathbf{x}^t)$ is a function that depends only on the values $\mathbf{x}^t$; here we used the superscript t to indicate that $\mathbf{x}$ is taken at some time t, therefore, Y depends implicit on t. We can calculate any time correlation function of property Y with the equation

$$\langle Y(t_0) Y(t_1) \ldots Y(t_n) \rangle = \int\int \cdots \int W_n(\mathbf{x}^0, t_0; \ldots; \mathbf{x}^n, t_n) Y(\mathbf{x}^0) Y(\mathbf{x}^1) \cdots Y(\mathbf{x}^n) \times d\mathbf{x}^0 d\mathbf{x}^1 \ldots d\mathbf{x}^n. \tag{2.6}$$

Until now we have just discussed the general properties of W_n without making any assumption about the kind of stochastic process involved. For instance, if we assume our process to be completely random, there will be no dependence of $\mathbf{x}^1$ over $\mathbf{x}^0$ and further until $\mathbf{x}^n$. In this way the joint probability W_n can be factored as the product of the individual $W_1(\mathbf{x}^i, t_i)$. Taking the times appearing in W_n ordered in the form that $t_0 < t_1 < \cdots < t_n$, if we assume the probability distribution of $\mathbf{x}^n$ to depend only on the value of $\mathbf{x}^{n-1}$, i.e. the process to be Markovian, we can write

$$W_n(\mathbf{x}^0, t_0; \ldots; \mathbf{x}^n, t_n) = W_n(\mathbf{x}^0, t_0; \ldots; \mathbf{x}^{n-1}, t_{n-1}) P(\mathbf{x}^{n-1}, t_{n-1} | \mathbf{x}^n, t_n) \tag{2.7}$$

where $P(\mathbf{x}^{n-1}, t_{n-1}|\mathbf{x}^n, t_n)$ is the conditional probability of finding $\mathbf{x}^n$ at t_n given it was at $\mathbf{x}^{n-1}$ at t_{n-1}, normalized by

$$\int P(\mathbf{x}^{n-1}, t_{n-1}|\mathbf{x}^n, t_n) d\mathbf{x}^n = 1 \tag{2.8}$$

and subject to the initial condition

$$\int P(\mathbf{x}^{n-1}, t_{n-1}|\mathbf{x}^n, t_{n-1}) d\mathbf{x}^n = \delta(\mathbf{x}^n - \mathbf{x}^{n-1}). \tag{2.9}$$

Here we can apply the rule stated in Eq. (2.7) recursively and express the joint distribution as a product of conditional probabilities. Markovian processes are usually used to describe Brownian motion, where the position of the particle at the next instant of time depends only on where the particle was at the immediately precedent time and on the conditional probability. We can use this property and write the transition probability $\{\mathbf{x}^0, t_0\} \rightarrow \{\mathbf{x}, t\}$ as a two step process described by the Chapman-Kolmogorov equation [31]

$$P(\mathbf{x}^0, t_0|\mathbf{x}, t) = \int P(\mathbf{x}^0, t_0|\mathbf{x}^1, t-\tau) P(\mathbf{x}^1, t-\tau|\mathbf{x}, t) d\mathbf{x}^1, \tag{2.10}$$

where τ is an intermediate instant o time which satisfies $t_0 < t - \tau < t$. If the conditional probabilities are continuous functions, we can take τ as small as we want and with a Taylor expansion from the initial time, we can cast, to $\mathcal{O}(t^2)$ Eq. 2.10 in the master equation form [31]

$$\frac{\partial}{\partial t} P(\mathbf{x}^0, t_0|\mathbf{x}, t) = \int R(\mathbf{x}^1, \mathbf{x}) P(\mathbf{x}^0, t_0|\mathbf{x}^1, t_1) d\mathbf{x}^1, \tag{2.11}$$

being $R(\mathbf{x}^1, \mathbf{x}) = \partial P(\mathbf{x}^1, t_1|\mathbf{x}, t)/\partial t|_{t=t_0}$.

Finally, if a stochastic process is stationary, than the joint distribution is independent of t_0 and the transition probabilities depend only on the time differences $t_i - t_0$. Hence we can write

$$W_n(\mathbf{x}^0, t_0; \ldots; \mathbf{x}^n, t_n) = W_n(\mathbf{x}^0; \mathbf{x}^1, t_1 - t_0; \ldots; \mathbf{x}^n, t_n - t_0). \tag{2.12}$$

Now we are going to apply the formalism we developed to study the roto-diffusion

dynamics of non-rigid particles solvated in a liquid crystal environment. The experimental observables require knowledge of the particle orientation Ω and internal degrees of freedom χ, which will be our stochastic variable $\mathbf{x} = \{\Omega, \chi\}$. Therefore we can rewrite Eq. (2.2)

$$\langle A_H^{L,m}(0) B_H^{L',m'*}(t)\rangle = \sum_{n,n'} \sum_{\chi_0,\chi} \iint d\Omega_0 d\Omega W(\chi_0,\Omega_0,t_0;\chi,\Omega,t) D_{m,n}^{L*}(\Omega_0) \times D_{m',n'}^{L'}(\Omega) A_P^{L,n}(\chi_0) B_P^{L',n'*}(\chi). \tag{2.13}$$

where $W(\chi_0,\Omega_0,t_0;\chi,\Omega,t)$ is the joint probability of finding the same particle with shape χ_0 and orientation Ω_0 at $t = 0$ and to find the particle with shape χ and orientation Ω at time t.

We will now assume all stochastic processes to be Markovian, which allows us to rewrite the joint distribution as

$$W(\chi_0,\Omega_0,t_0;\chi,\Omega,t) = P(\chi_0,\Omega_0,t_0) P(\chi_0,\Omega_0,t_0|\chi,\Omega,t) \tag{2.14}$$

where $P(\chi_0,\Omega_0,t_0)$ is the probability of finding the particle at $\{\chi_0,\Omega_0\}$ at time $t = 0$ and $P(\chi_0,\Omega_0|\chi,\Omega,t)$ is the conditional probability of finding the particle with the orientation Ω and shape χ at time t given it had the orientation Ω_0 and shape χ_0 at time 0 (illustrated in Fig. 2.2). The conditional probability is normalized as follows:

$$\sum_{\chi} \int d\Omega\, P(\chi_0,\Omega_0,t_0|\chi,\Omega,t) = 1, \tag{2.15}$$

with the initial time boundary condition:

$$P(\chi_0,\Omega_0,t_0|\chi,\Omega,t = t_0) = \delta_{\chi_0,\chi}\delta(\Omega_0 - \Omega). \tag{2.16}$$

In a stable thermodynamic equilibrium, the stochastic processes are stationary, therefore, we can drop t_0 from the probability distribution defining

$$W_1(\Omega_0,\chi_0,t_0) \equiv P_{eq}(\Omega_0,\chi_0), \tag{2.17}$$

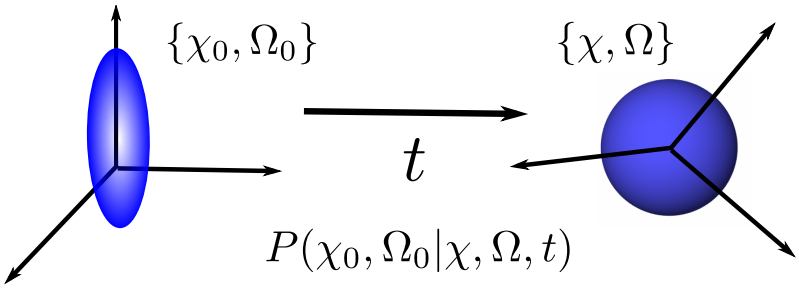

Figure 2.2: Conditional probability of a shape changing probe particle.

and rewrite Eq. (2.13) as

$$\langle A_H^{L,m}(0) B_H^{L',m'*}(t)\rangle = \sum_{n,n'}\sum_{\chi_0,\chi}\iint d\Omega_0 d\Omega P_{eq}(\chi_0,\Omega_0) P(\chi_0,\Omega_0|\chi,\Omega,t) \times D^L_{mn}(\Omega_0) D^{L'*}_{mn}(\Omega) A_P^{L,n}(\chi_0) B_P^{L',n'*}(\chi). \tag{2.18}$$

To calculate the components of Eq.(2.18), we need to describe how the probe particle interacts with the environment in order to derive the stochastic dynamics. The solute - solvent interactions depend on the molecular distribution of solvent around the probe particle and on the other particles of the same type of the probe one. If we assume our system to be in infinite dilution, there will be only solvent molecules around our probe particle, allowing us to describe their interaction by means of an effective, anisotropic, potential taking into account the effect of the surrounding environment on the particle of interest.

Since our probe particle is non rigid, in addition to the anisotropic potential, we should consider the intrinsic probability associated with different shapes [52]. For instance, we might consider that each shape has a different internal elastic energy, due to its constituent anisotropic material and structure [53]. To take this behaviour into account, we add to the mean-field potential a term dependent only on χ. The complete form of the effective potential $U(\chi,\Omega)$ will be given by

$$\frac{U(\chi,\Omega)}{k_B T} = u(\chi,\beta) = u_0(\chi) + \sum_{l_u,m_u,n_u} u^{l_u}_{m_u,n_u}(\chi) D^{l_u}_{m_u,n_u}(\Omega), \tag{2.19}$$

where k_B is the Boltzmann constant, T the temperature, $u^{l_u}_{m_u,n_u}(\chi)$ are the shape dependent anisotropic strength and $u_0(\chi)$ is the intrinsic shape dependent energy

term. We take β as the angle between the nematic host director, defining the Z lab axis and the particle z axis. In biaxial environments α is the angle between the probe particle and the host second director, taken to define X axis. γ is the angle between the molecule X axis and laboratory X axis. It is important to notice that the Wigner functions form a complete basis set, therefore, taking an appropriate number of Wigner functions we can obtain any other function depending on Ω. However, for the present work we will proceed as Nordio and Segre [19] and consider expansion of the effective potential until $L = 2$, to reduce the number of phenomenological free parameters.

In thermodynamic equilibrium, the probability of finding a particle with orientation Ω and shape χ in the anisotropic solvent, from now on referred as $P_{eq}(\chi,\Omega)$, will be given by the Boltzmann distribution

$$\begin{aligned} P_{eq}(\chi,\Omega) &= \frac{e^{-u(\chi,\Omega)}}{\sum_{\chi'}\int e^{-u(\chi',\Omega')}d\Omega'} \\ &= \frac{p_0(\chi)\exp\left[-\sum_{L,m,n} u^L_{m,n}(\chi)D^L_{m,n}(\Omega)\right]}{\sum_{\chi'} p_0(\chi')S^0_{0,0}(\chi')}. \end{aligned} \tag{2.20}$$

In the last expression we have introduced the intrinsic shape distribution

$$p_0(\chi) = \frac{e^{-u_0(\chi)}}{\sum_{\chi'} e^{-u_0(\chi')}}, \tag{2.21}$$

that can be interpreted as a normalized "*a priori*" (independent of the environment) probability density of observing a certain shape χ, and $S_0(\chi)$ is a special, $L = 0, m = 0, n = 0$, case of the rank-L integrals

$$\begin{aligned} S^L_{m,n}(\chi) &= \langle \exp\left[-\sum_{l_u,m_u,n_u} u^{l_u}_{m_u,n_u}(\chi)D^{l_u}_{m_u,n_u}(\Omega)\right] D^L_{m,n}(\Omega)\rangle_\Omega \\ &\equiv \int d\Omega \exp\left[-\sum_{l_u,m_u,n_u} u^{l_u}_{m_u,n_u}(\chi)D^{l_u}_{m_u,n_u}(\Omega)\right] D^L_{m,n}(\Omega). \end{aligned} \tag{2.22}$$

Even though we are interested in the correlation functions 2.13, it is more conve-

nient to treat each term in the summation (2.2) separately, defining

$$\phi^{L,L'}_{mm',nn',AB}(t) \equiv \sum_{\chi_0,\chi} \iint d\Omega_0 d\Omega P_{eq}(\chi_0,\Omega_0) P(\chi_0,\Omega_0|\chi,\Omega,t) D^{L}_{mn}(\Omega_0) D^{L'*}_{mn}(\Omega) \times A^{L,n}_{P}(\chi_0) B^{L',n'*}_{P}(\chi). \quad (2.23)$$

There is an infinite number of correlation functions (2.23), however, any experimental setup has only access to a finite (typically small) combination of them. As an example, here we will focus on two types of correlation functions.

In the first case we will consider that the orientational correlations functions are modulated by fluctuations in shape, but both $A^{L,n}_{P}(\chi_0) = A^{L,n}_{P}$ and $B^{L',n'*}_{P}(\chi) = B^{L',n'*}_{P}$ do not depend on χ. From now on, we will call these function angular correlation functions. They can be calculated as

$$\phi^{L,L'}_{mm',nn'}(t) = \sum_{\chi_0,\chi} \iint d\Omega_0 d\Omega P_{eq}(\chi_0,\Omega_0) P(\chi_0,\Omega_0|\chi,\Omega,t) D^{L}_{mn}(\Omega_0) D^{L'*}_{m'n'}(\Omega). \quad (2.24)$$

For the second kind we will consider the family of functions that depend on shape, but are independent of the particle orientation, i.e $\phi^{0,0}_{00,00,AB}(t) \equiv \phi_{AB}(t)$, which can be calculated by:

$$\phi_{AB}(t) = \sum_{\chi_0,\chi} \iint d\Omega_0 d\Omega P_{eq}(\chi_0,\Omega_0) P(\chi_0,\Omega_0|\chi,\Omega,t) A(\chi_0) B(\chi), \quad (2.25)$$

where $A \equiv A^{0}_{0,0}$ and $B \equiv B^{0}_{0,0}$. One example of such a function is $\phi_{a_i a_j}(t)$, which measures the correlation of a particle axis length a_i, here called axial correlation function. Due to its simplicity, we will use this function to study orientational independent functions.

Together with each correlation functions we can also measure the associate correlation time, given by

$$\tau^{L,L'}_{mm',nn'} = \int_0^\infty \left(\phi^{LL'}_{mm',nn'}(t) - \phi^{LL'}_{mm',nn'}(\infty) \right) dt \quad (2.26)$$

for the first kind and

$$\tau_{AB} = \int_0^\infty \left(\phi_{AB}(t) - \phi_{AB}(\infty)\right) dt, \tag{2.27}$$

for the second.

The initial and asymptotically long time values are of course independent of the dynamics of the system and can be written in terms of order parameters [54]. When $t = 0$ we have $P(\chi_0, \Omega_0 | \chi, \Omega, t = 0) = \delta_{\chi,\chi'}\delta(\Omega - \Omega_0)$ which can be substituted in Eq. (2.24) to give

$$\begin{aligned}\phi^{L,L'}_{mm',nn'}(0) &= \sum_\chi \int d\Omega P_{eq}(\chi,\Omega) D^L_{mn}(\Omega) D^{L'*}_{m'n'}(\Omega) \\ &= \frac{\sum_\chi p_0(\chi) \langle \exp\left[-\sum_{u^{L''}_{m'',n''}} u^{L''}_{m'',n''}(\chi) D^{L''}_{m'',n''}(\Omega)\right] D^L_{mn}(\Omega) D^{L'*}_{m'n'}(\Omega)\rangle_\Omega}{4\pi^2 \sum_{\chi'} p_0(\chi') S^0_{0,0}(\chi')}.\end{aligned} \tag{2.28}$$

We can obtain the explicit dependence on order parameters coupling the Wigner rotation matrices as

$$\begin{aligned}D^L_{mn}(\Omega) D^{L'*}_{m'n'}(\Omega) = (-1)^{m'-n'} &\sum_{J=|L-L'|}^{L+L'} C(L,L',J;m,-m') \\ &\times C(L,L',J;n,-n') D^L_{m-m',n-n'}(\Omega),\end{aligned} \tag{2.29}$$

where the Clebsch-Gordian coefficients $C(a,b,c;d,e)$ are tabulated elsewhere [55] and writing

$$\begin{aligned}\phi^{L,L'}_{mm',nn'}(0) = (-1)^{m'-n'} &\sum_{J=|L-L'|}^{L+L'} C(L,L',J;m,-m') \\ &\times C(L,L',J;n,-n') \frac{\sum_\chi p_0(\chi) S^J_{m-m',n-n'}(\chi)}{\sum_{\chi'} S^0_{0,0}(\chi') p_0(\chi')}.\end{aligned} \tag{2.30}$$

As $t \to \infty$ the conditional probability will be completely uncorrelated, therefore

$P(\chi_0,\Omega_0|\chi,\Omega,\infty) = P_{eq}(\chi_0,\Omega_0)P_{eq}(\chi,\Omega)$, which allows us to write:

$$\begin{aligned}\phi^{L,L'}_{mm',nn'}(\infty) &= \sum_{\chi_0,\chi}\iint d\Omega\, d\Omega_0 P_{eq}(\chi_0,\Omega_0)D^{L}_{mn}(\Omega_0)P_{eq}(\chi,\Omega)D^{L'*}_{mn}(\Omega) \\ &= (-1)^{m'-n'}\frac{\sum_\chi p_0(\chi)S^{L}_{m,n}(\chi)}{\sum_{\chi'} S^0_{0,0}(\chi')p_0(\chi')}\frac{\sum_\chi p_0(\chi)S^{L'}_{-m',-n'}(\chi)}{\sum_{\chi'} S^0_{0,0}(\chi')p_0(\chi')}.\end{aligned} \tag{2.31}$$

The initial values for second kind of correlation functions can be obtained with the same procedure. Substituting the initial conditions (2.16) in (2.25) we obtain for t=0:

$$\begin{aligned}\phi_{AB}(0) &= \sum_\chi \int d\Omega P_{eq}(\chi,\Omega)A(\chi)B(\chi) \\ &= \frac{\sum_\chi p_0(\chi)A(\chi)B(\chi)}{\sum_\chi p_0(\chi)S^0_{0,0}(\chi)},\end{aligned} \tag{2.32}$$

and for the asymptotic behaviour

$$\begin{aligned}\phi_{AB}(\infty) &= \sum_{\chi_0,\chi}\iint d\Omega d\Omega_0 P_{eq}(\chi_0,\Omega_0)A(\chi)P_{eq}(\chi,\Omega)B(\chi) \\ &= \frac{\sum_\chi p_0(\chi)A(\chi)}{\sum_\chi p_0(\chi)S^0_{0,0}(\chi)}\frac{p_0(\chi')B(\chi')}{\sum_{\chi'} p_0(\chi')S^0_{0,0}(\chi')},\end{aligned} \tag{2.33}$$

2.3 Evolution operator

The last quantity we need to determine is the evolution operator in Eq. 2.11. To proceed, we now need to introduce some models for the time evolution of the probability distribution. Here we will assume two distinct stochastic processes. The first is the usual rotational rotational diffusion, where the particle rotates by small jumps. The jump probability is shape dependent, but the particle remains rigid during this step. The last is the shape-changing process, which can be orientation dependent, but the orientation remain fixed during the change.

We shall assume for reorientations a rotational-diffusion process [19, 28, 56, 57], which implies that orientations change by small angular steps. This model is of very general use, but is particularly appropriate when the deformable probe particle is much bigger than the surrounding solvent ones, as we expect the case for a vesicle or gel particle.

Models for shape change are not so well developed, even though some significant contributions have been put forward [44, 45]. Here we shall assume a jump model where the shape remains constant for a time much longer than that required to switch to a new one, so that we can be approximate the conversion, as in the so called strong collision models, with an instantaneous transition [58].

The interaction between the particle and the anisotropic solvent environment is assumed to be modelled by an effective field potential of the Maier-Saupe type [59, 60]. If all the shapes share the same symmetry, we can take the angular dependence of the mean field potential to be the same before and after the shape transition, with only the strength of the interaction changing.

Restating our assumptions mathematically, we are assuming that at a given instant of time each particle is characterized by an orientation Ω and a "shape" χ degrees of freedom. We assume for simplicity that χ can take a discrete, finite even if arbitrary large set of values $\{\chi_i\}$, corresponding to a finite set of shapes ranging from an elongated, to a spherical, up to an oblate discotic one. The particle can behave as a rigid rotor with its rotational diffusion tensor $\mathbf{D}^{\chi}$ for a certain time and during this time lapse it is subject to an anisotropic effective field determined by the solvent and by its own anisotropy, but it is prone to changing its shape adopting a different χ.

Under these assumptions, the we can write the master equation as:

$$\frac{\partial}{\partial t} P(\chi_0, \Omega_0 | \chi, \Omega, t) = \Gamma(\chi, \Omega) P(\chi_0, \Omega_0 | \chi, \Omega, t), \tag{2.34}$$

where $\Gamma(\chi, \Omega)$ is the evolution operator. We can further separate the operator $\Gamma(\chi, \Omega)$ as the sum of the roto-diffusion operator $\Gamma_{\chi}(\Omega)$ plus the shape change operators $k_{\chi\chi'}(\Omega)$ connecting each shape possibility χ and χ'. We can therefore rewrite Eq. (2.34) as

$$\frac{\partial}{\partial t} P(\chi_0, \Omega_0 | \chi, \Omega, t) = \Gamma_{\chi}(\Omega) P(\chi_0, \Omega_0 | \chi, \Omega, t) + \sum_{\chi'} k_{\chi\chi'}(\Omega) P(\chi_0, \Omega_0 | \chi', \Omega, t).$$

Following [27,28] we the stochastic operator $\Gamma_\chi(\Omega)$ is given by

$$\begin{aligned}\Gamma_\chi(\Omega) = &- D_x^\chi\{L_x^2 + L_x\left[L_x u(\chi,\Omega)\right]\}\\ &- D_y^\chi\{L_y^2 + L_y\left[L_y u(\chi,\Omega)\right]\}\\ &- D_z^\chi\{L_z^2 + L_z\left[L_z u(\chi,\Omega)\right]\},\end{aligned} \tag{2.35}$$

where L_x, L_y, L_z are the angular momentum operators and $\{D_x^\chi, D_y^\chi, D_z^\chi\}$ are the χ shape diffusion tensor components. This is the most general case for the roto-diffusion operator. In the next sessions, we will develop a specific version for each case studied.

Now we need to define the operator that performs shape transitions $k_{\chi\chi'}(\Omega)$. In our model, the symmetry axis of the particle is conserved during the shape change. In this way the switch operator will connect only functions with the same orientation. According to detailed balance in stationary conditions, the transition between two states will obey

$$k_{\chi\chi'}(\Omega)P_{eq}(\chi',\Omega) = k_{\chi'\chi}P_{eq}(\chi,\Omega), \tag{2.36}$$

which allows us to assume

$$k_{\chi\chi'}(\Omega) = \frac{e^{-u(\chi,\Omega)/2}}{e^{-u(\chi',\Omega)/2}}\zeta(\chi,\chi') \quad \forall \quad \chi' \neq \chi, \tag{2.37}$$

where $\zeta(\chi,\chi')$ are and $\zeta(\chi',\chi) = \zeta(\chi,\chi')$. If we consider that every shape can have a different intrinsic persistence time and $\zeta(\chi)$ represents the inverse of the residence time of the particle in its shape χ, then we could think of $\zeta(\chi',\chi) = [\zeta(\chi) + \zeta(\chi')]/2$.

The conservation of overall probability condition can be satisfied, as for every Markov process, by defining the diagonal elements of the transition matrix as

$$k_{\chi\chi}(\Omega) = -\sum_{\chi'\neq\chi} k_{\chi'\chi}(\Omega). \tag{2.38}$$

Here we derived a mathematical expression for $k_{\chi'\chi}(\Omega)$, but the physics of the problem can impose some constraints on the connectivity of the shapes. For instance, we can have a system where just shapes with similar forms can be visited, here called neighbouring shapes. The number of neighbouring shapes depends on the symmetry of the probe particle, for example, a uniaxial particle could have two neighbours, one

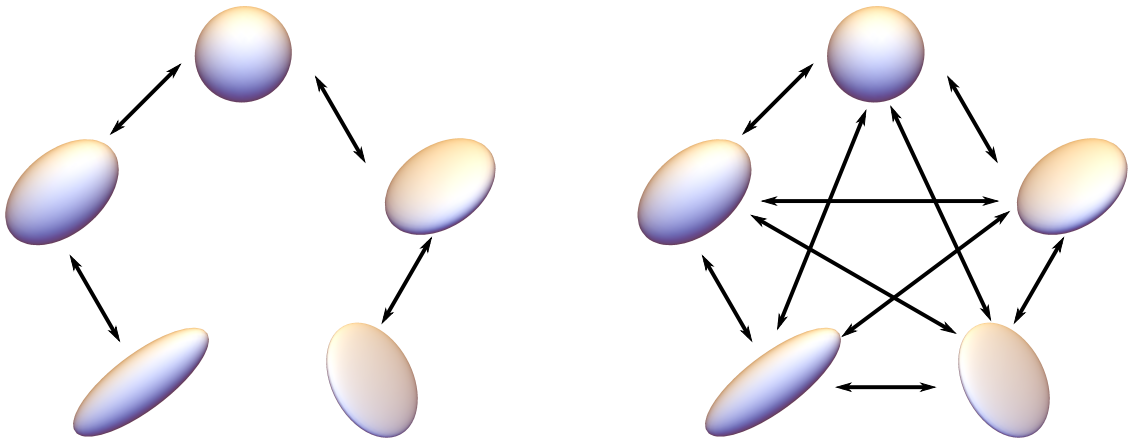

(a) First neighbors **(b)** All connected

Figure 2.3: Shape connectivity model.

shape that is more elongated and another one more squashed. A biaxial probe particle can transform in more dimensions, and will probably have at least 4 neighbours. We call this connection model first neighbour connectivity.

On the other way, we can also have all shapes direct accessible to all shapes. This is the analogue of the strong collision model, but for shape exchange. In Fig. 2.3 we can see a sketch of the models.

The set of differential equations (2.35), together with the initial conditions (2.16), describes the dynamics of the orientation and their solution allows calculations of the correlation functions in Eq. (2.24).

Chapter 3

Uniaxial particles in uniaxial nematic liquid crystals

In this chapter we will apply the formalism developed in chapter 2 to study the roto-diffusion of uniaxial particles dissolved in a uniaxial liquid crystal. Since we are taking the host to be uniaxial, an arbitrary rotation of ψ around the laboratory Z axis, which multiplies the r.h.s of Eq. (2.2) for $\exp[i(\psi(m-m')]$ should leave the results invariant, therefore allowing only the correlation functions $\phi^{L,L'}_{mm',nn'}(t)$ with $m = m'$ to be different from 0, i.e., $\delta_{mm'}$.

If we assume that the change of shape, however large, corresponds to a sort of breathing mode that maintains the particle uniaxial around its z axis, then we also have $\delta_{nn'}$. In practice, the particle is assumed here to have a uniaxial ellipsoidal shape, with axes

$$\begin{aligned} a_x(\chi) &= a_y(\chi) = a_\perp(\chi), \\ a_z(\chi) &= a_\parallel(\chi), \end{aligned} \tag{3.1}$$

which allows us to define the aspect ratio $\rho_\chi = a_\perp(\chi)/a_\parallel(\chi)$.

With these symmetries, we can reduce some of the parameters used in the model; for instance the diffusion tensor can also be rewritten as

$$\begin{aligned} D^\chi_x(\chi) &= D^\chi_y(\chi) = D^\chi_\perp(\chi), \\ D^\chi_z(\chi) &= D^\chi_\parallel(\chi). \end{aligned} \tag{3.2}$$

The symmetries also reduce the number of parameters involved in the mean-field potential. More specifically, we have $u^l_{m,n}(\chi) = 0$ for all $m \neq 0$ and $n \neq 0$, which allows us to write

$$u(\chi,\Omega) = u_0(\chi) + u_2(\chi)P_2(\cos\beta), \tag{3.3}$$

where we replaced $u^2_{0,0}(\chi) = u_2(\chi)$ for simplicity.

With these parameters we setup the set of evolution equations.

3.1 Evolution equation

The stochastic rotation operator for our probe particle can be obtained substituting Eqs. (3.2) in Eq. (2.35) to obtain

$$\begin{aligned}\Gamma_\chi(\Omega) = -D^\chi_\perp\{L_x^2 + L_x\left[L_x u(\chi,\Omega)\right]\} - D^\chi_\perp\{L_y^2 + L_y\left[L_y u(\chi,\Omega)\right]\} \\ -D^\chi_\parallel\{L_z^2 + L_z\left[L_z u(\chi,\Omega)\right]\}.\end{aligned} \tag{3.4}$$

Following Zare formalism [61], the angular momentum operator components can be written in terms of Euler angles derivatives as

$$\begin{aligned}L_x &= -i\cos\gamma\left(\cot\beta\frac{\partial}{\partial\gamma} - \frac{1}{\sin\beta}\frac{\partial}{\partial\alpha}\right) - i\sin\gamma\frac{\partial}{\partial\beta} \\ L_y &= i\sin\gamma\left(\cot\beta\frac{\partial}{\partial\gamma} - \frac{1}{\sin\beta}\frac{\partial}{\partial\alpha}\right) - i\cos\gamma\frac{\partial}{\partial\beta} \\ L_z &= -i\frac{\partial}{\partial\gamma}.\end{aligned} \tag{3.5}$$

Replacing equations (3.5) in Eq. (3.4), gives after some algebraic manipulations

$$\begin{aligned}\Gamma_\chi(\Omega) = &\frac{1}{2}\left(D^\chi_\perp\cot^2\beta + D^\chi_\perp\csc^2\beta - D^\chi_\perp + 2D^\chi_\parallel\right)\frac{\partial^2}{\partial\gamma^2} \\ &+ D^\chi_\perp\left(\frac{\partial^2}{\partial\beta^2} + \csc^2\beta\frac{\partial^2}{\partial\alpha^2} - 2\cot\beta\csc\beta\frac{\partial^2}{\partial\alpha\partial\gamma}\right) \\ &+ D^\chi_\perp\left(\cot\beta + \frac{\partial u(\beta)}{\partial\beta}\frac{\partial}{\partial\beta}\right) + D^\chi_\perp\left(\frac{\partial^2 u(\beta)}{\partial\beta^2} + \cot\beta\frac{\partial u(\beta)}{\partial\beta}\right).\end{aligned} \tag{3.6}$$

For a vanishing effective field term $u(\chi,\Omega)$, i.e., for an isotropic liquid, the eigenfunctions of $\Gamma(\Omega)$ for a particle of a given shape are the Wigner functions: $D^L_{mn}(\Omega) = \exp(-im\alpha)d^L_{mn}(\beta)\exp(-in\gamma)$. In our current case we have $u(\chi,\Omega) = u(\chi,\beta)$, thus both

operators $\Gamma_\chi(\Omega)$ and $k_{\chi\chi'}(\Omega)$ depend only on β. Therefore, we can use the uniaxial symmetry around the laboratory and particle frame principal axis to write the eigenfunctions of $\Gamma_\chi(\Omega)$ as $\Psi_{mn}(\Omega) = \exp(-im\alpha)P_{m,n}(\chi_0,\beta_0|\chi,\beta,t)\exp(-in\gamma)$, effectively separating variables in equation 2.35.

In the space being considered, the angles $\alpha = 0$ and $\alpha = 2\pi$ are equivalent; consequently we need to ensure that the conditional probability takes it into consideration and that is possible only if m is an integer. The same considerations must hold for γ; as a consequence, we have that n is also an integer. Therefore, after applying the initial condition, the conditional probability can be written as

$$P(\chi_0,\Omega_0|\chi,\Omega,t) = \frac{1}{4\pi^2}\sum_{m,n} e^{-im(\alpha-\alpha_0)}P_{m,n}(\chi_0,\beta_0|\chi,\beta,t)e^{-in(\gamma-\gamma_0)}. \tag{3.7}$$

Substituting (3.7) in (3.6) we will obtain for each term m and n

$$\begin{aligned}\Gamma_\chi(\beta)P_{m,n} = D_\perp^\chi\Big\{&\frac{\partial^2 P_{m,n}}{\partial\beta^2} + \cot\beta\frac{\partial P_{m,n}}{\partial\beta}\\ &-\left[\frac{m^2+n^2-2mn\cos\beta}{\sin^2\beta} + \left(\frac{D_\parallel^\chi}{D_\perp^\chi}-1\right)n^2\right]P_{m,n}\\ &+\left[\frac{1}{\sin\beta}\frac{\partial}{\partial\beta}\left(\sin\beta\frac{du(\beta)}{d\beta}P_{m,n}\right)\right]\Big\},\end{aligned} \tag{3.8}$$

where $P_{m,n} \equiv P_{m,n}(\chi_0,\beta_0|\chi,\beta,t)$. With the substitution $x = \cos\beta$

$$\begin{aligned}\Gamma_\chi(x)P_{m,n} = D_\perp^\chi\Big\{&(1-x^2)\frac{d^2P_{m,n}}{dx^2} + \left[-2x+(1-x^2)\frac{du(x)}{dx}\right]\frac{dP_{m,n}}{dx}\\ &+\left[\left(1-\frac{D_\parallel^\chi}{D_\perp^\chi}\right)n^2 - \frac{m^2+n^2-2mnx}{1-x^2}\right]P_{m,n}\\ &-2x\frac{du(x)}{dx}P_{m,n} + (1-x^2)P_{m,n}\frac{d^2u(x)}{dx^2}\Big\}.\end{aligned} \tag{3.9}$$

Assuming an anisotropic potential like that in Eq. (3.3), we obtain

$$\begin{aligned}
&\Gamma_\chi(x)P_{m,n} \\
&= D_\perp^\chi \Big\{(1-x^2)\frac{d^2P_{m,n}}{dx^2} + \left[-2x + 3u_2(\chi)(1-x^2)\right]\frac{dP_{m,n}}{dx} \\
&+ \left[\left(1-\frac{D_\parallel^\chi}{D_\perp^\chi}\right)n^2 - \frac{m^2+n^2-2mnx}{1-x^2}\right]P_{m,n} \\
&+3u_2(\chi)x(1-3x^2)P_{m,n}\Big\}. \qquad (3.10)
\end{aligned}$$

Since the evolution operator $\Gamma_\chi(\Omega)$ can be symmetrized by a unitary transformation (see e.g. [28]), its eigenvalues will be real and its eigenfunctions for non-degenerate eigenvalues orthogonal. Due to the orthogonality of $\Psi_{m,n}(\Omega)$, the only eigenfunctions needed to calculate $\phi_{m,n}^{L,L'}$ are $\Psi_{m,n}(\Omega)$ and to calculate $\phi_{AB}(t)$ just $\Psi_{0,0}(\Omega)$. Therefore, we can solve the Eq. (3.10) using only the desired value of m and n corresponding to the required correlation function.

While the present formulation is still relatively general, in the absence of available experimental results to try to interpret, we now wish to consider in detail some special cases, where we can concentrate on the physics of the interplay between shape and orientational fluctuations and the general effects of the shape changing on the correlation times in our system. Therefore, the equation we will solve explicitly will be that for $m = n = 0$:

$$\begin{aligned}
\Gamma_\chi(x)P_{0,0} = D_\perp^\chi \Big\{&(1-x^2)\frac{d^2P_{0,0}}{dx^2} \\
&+ \left[-2x + 3u_2(\chi)(1-x^2)\right]\frac{dP_{0,0}}{dx} \\
&+ 3u_2(\chi)x(1-3x^2)P_{0,0}\Big\}. \qquad (3.11)
\end{aligned}$$

This equation can be solved numerically in various ways. Here we have used a finite differences algorithm as detailed later.

From now on we shall focus, for simplicity, only on the calculation of correlations for axial properties, where $A_P^{L,n}(\chi_0) = A_P^{L,0}(\chi)\delta_{n0}$, $B_P^{L,n\,*}(\chi) = B_P^{L,0\,*}(\chi)\delta_{n0}$ and accordingly we shall only consider the subset of correlation functions $\phi_{0,0}^L(t) \equiv \phi_{0,0}^{L,L}$, which will be sufficient to characterize the rotational motion of the particle principal axis, i.e., its tumbling motion and the corresponding orientational correlation times τ^L:

$$\tau^L = \int_0^\infty [\phi^L_{0,0}(t) - \phi^L_{0,0}(\infty)]dt, \tag{3.12}$$

associated to the relaxation of a physical property of rank L. Referring to just a few of the many experimental techniques available [62], we can think of a dielectric relaxation experiment where $L = 1$. and we assume the particle dipole moment to be along the particle axis. Alternatively, for a deuterium NMR experiment, referring to a case where the quadrupolar tensor monitored is along the same axis ($L = 2$ in this case).

3.2 Numerical formulation

The solution of the set of equations (2.35) and the calculation of the correlation functions and their respective correlation times is performed numerically. In particular, we have introduced a matrix representation of the evolution operator over an angular grid in x using a finite differences approach [57] and proceeded to write P_{00} in terms of the eigenvalues and eigenvectors of the evolution matrix [28].

These equations have been solved using a finite differences method with a uniform grid in $x = \cos\beta$ space, from $x = -1$ to $x = 1$. Therefore, the distance Δ between two adjacent points is $\Delta = 2/(N-1)$. The conditional probabilities in this space will be denoted by $P_{0,0}(\chi_0, x_0|\chi, x_i, t)$.

We used centred differences for the first order derivatives and symmetric differences for the second order derivative, in this way

$$\begin{aligned}
\frac{\partial}{\partial x} P_{0,0}(\chi_0, x_0|\chi, x_i, t) &= \frac{P_{0,0}(\chi_0, x_0|\chi, x_{i+1}, t) - P_{0,0}(\chi_0, x_0|\chi, x_{i-1}, t)}{2\Delta} \\
\frac{\partial^2}{\partial x^2} P_{0,0}(\chi_0, x_0|\chi, x_i t) &= \frac{P_{0,0}(\chi_0, x_0|\chi, x_{i+1}, t) + P_{0,0}(\chi_0, x_0|\chi, x_{i-1}, t) - 2P_{0,0}(\chi_0, x_0|\chi, x_i, t)}{\Delta^2}.
\end{aligned} \tag{3.13}$$

Using equations (3.13) we can write the rotational operator Γ as a matrix with elements $\Gamma_{\chi i,\nu j}$ connecting the shape ν and orientation j with shape χ and orientation

i as [63]:

$$\Gamma_{\chi i,\nu j} = \begin{cases} D^{\chi}\left[\dfrac{1-x_i^2}{\Delta^2} - \dfrac{-2x_i + 3u_2(\chi)x_i - 3u_2(\chi)x_i^3}{2\Delta}\right] & \forall \quad j = i-1 \quad \text{and} \quad \nu = \chi \\ D^{\chi}\left[-2\dfrac{1-x_i^2}{\Delta^2} + 3u_2(\chi)(1-3x_i^2)\right] & \forall \quad i = j \quad \text{and} \quad \nu = \chi \\ D^{\chi}\left[\dfrac{1-x_i^2}{\Delta^2} + \dfrac{-2x_i + 3u_2(\chi)x_i - 3u_2(\chi)x_i^3}{2\Delta}\right] & \forall \quad j = i+1 \quad \text{and} \quad \nu = \chi \\ 0 & \text{otherwise.} \end{cases} \tag{3.14}$$

We have assumed reflective boundary conditions, i.e., that the particle is not allowed to move beyond the limiting angles. Mathematically, this can be achieved making the flux equals to 0 across the borders, attained by the expressions:

$$\Gamma_{\chi 1,\chi 1} = -\Gamma_{\chi 2,\chi 1}$$
$$\Gamma_{\chi N,\chi N} = -\Gamma_{\chi N-1,\chi N}.$$

The operator $k_{\chi\nu}(x)$ will be written as a matrix $\mathbf{K}$ with elements $K_{\chi i,\nu j}$ that connects the shape ν and orientation j with shape χ and orientation i as:

$$K_{\chi i,\nu j} = \begin{cases} e^{-[u(\chi,x_j)-u(\nu,x_i)]/2}\zeta(\nu,\chi) & \forall \quad j = i \quad \text{and} \quad \chi \neq \nu \\ -\sum_{\chi'\neq\chi} e^{-[u(\chi',x_j)-u(\chi,x_i)]/2}\zeta(\chi,\chi') & \forall \quad j = i \quad \text{and} \quad \chi = \nu \\ 0 & \text{otherwise.} \end{cases} \tag{3.15}$$

Therefore, we can write the general operator as

$$W_{\chi i,\nu j} = \Gamma_{\chi i,\nu j} + K_{\chi i,\nu j} \tag{3.16}$$

and

$$\frac{\partial}{\partial t}P_{0,0}(\chi_0,x_0|\chi,x_i,t) = \sum_{\nu,j} W_{\chi i,\nu j}P_{0,0}(\chi_0,x_0|\nu,x_j,t). \tag{3.17}$$

Given the initial conditions x_0 and χ_0, we can write the conditional probability $P_{0,0}(\chi_0, x_0|\chi, x_i, t)$ as a column vector $\mathbf{P_{0,0}}(t)$. In this way, the linear system of equations (3.17) can be written in matrix form

$$\frac{\partial}{\partial t}\mathbf{P_{0,0}}(t) = \mathbf{W}\mathbf{P_{0,0}}(t), \tag{3.18}$$

which can be solved straightforwardly diagonalizing the matrix $\mathbf{W}$:

$$\mathbf{W} = \mathbf{R}\mathbf{w}\mathbf{L}^T, \tag{3.19}$$

where $\mathbf{R}$ and $\mathbf{L}$ are a matrix whose columns are composed by the right and left eigenvectors $\mathbf{W}$ and $\mathbf{w}$ is the diagonal eigenvalues matrix. The left and right eigenvectors are orthogonal, therefore, the product $\mathbf{R}$ and $\mathbf{L}$ are orthogonal and have to be normalized as

$$\mathbf{L}^T\mathbf{R} = \mathbf{I}. \tag{3.20}$$

Consequently, the solution is:

$$\mathbf{P_{0,0}}(t) = \mathbf{R}e^{\mathbf{w}t}\mathbf{L}^T\mathbf{P_{0,0}}(0). \tag{3.21}$$

Applying the initial conditions, the solutions will be

$$P_{0,0}(\chi_0, x_0|\chi, x_i, t) = \sum_{vj}(R)_{\chi i, vj}e^{w_{vj}t}(L^T)_{vj,\chi_0 x_0}. \tag{3.22}$$

The convergence of the algorithm was tested comparing the values calculated by the algorithm proposed here for $t = 0$ and $t = \infty$ with the ones calculated using Eq. (2.30) and Eq. (2.31).

3.3 Estimating the shape dependence of the diffusion coefficients and of the effective field potential

To estimate the shape dependence of the mean field potential, we assume that its interaction strength can be related to the instantaneous anisotropy of the guest particle [64]. In the limit of vanishingly small concentration of solute particles, the mean field theory for mixtures [25, 60, 65] yields

$$u_2(\chi) = c_{200}(\chi)\langle P_2\rangle_{LC}, \tag{3.23}$$

where $\langle P_2\rangle_{LC}$ is the order parameter of the liquid crystal host, that carries the dominant temperature dependence of $u_2(\chi)$ and in particular brings it to zero when the host system becomes isotropic. The interaction strength $c_{200}(\chi)$ depends on both the solvent and the solute particles properties. In a few cases [60], c_{200} can be separated in a product of particle and solvent contributions. In particular if, at molecular level, the orienting potential is determined by dispersion forces, via anisotropic polarizability interactions, the interaction coefficients become [64]

$$c_{200} = \xi_{12}\alpha_{LC}^{2,0}\alpha_P^{2,0}, \tag{3.24}$$

where ξ_{12} is a proportionality constant and $\alpha_{LC}^{2,0}$, $\alpha_P^{2,0}$ spherical components of the polarizability tensors for the nematogen and the deformable particle, $\boldsymbol{\alpha}_{LC}$ $\boldsymbol{\alpha}_P$. If, instead, the deformable particle is much larger than the solvent ones, e.g. a gel nanoparticle or a micelle, and it can be considered as a dielectric bead of ellipsoidal shape its polarizability and aspect factor are related and explicit forms for the shape dependent polarizability are available [66, 67]. An alternative mechanism for particle alignment focuses purely on its shape via steric repulsions [68, 69]. Although the mechanism for alignment is very different, the functional form of the effective potential is not specific to dispersive interactions but applies to any potential that

decouples in a similar way into solute and solvent factors.

$$c_{200}(\chi) = \xi'_{12} F_{LC}^{2,0} F_P^{2,0}(\chi), \tag{3.25}$$

where ξ'_{12} is a proportionality constant. Establishing a precise relation between the shape of the particle and the actual dominant type of interaction, even if there was a single one, is hardly possible and beyond the scope of this work. However, since the actual particle shape anisotropy is at the core of many types of relevant interactions, e.g. steric repulsion ones, we can assume to a first approximation a form like eq. (3.25) and try to evaluate this shape anisotropy. To do this, we adopt an approach similar to the one used in [60], introducing a shape tensor $\mathbf{F}$, similar to the inertia tensor, but with the distribution of local masses replaced by a distribution of local sizes. This can be easily visualized in two cases. The first (see, e.g., ref. [60]) is when where we deal with specific molecules, and the constituents are just atoms or, in the second case, when we deal with berry-like nanoparticles formed by aggregates of spherical sub-units [70]. In these cases we could use, to quantify the size of the individual constituents of the particles, their van der Waals radii (d_i) of each constituent and write

$$F_{ab} = \sum_i d_i (\mathbf{r}^i \cdot \mathbf{r}^i \delta_{ab} - r_a^i r_b^i), \tag{3.26}$$

where $\mathbf{r}^i$ is the position vector of the ith constituent of the particle, and r_a^i its components.

Another simple case is when, instead, we can assume that the particle is approximately homogeneous, e.g. for colloidal gel particles, in which case we can substitute the discrete summation with an integral over its volume. If the particles have uniaxial ellipsoidal shape like we assume here, the principal Cartesian components of the steric tensor will then be

$$\boldsymbol{F} \propto \begin{bmatrix} ({a_\parallel}^2 + {a_\perp}^2) & 0 & 0 \\ 0 & (a_\parallel^2 + {a_\perp}^2) & 0 \\ 0 & 0 & 2{a_\perp}^2 \end{bmatrix}. \tag{3.27}$$

therefore we will have $\mathbf{F}^{2,0} \propto ({a_\perp}^2 - {a_\parallel}^2)$. This allow us to write

$$u_2(\chi) = \xi {a_\parallel}^2(\rho^2 - 1), \tag{3.28}$$

where the proportionality constant ξ can be used as a free parameter.

Having established a procedure for determining the effective potential, we still have to adopt an explicit expression for the rotational diffusion tensor $\mathbf{D}^\chi$ for a particle of a give shape χ and in practice we shall employ for this, assuming that the classical stick boundary condition holds, the Stokes-Einstein-Perrin expressions [71]. Even though these expressions strictly apply to an anisotropic body reorienting in an isotropic solvent with sticky boundary conditions, an equivalent expression does not exist to the best of our knowledge for anisotropic media and moreover we can expect that the major effect of the medium will be to bias the preferred orientation, taken into account by the distribution, rather than the mean square angular fluctuations around each orientation. For a spherical particle of radius R immersed in a fluid of viscosity η, the rotational diffusion coefficient $D^s(R)$ can be written as

$$D^s(R) = \frac{k_B T}{8\pi\eta R^3}. \tag{3.29}$$

The coefficients for an ellipsoid also have well known expressions depending on the aspect ratio $\rho = a_\perp/a_\parallel$ and the hydrodynamic radius $d = \sqrt[3]{a_\parallel {a_\perp}^2}$. For prolate ellipsoids ($\rho < 1$) the rotational coefficient perpendicular to the symmetry axis can be written as [34, 72]

$$D_\perp^{prolate} = D^s(d)\frac{3\rho^2}{2(1-\rho^4)}\left[\frac{2-\rho^2}{\sqrt{1-\rho^2}}\ln\left(\frac{1+\sqrt{1-\rho^2}}{\rho}\right) - 1\right]. \tag{3.30}$$

Similarly, for a squashed ellipsoid ($\rho > 1$) the diffusion coefficient can be written as:

$$D_\perp^{oblate} = D^s(d)\frac{3\rho^2}{2(\rho^4-1)}\left[\frac{\rho^2-2}{\sqrt{\rho^2-1}}\arctan\left(\sqrt{\rho^2-1}\right) + 1\right]. \tag{3.31}$$

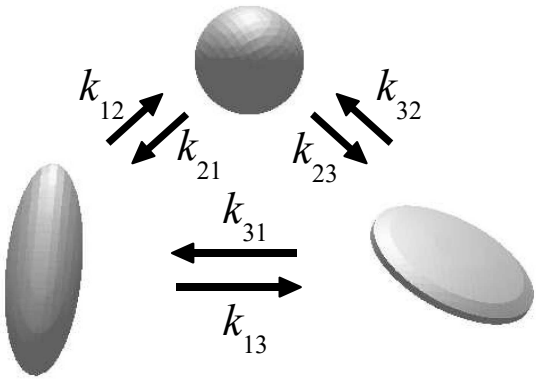

Figure 3.1: The shape switching process between rod-like, spherical and disk-like ellipsoidal particles.

3.4 Results

We can now show the general behaviour of the proposed model performing calculations for a range of parameters and analysing how the correlation functions of interest will change.

Although our model can be applied to an arbitrary discrete number of shapes, here we assume for simplicity only three distinct cases: a prolate ellipsoid (rod), an oblate ellipsoid (disk) and a sphere. In all the cases we choose the axis lengths size in a way that the hydrodynamic radius across different particles is equal, i.e. $a_{\parallel}^{*} a_{\perp}^{*\,2} = 1$. We can see a sketch of the switching shapes in Fig. 3.1.

The analysis of the results is made simpler as well as more general using dimensionless units, i.e., performing the set of substitutions

$$\begin{aligned} t^{*} &= D^{s} t, & \zeta^{*}(\chi, \nu) &= \zeta(\chi, \nu)/D^{s}(d), \\ a_{\parallel}^{*} &= a_{\parallel}/d, & a_{\perp}^{*} &= a_{\perp}/d \\ D_{\perp}^{\chi,*} &= D_{\perp}^{\chi}/D^{s}(d) & . & \end{aligned} \tag{3.32}$$

The axis lengths and the calculated rotational diffusion coefficients are reported in Table 3.1, where we also provide the order parameters calculated for a rigid probe particle with the same dimensions and interaction parameters.

To understand how the shape exchange influences the dynamics of the correlation

Table 3.1: Value of the shape dependent parameters for the three shapes. $\phi^L_{\chi,0,0}$ are the angular correlation functions calculated for the rigid shape χ. Here we have used $\xi = 1$ in the mean field calculation.

χ	Shape	$D^{\chi,*}_{\perp}$	$u_2(\chi)$	$a^*_{\parallel}$	$a^*_{\perp}$	$\phi^L_{\chi,0,0}(0)$	$\phi^L_{\chi,0,0}(\infty)$
1	Rod	0.42	-3.85	2.08	0.69	0.58	0.49
2	Spherical	1.0	0.00	1.00	1.00	0.2	0.0
3	Disk	0.54	2.36	0.4	1.59	0.16	0.09

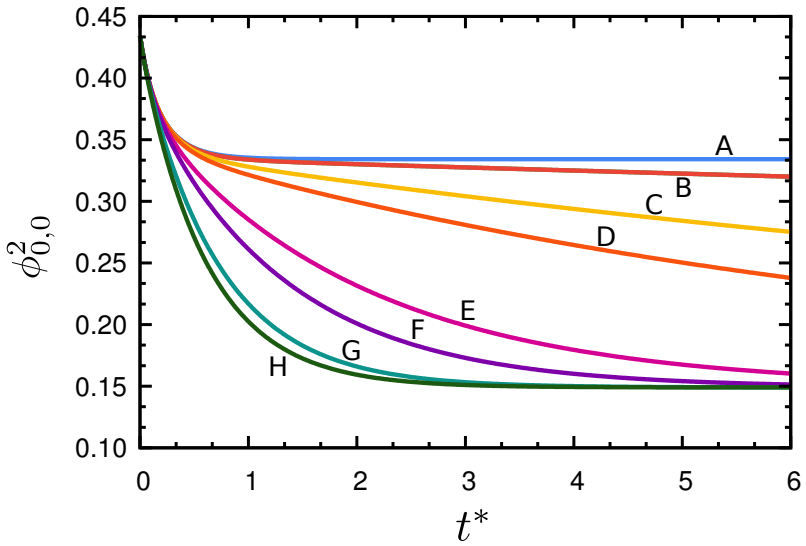

Figure 3.2: Angular correlation functions for the particle described in Table 3.1. The curves were obtained using $p_0(\chi) = 1/3$ for all shapesχ and switching rate $\zeta^* = 0$ (A), 0.01 (B), 0.05 (C), 0.1(D), 0.5 (E) , 1 (F), 5 (G), 20 (H).

functions, we will consider two cases in turn. In the first, we examine how the shape exchange rate affects the orientational correlations functions. In the second, we will examine how the intrinsic aspect ratios distribution affects the orientational and shape correlation functions and correlation times.

For the first case, we have assumed the same intrinsic probability for each shape, $p_0(\chi) = 1/3$ for all χ and varied the shape switching rates ζ^*. To simplify the analysis, we also assumed, as already mentioned, the same transition rate between any two distinct shapes. i.e., $(\zeta^*(\chi,\chi') = \zeta^*)$. A summary of our numerical results for angular correlation functions are shown in Fig. 3.2, for axial correlation functions in Fig. 3.3 and the correlation times in Fig. 3.4.

The plots show two distinct trends, one for $\zeta^* \ll 1$ and the other for $\zeta^* \gg 1$. In the first regime shape transitions are very infrequent and in the limit $\zeta^* \to 0$ each shape will evolve independently of each other, therefore the angular correlation function

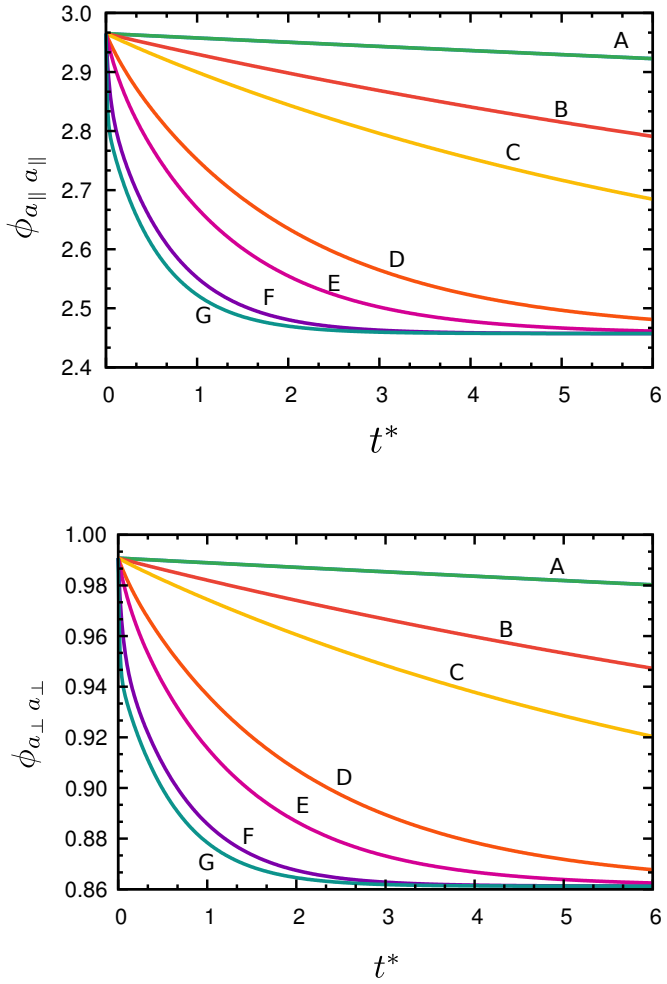

Figure 3.3: Correlation functions of the shape deformation for parallel (top) and perpendicular axis (bottom). The parameters used in the calculations is described in Table 3.1. The curves correspond to $p_0(\chi) = 1/3$. for all shapes χ and switching rate $\zeta^* = 0.01$ (A), 0.05 (B), 0.1 (C), 0.5 (D), 1 (E), 5(F), 20 (G).

will be given by

$$\phi^L_{0,0}(t^*) \approx \sum_\chi c_\chi \phi^L_{\chi,0,0}(t^*) \equiv \phi^{L,frozen}_{0,0}(t^*) \tag{3.33}$$

where

$$c_\chi = \frac{p_0(\chi) S_0(\chi)}{\sum_\nu p_0(\nu) S_0(\nu)}. \tag{3.34}$$

For comparison $\phi^{2,frozen}_{0,0}(t^*)$ can also be seen in Fig. 3.2. Note that for small values of ζ^* the correlation function is similar to $\phi^{L,frozen}_{0,0}(t^*)$ for short times, but the difference increases with time. This is reasonable since, if the change shape events are rare, they only take place on a long enough time scale. For the axial correlation function (i.e. FIG. 3.3), there is no equivalent frozen regime. In the absence of shape

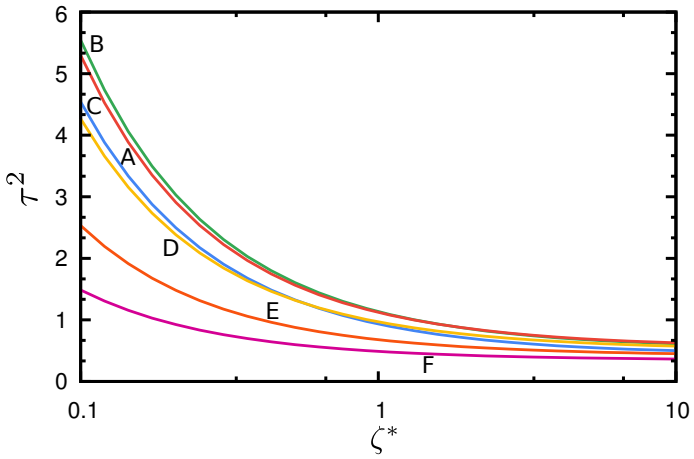

Figure 3.4: Correlation times τ^2 for $p_0(rod)/p_0(disk) = 0.2$ (A), 0.5 (B), 1(C), 2 (D), 5 (E) and 10 (F)

transition, the correlations function will be constant in time with value equal to the weighted average of the particle sizes.

The second limiting case is for rapid shape switching: $\zeta^* \gg 1$. As ζ^* increases, the shape exchange starts to happen in the same time scale as the roto-diffusion process. The correlation time (i.e. 3.4) decreases with the increase in ζ^*, but saturates to a plateau, with is consistent with the fact that the correlation function of a changing shape particle cannot decay faster than the fastest rigid correlation function among the possible shapes.

In our second analysis, we varied the intrinsic $p_0(\chi)$ keeping the shape transition rate ζ^* constant. To keep the analysis simple we varied the coefficient of the rod-like ellipsoid ($p_0(rod)$) while keeping $p_0(sphere) = p_0(disk)$. To check the consistence of our model we also calculated the correlation function for the rigid prolate ellipsoid and for a system where this shape is absent (i.e., just the sphere and disk are allowed.) The numerical results can be seen in Fig. 3.5, while the relative parameters and other informations for a given $p_0(rod)$ can be seen in Table 3.2.

Figures 3.5 and 3.4 show that the results are consistent. The ratio between different $p_0(\chi)$ controls the sampling of shapes in the initial conditions and during the relaxation process. For $p_0(rod) \gg p_0(disk)$, the probe particle behaves like a rigid rod-like ellipsoid, for $p_0(rod) \ll p_0(disk)$ the probe particle should behave as if this shape was not allowed, while a mixed behavior is found for intermediate values.

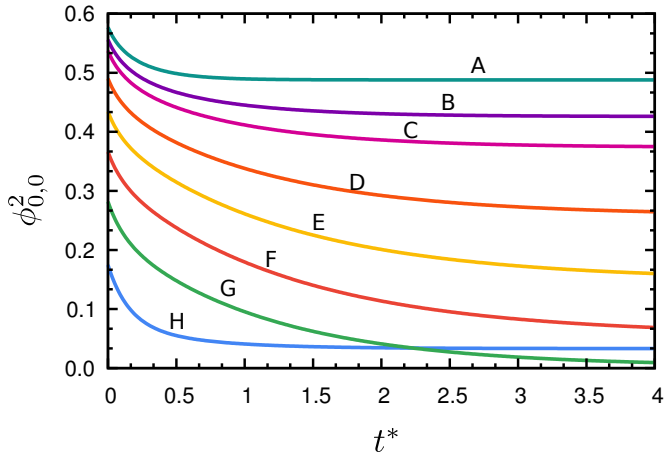

Figure 3.5: Angular correlation functions for the particle described in Table 3.1 . Here $\zeta = 1$ and $p_0(rod)/p_0(disk)$ = (A) ∞, (prolate); (B) 10; (C) 5; (D) 2; (E) 1; (F) 0.5; (G) 0.2; (H) 0.0.

Table 3.2: Equilibrium values and relative concentration for a particle which can assume all the shapes specified in table 3.1. We performed the calculations with $p_0(sphere) = p_0(disk)$.

$p_0(rod)/p_0(disk)$	c_{rod}	c_{sphere}	c_{disk}	$\phi^2_{0,0}(0)$	$\phi^2_{0,0}(\infty)$
0.0	0.0	39.6	60.3	0.174	3.30×10^{-2}
0.2	26.6	29.0	44.3	0.281	2.77×10^{-3}
0.5	47.6	20.8	31.6	0.366	5.62×10^{-2}
1.0	64.5	14.1	21.4	0.433	0.149
2.0	78.4	8.56	13.0	0.490	0.258
5.0	90.1	3.93	5.99	0.536	0.373
10.0	94.8	2.07	3.15	0.555	0.426

Chapter 4

Uniaxial particles dispersed in biaxial liquid crystals

In this chapter we will apply the formalism developed in chapter 2 to study the roto-diffusion of uniaxial particles dispersed in a biaxial liquid crystal. Here we will make the same assumptions for the solute particle made in the previous chapter. We are taking all shapes that our probe particle can assume to be uniaxial, furthermore, the change of shape also happens as a sort of breathing mode that maintains the particle uniaxial around its z axis. As a consequence the correlation functions $\phi^{L,L'}_{mm',nn'}(t)$ where $n \neq n$ are intrinsically 0, however, since the host is biaxial, now we can have correlation functions with $m \neq m'$.

Since all shapes are uniaxial, we can define

$$\begin{aligned} a_x(\chi) &= a_y(\chi) = a_\perp(\chi), \\ a_z(\chi) &= a_\parallel(\chi), \end{aligned} \tag{4.1}$$

and aspect ratio $\rho_\chi = a_\perp(\chi)/a_\parallel(\chi)$. The diffusion coefficients can again be reduced to

$$\begin{aligned} D^\chi_x(\chi) &= D^\chi_y(\chi) = D^\chi_\perp(\chi), \\ D^\chi_z(\chi) &= D^\chi_\parallel(\chi). \end{aligned} \tag{4.2}$$

Due to the biaxiality of the host, the α angle now defines the laboratory X axis

and secondary director. The mean-field potential $U(\chi,\Omega)$ will have the form

$$\frac{U(\chi,\Omega)}{k_BT} \equiv u(\chi,\Omega) = u_0(\chi) + u^2_{0,0}(\chi)D^2_{0,0}(\Omega) + u^2_{2,0}(\chi)\left(D^2_{2,0}(\Omega) + D^2_{-2,0}(\Omega)\right), \tag{4.3}$$

where k_B is the Boltzmann constant, T is the temperature, $u^L_{m,n}(\chi)$ is the shape dependent mean field interaction intensity and $D^L_{m,n}(\Omega)$ are Wigner functions. We like to call attention to $u_0(\chi)$ which is the intrinsic shape dependent energy term.

4.1 Evolution Operator

The time evolution of the conditional probabilities $P(\chi_0,\Omega_0|\chi,\Omega,t)$ in the roto-diffusion model is governed by the following set of differential equations

$$\frac{\partial}{\partial t}P(\chi_0,\Omega_0|\chi,\Omega,t) = \Gamma_\chi(\Omega)P(\chi_0,\Omega_0|\chi,\Omega,t) + \sum_{\chi'} k_{\chi\chi'}(\Omega)P(\chi_0,\Omega_0|\chi',\Omega,t), \tag{4.4}$$

subject to the initial conditions

$$P(\chi_0,\Omega_0|\chi,\Omega,t) = \delta(\Omega-\Omega_0)\delta_{\chi,\chi_0}, \tag{4.5}$$

where δ_{χ,χ_0} is a Kronecker delta, $\delta(\Omega-\Omega_0)$ is a Dirac delta, $\Gamma_\chi(\Omega)$ is the rotational-diffusion operator for a particle with shape χ and $k_{\chi\chi'}(\Omega)$ the transition operator from shape χ' to χ.

In the particle main frame, ignoring the coupling between diffusion and rotational diffusion we have:

$$\begin{aligned}\Gamma_\chi(\Omega) = &-D^\chi_\perp\left\{L^2_x + L_x\left[L_x u(\chi,\Omega)\right]\right\}\\ &-D^\chi_\perp\left\{L^2_y + L_y\left[L_y u(\chi,\Omega)\right]\right\}\\ &-D^\chi_\parallel\left\{L^2_z + L_z\left[L_z u(\chi,\Omega)\right]\right\},\end{aligned} \tag{4.6}$$

where L_x, L_y, L_z are the x,y,z quantum angular momentum operators, $D^\chi_\parallel$ and $D^\chi_\perp$

are the shape χ roto-diffusion coefficient parallel and perpendicular to the particle z axis, respectively.

In the actual form, the system of Eqs. (4.4) is closed and can be solved by the formalism we will further develop, but the equations are more convenient to manipulate algebraically if the functions and operators are symmetric in relation to $\{\chi_0, \Omega_0\}$ and $\{\chi, \Omega\}$. The symmetric set of conditional probabilities $\widehat{P}(\chi_0, \Omega_0|\chi, \Omega, t)$ functions can be obtained by the similarity transformation

$$\widehat{P}(\chi_0, \Omega_0|\chi, \Omega, t) = P_{eq}^{-1/2}(\chi, \Omega) P(\chi_0, \Omega_0|\chi, \Omega, t) P_{eq}^{1/2}(\chi_0, \Omega_0), \tag{4.7}$$

and they are subject to the initial conditions

$$\widehat{P}(\chi_0, \Omega_0|\chi, \Omega, 0) = \delta(\Omega - \Omega_0)\delta_{\chi_0,\chi}. \tag{4.8}$$

The symmetric version of the roto-diffusion operators can be obtained by the following similarity transformation

$$\begin{aligned}
\widehat{\Gamma}_\chi(\Omega) &= P_{eq}^{-1/2}(\chi, \Omega)\Gamma_\chi(\Omega)P_{eq}^{1/2}(\chi, \Omega) \\
&= -D_\perp^\chi \mathbf{L}^2 - \left(D_\parallel^\chi - D_\perp^\chi\right) {L_z}^2 - \frac{D_\perp^\chi}{2}\mathbf{L}^2 u(\chi, \Omega) \\
&+ \frac{D_\perp^\chi}{4} L_+ u(\chi, \Omega) L_- u(\chi, \Omega) - \frac{1}{2}\left(D_\parallel^\chi - D_\perp^\chi\right) {L_z}^2 u(\chi, \Omega) \\
&+ \frac{1}{4} D_\parallel^\chi \left(L_z u(\chi, \Omega)\right)^2,
\end{aligned} \tag{4.9}$$

here we used $L^2 = {L_x}^2 + {L_y}^2 + {L_z}^2$ and $L_\pm = L_x \pm i L_y$. While the symmetric shape-exchange operator can be obtained

$$\widehat{k}_{\chi\chi'}(\Omega) = P_{eq}^{-1/2}(\chi, \Omega) k_{\chi\chi'}(\Omega) P_{eq}^{1/2}(\chi', \Omega). \tag{4.10}$$

Since $k_{\chi\chi'}(\Omega) = P_{eq}^{1/2}(\chi, \Omega) P_{eq}^{-1/2}(\chi', \Omega)\zeta(\chi, \chi')$ for $\chi \neq \chi'$ and $k_{\chi\chi}(\Omega) = -\sum_{\chi' \neq \chi} k_{\chi\chi'}(\Omega)$ we will have:

$$\widehat{k}_{\chi\chi'}(\Omega) = \begin{cases} \zeta(\chi, \chi') \quad \forall \quad \chi \neq \chi' \\ -\sum_{\chi' \neq \chi} P_{eq}^{1/2}(\chi', \Omega) P_{eq}^{-1/2}(\chi, \Omega)\zeta(\chi', \chi) \quad \text{otherwise.} \end{cases} \tag{4.11}$$

Therefore, the symmetrized evolution equation will be given

$$\frac{\partial \widehat{P}(\chi_0,\Omega_0|\chi,\Omega,t)}{\partial t} = \widehat{\Gamma}(\chi)\widehat{P}(\chi_0,\Omega_0|\chi,\Omega,t) + \sum_{\chi'} \widehat{k}_{\chi,\chi'}(\Omega)\widehat{P}(\chi_0,\Omega_0|\chi',\Omega,t), \tag{4.12}$$

which have the same form as Eqs. (4.4), however, with the operators and functions involved replaced by the symmetrized version. The symmetrized conditional probabilities can be used to calculate the correlation functions by the relation

$$\begin{aligned}\phi^{LL'}_{mm'nn'}(t) &= \iint d\Omega_0 d\Omega D^{L}_{m,n}(\Omega_0) D^{L'*}_{m',n'}(\Omega) P^{1/2}_{eq}(\Omega_0) P^{1/2}_{eq}(\Omega)\widehat{P}(\chi_0,\Omega_0|\chi,\Omega,t) \\ \phi_{a_i a_j}(t) &= \iint d\Omega_0 d\Omega a_i(\chi_0)\widehat{P}(\chi_0,\Omega_0|\chi,\Omega,t) P^{1/2}_{eq}(\Omega_0) P^{1/2}_{eq}(\Omega) a_j(\chi).\end{aligned} \tag{4.13}$$

4.2 Eigenfunction expansion

The evolution equation for the conditional probability function can be solved using the eigenfunction expansion as developed in [27–29]. Expanding each function $P(\chi_0,\Omega_0|\chi,\Omega,t)$ in a series of normalized Wigner functions $\mathscr{D}^{L}_{m,n}(\Omega) = \sqrt{(2L+1)/(8\pi^2)}D^{L}_{m,n}(\Omega)$ we obtain:

$$\widehat{P}(\chi_0,\Omega_0|\chi,\Omega,t) = \sum_{L,m,n} C^{L}_{m,n}(\chi_0,\Omega_0;\chi,t)\mathscr{D}^{L}_{m,n}(\Omega). \tag{4.14}$$

The dual space of the normalized Wigner functions is defined by: $\mathscr{D}^{L*}_{m,n}(\Omega) = \sqrt{(2L+1)/(8\pi^2)}D^{L*}_{m,n}(\Omega)$ with inner product:

$$\int d\Omega \mathscr{D}^{L'*}_{m',n'}(\Omega)\mathscr{D}^{L}_{m,n}(\Omega) = \delta_{L',L}\delta_{m',m}\delta_{n',n}. \tag{4.15}$$

Substituting the equations (4.14) in (4.12) we will obtain:

$$\begin{aligned}\sum_{L,m,n} \frac{\partial}{\partial t} C^{L}_{m,n}(\chi_0,\Omega_0;\chi,t)\mathscr{D}^{L}_{m,n}(\Omega) &= \sum_{L,m,n} C^{L}_{m,n}(\chi_0,\Omega_0;\chi,t)\widehat{\Gamma}(\chi)\mathscr{D}^{L}_{m,n}(\Omega) \\ &+ \sum_{\chi',L,m,n} C^{L}_{m,n}(\chi_0,\Omega_0;\chi',t)\widehat{k}_{\chi\chi'}(\Omega)\mathscr{D}^{L}_{m,n}(\Omega).\end{aligned} \tag{4.16}$$

Multiplying both sides of the equation by $\mathscr{D}^{L'*}_{m',n'}(\Omega)$ and integrating in $d\Omega$ and

performing the summation on the r.h.s we will obtain:

$$\frac{\partial}{\partial t} C^{L'}_{m',n'}(\chi_0, \Omega_0; \chi, t) = \sum_{L,m,n} \widehat{\mathbf{G}}_{L',m',n';L,m,n}(\chi) C^{L}_{m,n}(\chi_0, \Omega_0; \chi, t) + \sum_{\chi',L,m,n} \widehat{\mathbf{K}}_{L',m',n';L,m,n}(\chi, \chi') C^{L}_{m,n}(\chi_0, \Omega_0; \chi', t), \tag{4.17}$$

where

$$\widehat{\mathbf{G}}_{L',m',n';L,m,n}(\chi) = \int d\Omega \mathscr{D}^{L'*}_{m',n'}(\Omega) \widehat{\Gamma}_{\chi}(\Omega) \mathscr{D}^{L}_{m,n}(\Omega), \tag{4.18}$$

and

$$\widehat{\mathbf{K}}_{L',m',n';L,m,n}(\chi, \chi') = \int d\Omega \mathscr{D}^{L'*}_{m',n'}(\Omega) \widehat{k}_{\chi\chi'}(\Omega) \mathscr{D}^{L}_{m,n}(\Omega). \tag{4.19}$$

We can collect all the coefficients related to the shape χ in the column vector

$$\mathbf{C}(\chi) = \begin{bmatrix} C^{0}_{0,0}(\chi_0, \Omega_0; \chi, t) \\ \vdots \\ C^{3}_{-2,2}(\chi_0, \Omega_0; \chi, t) \\ \vdots \\ C^{L}_{m,n}(\chi_0, \Omega_0; \chi, t), \end{bmatrix} \tag{4.20}$$

and further organize them in the block column vector

$$\mathbf{C} = \begin{bmatrix} \mathbf{C}(\chi_1) \\ \mathbf{C}(\chi_2) \\ \vdots \\ \mathbf{C}(\chi_n) \end{bmatrix}. \tag{4.21}$$

Proceeding with the formalism, we can organize the operators in a block matrix

$$\widehat{\mathbf{R}} = \begin{bmatrix} \widehat{\mathbf{G}}(\chi_1) + \mathbf{K}(\chi_1, \chi_1) & \mathbf{K}(\chi_1, \chi_2) & \dots & \mathbf{K}(\chi_1, \chi_n) \\ \mathbf{K}(\chi_2, \chi_1) & \widehat{\mathbf{G}}(\chi_1) + \mathbf{K}(\chi_2, \chi_2) & \dots & \mathbf{K}(\chi_2, \chi_n) \\ \vdots & \vdots & \ddots & \vdots \\ \mathbf{K}(\chi_n, \chi_1) & \mathbf{K}(\chi_n, \chi_2) & \dots & \widehat{\mathbf{G}}(\chi_n) + \mathbf{K}(\chi_n, \chi_n) \end{bmatrix}, \tag{4.22}$$

and write equation (4.17) as:

$$\frac{\partial}{\partial t}\mathbf{C} = \widehat{\mathbf{R}}\mathbf{C}. \tag{4.23}$$

Since $\widehat{\mathbf{R}}$ is symmetric, there is a unitary matrix $\widehat{\mathbf{X}}$ that:

$$\widehat{\mathbf{R}}\widehat{\mathbf{X}} = \widehat{\mathbf{X}}\widehat{\mathbf{r}}, \tag{4.24}$$

where $\widehat{\mathbf{r}}$ is a diagonal matrix. Left multiplying the equation by $\widehat{\mathbf{X}}^T$ and reorganizing the terms we obtain

$$\frac{\partial}{\partial t}\left(\widehat{\mathbf{X}}^T\mathbf{C}\right) = \widehat{\mathbf{X}}^T\widehat{\mathbf{R}}\widehat{\mathbf{X}}\left(\widehat{\mathbf{X}}^T\mathbf{C}\right). \tag{4.25}$$

Defining $\widehat{\mathbf{C}} = \widehat{\mathbf{X}}^T\mathbf{C}$, we can write

$$\frac{\partial}{\partial t}\widehat{\mathbf{C}} = \widehat{\mathbf{r}}\widehat{\mathbf{C}}. \tag{4.26}$$

Since the matrix $\widehat{\mathbf{r}}$ is diagonal, each element of $\widehat{\mathbf{C}}$ is connected just to itself, as a consequence, the set of linear differential equation will have as solution:

$$\widehat{\mathbf{C}}(t) = e^{\widehat{\mathbf{r}}t}\widehat{\mathbf{C}}(t=0), \tag{4.27}$$

which can be transformed back to the original form by the relations $\mathbf{C} = \widehat{\mathbf{X}}\widehat{\mathbf{C}}$. Proceeding this way we obtain

$$\mathbf{C}(t) = \widehat{\mathbf{X}}e^{\widehat{\mathbf{r}}t}\widehat{\mathbf{X}}^T\mathbf{C}(t=0). \tag{4.28}$$

Therefore, each element of the vectors is given by

$$C^{L}_{m,n}(\chi_0,\Omega_0;\chi,t) = \sum_{K,\chi',L',m',n'} \widehat{\mathbf{X}}_{\chi,L,m,n;K}\left[e^{\widehat{\mathbf{r}}t}\right]_K \widehat{\mathbf{X}}_{K;\chi',j',p',q'} C^{j'}_{p',q'}(\chi_0,\Omega_0;\chi',t=0), \tag{4.29}$$

where $K = \{\chi'', L'', m'', n''\}$ and the summation is performed over all possible values. Applying the initials conditions (4.8), we have

$$C^{j}_{p,q}(\chi_0,\Omega_0;\chi,t=0) = \mathscr{D}^{j*}_{p,q}(\Omega)\delta_{\chi_0,\chi},$$

which can be replace in Eq. (4.29) obtain:

$$C^{L}_{m,n}(\chi_0,\Omega_0;\chi,t) = \sum_{K,\chi',L',m',n'} \widehat{\mathbf{X}}_{\chi,L,m,n;K}\left[e^{\widehat{\mathbf{r}}t}\right]_K \widehat{\mathbf{X}}_{K;\chi',j',p',q'} \mathscr{D}^{j'*}_{p',q'}(\Omega_0)\delta_{\chi',\chi_0}. \tag{4.30}$$

The coefficients from Eq. (4.30) can substituted in Eq. (4.14) to give

$$\begin{aligned}\widehat{P}(\chi_0,\Omega_0|\chi,\Omega,t) = \frac{1}{8\pi^2}\sum_{K}\sum_{j,p,q}\sum_{j',p',q'}\sqrt{(2j+1)(2j'+1)} \\ \times \widehat{\mathbf{X}}_{\chi,j,p,q;K}\widehat{\mathbf{X}}_{\chi_0,j',p',q';K}\left[e^{\widehat{\mathbf{r}}t}\right]_K D^{j}_{p,q}(\Omega)D^{j'*}_{p',q'}(\Omega_0).\end{aligned} \tag{4.31}$$

As $t \to \infty$ all exponentials decay to 0 except the values with $\mathbf{r}_K = 0$, which can be identified with the equilibrium value. Therefore we have

$$\begin{aligned}\lim_{t\to\infty}\widehat{P}(\chi_0,\Omega_0|\chi,\Omega,t) &= P^{1/2}_{eq}(\chi,\Omega)P^{1/2}_{eq}(\chi_0,\Omega_0) \\ &= \frac{1}{8\pi^2}\sum_{j'',p'',q''}\sum_{\chi''',j''',p''',q'''}\sqrt{(2j''+1)(2j'''+1)} \\ &\times \widehat{\mathbf{X}}_{\chi,j'',p'',q'';0}\widehat{\mathbf{X}}_{\chi_0,j''',p''',q''';0}D^{j''}_{p'',q''}(\Omega)D^{j'''*}_{p''',q'''}(\Omega_0),\end{aligned} \tag{4.32}$$

where we used $K = 0$ to identify the index of the equilibrium value.

Substituting Eq. (4.32) and Eq. (4.31) in (4.13) and performing some algebraic

simplifications, we obtain

$$\begin{aligned}
\phi^{LL'}_{mm'nn'}(t) = &\sum_K \sum_{\chi,\chi_0} \sum_{j,p,q} \sum_{j',p',q'} \sum_{j'',j'''} \widehat{\mathbf{X}}_{\chi,j,p,q;K} \widehat{\mathbf{X}}_{\chi_0,j',p',q';K} \\
&\frac{\sqrt{(2j''+1)(2j'''+1)(2j+1)(2j'+1)}}{(2L+1)(2L'+1)} \widehat{\mathbf{X}}_{\chi,j'',m'-p,n'-q;0} \\
&\times \widehat{\mathbf{X}}_{\chi_0,j''',m-p',n-p';0} C(j,j'',L';p,m'-p) C(j,j'',L';q,n'-q) \\
&\times \left[e^{\widehat{\mathbf{r}}t}\right]_K C(j',j''',L;p',m-p') C(j',j''',L;q',n-q')
\end{aligned} \tag{4.33}$$

To obtain the axial $\phi_{a_i,a_j}(t)$ correlation functions we can substitute Eq. (4.32) and Eq. (4.31) in Eqs. (4.13) and simplify the Clebsch-Gordan coefficients $C(j,j',0;p,-p) = \delta_{j,j'}(-1)^{j-m}/\sqrt{2j+1}$ to give

$$\begin{aligned}
&\phi_{a_i,a_j}(t) = \\
&\sum_K \left(\sum_{\chi_0} \sum_{j',p',q'} \widehat{\mathbf{X}}_{\chi_0,j',p',q';K} \widehat{\mathbf{X}}_{\chi_0,j',-p',-q';0} a_i(\chi_0) \right) \\
&\left[e^{\widehat{\mathbf{r}}t}\right]_K \left(\sum_{\chi} \sum_{j,p,q} \widehat{\mathbf{X}}_{\chi_0,j,p,q;K} \widehat{\mathbf{X}}_{\chi,j,-p,-q;0} a_j(\chi) \right).
\end{aligned} \tag{4.34}$$

The solution to the proposed equation is formally exact, but it involves the evaluation of an infinite number of matrix elements. For practical use, we can truncate the expansion in Wigner functions after a certain number of elements, and evaluate the operators numerically. Compared with the algorithm we developed in the chapter 3, this algorithm is mathematically more cumbersome and the generalization to cases where there is a rotation-shape switching is far from trivial. However, it has the advantage of requiring the diagonalization of the matrix $\hat{\mathbf{R}}$ just once for all values of $\{L,L',m,m',n,n'\}$. Moreover, for the biaxial potential, the matrix generated by this algorithm is much smaller than the one it would be required by the finite differences method. We believe the advantages overplay the difficulties.

4.2.1 Shape change operator

In this section we will obtain in details the elements of the shape transition operator. The elements for $\widehat{\mathbf{K}}(\chi,\chi')$ where $\chi \neq \chi'$ can be obtained substituting the first

case of Eq. (4.11) in (4.19) and performing the integration in Ω to obtain

$$\widehat{\mathbf{K}}_{L',m',n';L,m,n}(\chi,\chi') = \zeta(\chi,\chi')\delta_{L,L'}\delta_{m,m'},\delta_{n,n'} \quad \forall \quad \chi \neq \chi', \tag{4.35}$$

while the elements of $\widehat{\mathbf{K}}(\chi,\chi')$ for $\chi = \chi'$ can be obtained substituting the second case of Eq. (4.11) in (4.19) to give

$$\begin{aligned}\widehat{\mathbf{K}}_{L',m',n';L,m,n}(\chi,\chi) = -\sum_{\chi'\neq\chi}\zeta(\chi',\chi)\int d\Omega P_{eq}^{-1/2}(\chi,\Omega) \\ \times P_{eq}^{1/2}(\chi'\Omega)\mathscr{D}^{L'}_{m',n'}(\Omega)\mathscr{D}^{L'*}_{m',n'}(\Omega).\end{aligned} \tag{4.36}$$

The elements of this matrix could be calculated evaluating the integral in equations (4.35) and (4.36) for each element of $\widehat{\mathbf{K}}$, but it is computationally unfeasible due to the high number of elements in the matrix. To avoid this problem we will reduce drastically the number of integrals expanding the exponential in a combination of Wigner functions, where we can take advantage of the orthogonality of the function space.

Therefore, we can rewrite the exponentials $P_{eq}^{-1/2}(\chi,\Omega)P_{eq}^{1/2}(\chi',\Omega)$ as

$$\begin{aligned}P_{eq}^{-1/2}(\chi,\Omega)P_{eq}^{1/2}(\chi',\Omega) = \sqrt{\frac{p_0(\chi)}{p_0(\chi')}}e^{-\Delta u^2_{0,0}(\chi,\chi')D^2_{0,0}(\Omega)} \\ \times e^{-\Delta u^2_{2,0}(\chi,\chi')\left(D^2_{0,0}(\Omega)+D^2_{-2,0}(\Omega)\right)},\end{aligned} \tag{4.37}$$

where

$$\Delta u^l_{mn}(\chi,\chi') = \frac{u^l_{m,n}(\chi') - u^l_{m,n}(\chi)}{2}. \tag{4.38}$$

Since our potential is a limited function, with no singularities we can expand each potential in series of functions and combine then later.

The exponential $\exp[-\Delta u^2_{2,0}(\chi,\chi')\left(D^2_{2,0}(\Omega)+D^2_{-2,0}(\Omega)\right)]$ is a analytic function of its arguments, consequently, we can expand it in a Maclaurin series relative to the

potential coefficients $\Delta u^{l}_{m,n}(\chi,\chi')$ with terms given by

$$\exp\left[-\Delta u^2_{2,0}(\chi,\chi')D^2_{2,0}(\Omega)-\Delta u^2_{2,0}(\chi,\chi')D^2_{-2,0}(\Omega)\right]= \sum_{j=0}^{\infty}\frac{(-1)^j}{j!}\left[\Delta u^2_{2,0}(\chi,\chi')\left(D^2_{2,0}(\Omega)+D^2_{-2,0}(\Omega)\right)\right]^j, \tag{4.39}$$

where each terms within brackets can be further expanded using the binomial series:

$$\left[\Delta u^2_{2,0}(\chi,\chi')\left(D^2_{2,0}(\Omega)+D^2_{-2,0}(\Omega)\right)\right]^j= \sum_{k_1+k_2=j}\frac{j!}{k_1!k_2!}\Delta u^2_{2,0}(\chi,\chi')^j D^2_{2,0}(\Omega)^{k_1}D^2_{-2,0}(\Omega)^{k_2} \tag{4.40}$$

Since we are summing in j from 0 to ∞, we can reorganize the series as

$$\exp\left[-\Delta u^2_{2,0}(\chi,\chi')\left(D^2_{2,0}(\Omega)+D^2_{-2,0}(\Omega)\right)\right]= \sum_{k_1=0}^{\infty}\sum_{k_2=0}^{\infty}\frac{(-1)^{k_1+k_2}}{k_1!k_2!}\Delta u^2_{2,0}(\chi,\chi')^{k_1+k_2}D^2_{2,0}(\Omega)^{k_1}D^2_{-2,0}(\Omega)^{k_2}. \tag{4.41}$$

Each Wigner function raised to some power k can be recursively expanded using a Clebsch-Gordan series. For our specific case, we have the functions $D^2_{2,0}(\Omega)$ and $D^2_{-2,0}(\Omega)$ raised to some power, performing some algebraic work we can show that for any k the recurrent Clebsch-Gordan expansions reduce to the following expressions

$$\begin{aligned} D^2_{2,0}(\Omega)^{k_2} &= \Upsilon(k_2)D^{2k_2}_{2k_2,0}(\Omega) \\ D^2_{-2,0}(\Omega)^{k_3} &= \Upsilon(k_3)D^{2k_3}_{-2k_3,0}(\Omega) \end{aligned} \tag{4.42}$$

where

$$\Upsilon(k)\equiv\begin{cases} 1 \quad \text{if} \quad k=0 \\ \prod_{i=1}^{k} C(2,2k-2,2k;0,0)C(2,2k-2,2k;2,2k-2), \end{cases}$$

where $C(i,j,k,l,m)$ are Clebsch-Gordan coefficients.

Finally, substituting equations (4.42) into Eq. (4.41) we obtain

$$\exp\left[-\Delta u_{2,0}^2(\chi,\chi')\left(D_{2,0}^2(\Omega)+D_{-2,0}^2(\Omega)\right)\right] = \sum_{k_1=0}^{\infty}\sum_{k_2=0}^{\infty}\Upsilon(k_1) \times \Upsilon(k_2)\frac{(-1)^{k_2+k_3}}{k_1!k_2!}\Delta u_{2,0}^2(\chi,\chi')^{k_1+k_2}D_{2k_1,0}^{2k_1}(\Omega)D_{-2k_2,0}^{2k_2}(\Omega). \quad (4.43)$$

Unfortunately, we cannot use the same technique in the term $\exp[\left(-\Delta u_{0,0}^2(\chi,\chi')D_{0,0}^2(\Omega)\right)]$, since the functions $D_{0,0}^2(\Omega)^k$ cannot be reduced to an expression as simple as Eq. (4.42). As an alternative, we can express the exponential directly as a series of Wigner functions, given by

$$e^{\left(-\Delta u_{0,0}^2(\chi,\chi')D_{0,0}^2(\Omega)\right)} = \sum_{i=0}^{\infty}\Lambda^i(\chi,\chi')D_{0,0}^{2i*}(\Omega) \quad (4.44)$$

where

$$\Lambda^i(\chi,\chi') \equiv \frac{4i+1}{8\pi^2}\int d\Omega e^{\left(-\Delta u_{0,0}^2(\chi,\chi')D_{0,0}^2(\Omega)\right)}D_{0,0}^{2i*}(\Omega). \quad (4.45)$$

Since $D_{0,0}^2(\Omega)$ is independent of α and γ, any integral in Eq. (4.45) with $m \neq 0$ and $n \neq 0$ is identically 0. The same results holds for terms with L odd, because the exponential argument is an even function.

Combining Eq. (4.44) with (4.43) we obtain

$$\exp\left[-\Delta u_{0,0}^2(\chi,\chi')D_{0,0}^2(\Omega)-\Delta u_{2,0}^2(\chi,\chi')\left(D_{2,0}^2(\Omega)+D_{-2,0}^2(\Omega)\right)\right] = \sum_{i=0}^{\infty}\sum_{j=0}^{\infty}\sum_{k=0}^{\infty}\frac{(-1)^{j+k}}{j!k!}\Lambda^i(\chi,\chi')\Upsilon(j)\Upsilon(k)\Delta u_{2,0}^2(\chi,\chi')^{j+k}D_{0,0}^{2i}(\Omega)D_{2j,0}^{2j}(\Omega)D_{-2k,0}^{2k}(\Omega).$$

We can further reduce the product of the three Wigner functions using Clebsch-Gordan coefficients:

$$\exp\left[-\Delta u_{0,0}^2(\chi,\chi')D_{0,0}^2(\Omega)-\Delta u_{2,0}^2(\chi,\chi')\left(D_{2,0}^2(\Omega)+D_{-2,0}^2(\Omega)\right)\right] = \sum_{i=0}^{\infty}\sum_{j=0}^{\infty}\sum_{k=0}^{\infty}\sum_{L=|j-k|}^{j+k}\sum_{L'=|L-i|}^{L+i}\frac{(-1)^{j+k}}{j!k!}\Lambda(\Delta U_{0,0}^2,i)\Upsilon(j)\Upsilon(k)\Delta u_{2,0}^2(\chi,\chi')^{j+k}C(2i,2L,2L';0,0) \times C(2i,2L,2L';0,2j-2k)C(2j,2k,2L;0,0)C(2j,2k,2L;2j,-2k)D_{2j-2k,0}^{2L'}(\Omega). \quad (4.46)$$

Formally, equation (4.46) is already the solution that we wanted, since it involves summation of terms containing a single Wigner function without being raised to any power. However, the terms are summed in random order. This can be avoided rearranging the summation in the following form

$$
\begin{aligned}
e^{-\Delta u^2_{0,0}(\chi,\chi')D^2_{0,0}(\Omega)} e^{-\Delta u^2_{2,0}(\chi,\chi')\left(D^2_{2,0}(\Omega)+D^2_{-2,0}(\Omega)\right)} = \\
\sum_{L'=0}^{\infty}\sum_{m=-L'}^{L'}\sum_{k=max(0,-m)}^{\infty}\sum_{L=|m|}^{m+2k}\sum_{i=|L-L'|}^{L'+L}\frac{(-1)^{m+2k}}{(m+k)!k!}\Lambda(\chi,\chi')^i \\
\times\Upsilon(m+k)\Upsilon(k)\Delta u^2_{2,0}(\chi,\chi')^{m+2k}C(2i,2L,2L';0,0) \\
\times C(2m+2k,2k,2L;0,0)C(2i,2L,2L';0,2m) \\
\times C(2m+2k,2k,2L;2m+2k,-2k)D^{2L'}_{2m,0},
\end{aligned}
\tag{4.47}
$$

which allows us to define the elements

$$
\begin{aligned}
\Xi^{L'}_{m'}(\chi,\chi') = \sum_{k=max(0,-n')}^{\infty}\sum_{L=|n'|}^{n'+2k}\sum_{i=|L-L'|}^{L'+L}\frac{(-1)^{m+2k}}{(m+k)!k!}\Lambda^i(\chi,\chi') \\
\times\Upsilon(m+k)\Upsilon(k)\Delta u^2_{2,0}(\chi,\chi')^{m+2k}C(2i,2L,2L';0,0) \\
\times C(2m+2k,2k,2L;0,0)C(2i,2L,2L';0,2m) \\
\times C(2m+2k,2k,2L;2m+2k,-2k),
\end{aligned}
\tag{4.48}
$$

therefore, we can cast Eq. (4.47) in the much simpler form

$$
\begin{aligned}
e^{-\Delta u^2_{0,0}(\chi,\chi')D^2_{0,0}(\Omega)} e^{-\Delta u^2_{2,0}(\chi,\chi')\left(D^2_{2,0}(\Omega)+D^2_{-2,0}(\Omega)\right)} = \\
\sum_{L=0}^{\infty}\sum_{m=-L}^{L}\Xi^L_m(\chi,\chi')D^{2L}_{2m,0}(\Omega).
\end{aligned}
\tag{4.49}
$$

The elements of the shape operator $\widehat{\mathbf{K}}_{L',m',n';L,m,n}(\chi,\chi)$ can be obtained substituting Eq. (4.49) in Eq. (4.36) giving

$$
\begin{aligned}
\widehat{\mathbf{K}}_{L',m',n';L,m,n}(\chi,\chi) = -\sum_{\chi'\neq\chi}\sum_{L''=0}^{\infty}\sum_{m''=-L''}^{L''}\sqrt{\frac{p_0(\chi)}{p_0(\chi')}} \\
\times\sqrt{\frac{2L+1}{2L'+1}}\Xi^{L''}_{m''}(\chi,\chi')C(2L'',L,L',2m'',m) \\
\times C(2L'',L,L',0,n)\delta_{m'-m,2m''}\delta_{n,n'}.
\end{aligned}
\tag{4.50}
$$

Finally, we can simplify the Kronecker deltas to obtain

$$\begin{aligned}\widehat{\mathbf{K}}_{L',m',n';L,m,n}(\chi,\chi) &= 0 \quad \text{if} \quad m-m' \quad \text{odd},\\ \widehat{\mathbf{K}}_{L',m',n';L,m,n}(\chi,\chi) &= 0 \quad \text{if} \quad n\neq n',\end{aligned} \tag{4.51}$$

otherwise

$$\begin{aligned}\widehat{\mathbf{K}}_{L',m',n';L,m,n}(\chi,\chi) = &-\sum_{\chi'\neq\chi}\sum_{L''}\zeta(\chi',\chi)\sqrt{\frac{p_0(\chi)}{p_0(\chi')}}\\ &\times\sqrt{\frac{2L+1}{2L'+1}}C(2L'',L,L',m'-m,m)\\ &\times C(2L'',L,L',0,n)\Xi^{L''}_{(m'-m)/2}(\chi,\chi').\end{aligned} \tag{4.52}$$

The solution we presented here is formally exact, but each element of $\Xi^{L''}_{(m'-m)/2}(\chi,\chi')$ involves summation of infinite terms.

4.2.2 Roto-diffusion operator

In this section we will develop in detail the elements of the operators performing the roto-diffusion, derived in Eq. (4.9). The full version of $\hat{\Gamma}(\chi)$ can be obtained substituting Eq. (4.9) in Eq. (4.18) as follows:

$$\begin{aligned}\widehat{\mathbf{G}}_{L',m',n';L,m,n}(\chi) = \int d\Omega\mathscr{D}^{L'*}_{m',n'}(\Omega)\Big\{&-D^{\chi}_{\perp}\mathbf{L}^2-\left(D^{\chi}_{\parallel}-D^{\chi}_{\perp}\right){L_z}^2-\frac{D^{\chi}_{\perp}}{2}\mathbf{L}^2u(\chi,\Omega)\\ &+\frac{D^{\chi}_{\perp}}{4}L_+u(\chi,\Omega)L_-u(\chi,\Omega)-\frac{1}{2}\left(D^{\chi}_{\parallel}-D^{\chi}_{\perp}\right){L_z}^2u(\chi,\Omega)\\ &+\frac{1}{4}D^{\chi}_{\parallel}\left(L_zu(\chi,\Omega)\right)^2\Big\}\mathscr{D}^{L}_{m,n}(\Omega)\end{aligned} \tag{4.53}$$

The evaluation of Eq. (4.54) is possible, but however inconvenient due to high number of operators involved. We can simplify the expression using the linearity of

the integral operator:

$$\begin{aligned}\widehat{\mathbf{G}}_{L',m',n';L,m,n}(\chi) = &-D_{\perp}^{\chi}\int d\Omega \mathscr{D}^{L'*}_{m',n'}(\Omega)\mathbf{L}^2\mathscr{D}^{L}_{m,n}(\Omega)\\ &-\left(D_{\parallel}^{\chi}-D_{\perp}^{\chi}\right)\int d\Omega \mathscr{D}^{L'*}_{m',n'}(\Omega){L_z}^2\mathscr{D}^{L}_{m,n}(\Omega)\\ &-\frac{D_{\perp}^{\chi}}{2}\int d\Omega \mathscr{D}^{L'*}_{m',n'}(\Omega)\mathbf{L}^2 u(\chi,\Omega)\mathscr{D}^{L}_{m,n}(\Omega)\\ &+\frac{D_{\perp}^{\chi}}{4}\int d\Omega \mathscr{D}^{L'*}_{m',n'}(\Omega)L_+ u(\chi,\Omega)L_- u(\chi,\Omega)\mathscr{D}^{L}_{m,n}(\Omega)\\ &-\frac{1}{2}\left(D_{\parallel}^{\chi}-D_{\perp}^{\chi}\right)\int d\Omega \mathscr{D}^{L'*}_{m',n'}(\Omega){L_z}^2 u(\chi,\Omega)\mathscr{D}^{L}_{m,n}(\Omega)\\ &+\frac{1}{4}D_{\parallel}^{\chi}\int d\Omega \mathscr{D}^{L'*}_{m',n'}(\Omega)\left(L_z u(\chi,\Omega)\right)^2\mathscr{D}^{L}_{m,n}(\Omega),\end{aligned} \tag{4.54}$$

in this way instead of evaluating the elements of Eq. (4.54) as a whole, we will evaluate each term in the sum separately and combined them afterwards.

Furthermore, the evaluation of $\hat{\Gamma}(\chi)$ requires the application of a series of quantum angular momentum operators on Wigner functions, that can be obtained by the following rules [50]

$$\begin{aligned}&\mathbf{L}^2 D^{L}_{m,n}(\Omega) = L(L+1)D^{L}_{m,n}(\Omega)\\ &L_z D^{L}_{m,n}(\Omega) = nD^{L}_{m,n}(\Omega)\\ &L_{\pm}D^{L}_{m,n}(\Omega) = \sqrt{L(L+1)-n(n\pm 1)}D^{L}_{m,n\pm 1}(\Omega).\end{aligned} \tag{4.55}$$

Applying these rules to the integral operators, gives

$$\int d\Omega \mathscr{D}^{L'*}_{m',n'}(\Omega)\mathbf{L}^2\mathscr{D}^{L}_{m,n}(\Omega) = L(L+1)\delta(L',L)\delta(m',m)\delta(n',n) \tag{4.56}$$

$$\int d\Omega \mathscr{D}^{L'*}_{m',n'}(\Omega)L_z^2\mathscr{D}^{L}_{m,n}(\Omega) = n^2\delta(L',L)\delta(m',m)\delta(n',n) \tag{4.57}$$

$$\begin{aligned}\int d\Omega \mathscr{D}^{L'*}_{m',n'}(\Omega)\left[\mathbf{L}^2 u(\chi,\Omega)\right]\mathscr{D}^{L}_{m,n}(\Omega) = &\sqrt{\frac{2L+1}{2L'+1}}\sum_{L_u,m_u,n_u} u^{L_u}_{m_u,n_u}(\chi,\Omega)[L_u(L_u+1)]\\ &\times C(L,L_u,L',n,n_u)C(L,L_u,L',m,m_u)\delta(m',m+m_u)\delta(n',n+n_u)\end{aligned} \tag{4.58}$$

$$\int d\Omega \mathscr{D}^{L'*}_{m',n'}(\Omega)\left[{L_z}^2 u(\chi,\Omega)\right]\mathscr{D}^{L}_{m,n}(\Omega) = \sqrt{\frac{2L+1}{2L'+1}} \sum_{L_u,m_u,n_u} u^{L_u}_{m_u,n_u}(\chi)\, n_u^2$$
$$\times C(L,L_u,L',n,n_u)C(L,L_u,L',m,m_u)\delta(m',m+m_u)\delta(n',n+n_u) \tag{4.59}$$

$$\int d\Omega \mathscr{D}^{L'*}_{m',n'}(\Omega)\left[L_z u(\chi,\Omega)\right]^2\mathscr{D}^{L}_{m,n}(\Omega) = \sqrt{\frac{2L+1}{2L'+1}} \sum_{L_u,m_u,n_u}\sum_{L_{u'},m_{u'},n_{u'}} u^{L_{u'}}_{m_{u'},n_{u'}}(\chi)u^{L_u}_{m_u,n_u}(\chi)$$
$$\times n_{u'}n_u \sum_{J=|L_u-L_{u'}|}^{L_u+L_{u'}} C(L_u,L_{u'},J,n_{u'},n_u)C(L_u,L_{u'},J,m_{u'},m_u)C(L,J,L',n,n_u+n_{u'})$$
$$\times C(L,J,L',m,m_u+m_{u'})\delta(m',m+m_u+m_{u'})\delta(n',n+n_u+n_{u'}) \tag{4.60}$$

$$\int d\Omega \mathscr{D}^{L'*}_{m',n'}(\Omega)[L_- u(\chi,\Omega)L_+ u(\chi,\Omega)]\mathscr{D}^{L'*}_{m',n'}(\Omega) = \sqrt{\frac{2L+1}{2L'+1}} \sum_{L_u,m_u,n_u}\sum_{L_{u'},m_{u'},n_{u'}} u^{L_{u'}}_{m_{u'},n_{u'}}(\chi)$$
$$\times u^{L_u}_{m_u,n_u}(\chi) \sum_{J=|L_u-L_{u'}|}^{L_u+L_{u'}} \sqrt{L_u(L_u+1)-n_u(n_u-1)}\sqrt{L_{u'}(L_{u'}+1)-n_{u'}(n_{u'}+1)}$$
$$\times C(L_u,L_{u'},J,n_{u'}+1,n_u-1)C(L_u,L_{u'},J,m_{u'},m_u)C(L,J,L',n,n_u+n_{u'})$$
$$\times C(L,J,L',m,m_u+m_{u'})\delta(m',m+m_u+m_{u'})\delta(n',n+n_u+n_{u'}). \tag{4.61}$$

Finally, combining all the terms we gives

$$\begin{aligned}
\widehat{\mathbf{G}}_{L',m',n';L,m,n}(\chi) = &-k1\sqrt{\frac{1+2L}{1+2L'}}C(L,4,L',n,0)C(L,4,L',m,-4)\delta_{',m-4} \\
&-k2\sqrt{\frac{1+2L}{1+2L'}}C(L,2,L',n,0)C(L,2,L',m,-2)\delta_{m',m-2} \\
&-k3\sqrt{\frac{1+2L}{1+2L'}}C(L,4,L',n,0)C(L,4,L',m,-2)\delta_{m',m-2} \\
&-k4\sqrt{\frac{1+2L}{1+2L'}}C(L,2,L',n,0)C(L,4,L',m,0)\delta_{m',m} \\
&-k5\sqrt{\frac{1+2L}{1+2L'}}C(L,4,L',n,0)C(L,4,L',m,0)\delta_{m',m} \\
&-\left[k6+D_{\perp}^{\chi}L(L+1)-(D_{\parallel}^{\chi}-D_{\perp}^{\chi})n^2\right]\delta_{m',m}\delta_{L',L} \\
&-k2\sqrt{\frac{1+2L}{1+2L'}}C(L,2,L',n,0)C(L,2,L',m,2)\delta_{m',m-2} \\
&-k3\sqrt{\frac{1+2L}{1+2L'}}C(L,4,L',n,0)C(L,4,L',m,2)\delta_{m',m+2} \\
&-k1\sqrt{\frac{1+2L}{1+2L'}}C(L,4,L',n,0)C(L,4,L',m,4)\delta_{m',m+4}
\end{aligned} \tag{4.62}$$

where we substituted numerical values of the Clebsch-Gordon coefficients and simplified the Kronecker when possible. We also organized all the constants in the coefficients k:

$$\begin{aligned}
k_1 &= -3\sqrt{\frac{2}{35}}u_{2,0}^2(\chi)^2 D_{\perp}^{\chi} \\
k_2 &= -\frac{3}{7}\left(-7+u_{0,0}^2(\chi)\right)u_{2,0}^2(\chi)D_{\perp}^{\chi} \\
k_3 &= -\frac{6}{7}u_{0,0}^2(\chi)u_{2,0}^2(\chi)D_{\perp}^{\chi} \\
k_4 &= \frac{3}{14}(u_{0,0}^2(\chi)(14+u_{0,0}^2(\chi)-2u_{2,0}^2(\chi)^2)D_{\perp}^{\chi} \\
k_5 &= -\frac{6}{35}\left(3u_{0,0}^2(\chi)^2\right)D_{\perp}^{\chi} \\
k_6 &= \frac{3}{10}(u_{0,0}^2(\chi)^2+2u_{2,0}^2(\chi)^2)D_{\perp}^{\chi}.
\end{aligned} \tag{4.63}$$

4.3 Numerical Implementation details

Until now, all the results we have are exact, even though in practice it is not possible to evaluate some of the equations we obtained, since they involve either the evaluation of infinite terms in a summation, or the diagonalization of a infinitely large square matrix. Here we will develop a numerical procedure to solve the system of equations. The basic idea behind the computer algorithm is to truncate both series in Eq. (4.14) and (4.47) after a finite number of elements. The operators are evaluated for the chosen elements and the transition matrix in Eq. (4.22) is filled. With the finite transition matrix we can perform the calculations specified in section 4.2.

In general, the total algorithm precision depends on the combination of errors in the truncation of Eq. (4.14) and Eq. (4.47). For the former, the number of required coefficients grows with the mean field potential constants $u^l_{m,n}$. For the values of potentials studied in this chapter, the algorithm showed good precision and efficiency if we take elements in the series until $L = 12$, $m = 8$ and $n = 8$.

In the evaluation of the shape transition matrix, the number of terms necessary to attain a certain precision grows with the potential difference $\Delta u^2_{2,0}(\chi, \chi')$. To evaluate these series, we found it computationally more efficient to use Eq. (4.46), determining the maximum values for i, j, k and accumulate the terms in the elements of Ξ^L_m.

The integrals in $\Lambda(\chi', \chi)$ were performed using the Romberg integration [73] implemented in the Scypy library version 0.18.1. We used the *eigh* routine provided by the same library to diagonalize the transition matrix.

Even though the solution obtained in Eq. (4.33) is formally correct, it is unsuitable for numerical computations due to the elevate number of indexes in the summations. We can proceed as Tarroni and Zannoni [28], thus defining the vector

$$\begin{aligned} V^L_{m,n}(K) = \sum_{\chi_0} \sum_{j'''} \sum_{j',p',q'} \Bigg(& \frac{\sqrt{(2j'+1)(2j'''+1)}}{2L+1} \\ & \times \widehat{\mathbf{X}}_{\chi_0,j',p',q';K} C(j', j''', L; q', n-q') \\ & \times \widehat{\mathbf{X}}_{\chi_0,j''',m-p',n-q';0} C(j', j''', L; p', m-p') \Bigg), \end{aligned} \tag{4.64}$$

and rearranging the summation in the following form

$$\phi^{LL'}_{mm'nn'}(t) = \sum_K V^L_{m,n}(K) \left[e^{\hat{\mathbf{r}}t} \right]_K V^{L'}_{m',n'}(K). \tag{4.65}$$

In this way, we can calculate each element of $V^L_{m,n}(K)$ separately, which involves summation over only 5 indexes. Note also that if we are interested in calculating a series of correlations function, for any type of index $\{L,m,n\}$ we need to calculate the vector $V^L_{m,n}(K)$ just once and store its values for future usage, improving the performance even further.

The same process can be applied to reorganize the summations involved in Eq. (4.34) to speed up numerical calculations. For this aim, we define the vector

$$V_{a_j}(K) = \sum_\chi \sum_{j,p,q} \widehat{\mathbf{X}}_{\chi_0,j,p,q;K} \widehat{\mathbf{X}}_{\chi,j,-p,-q;0} a_j(\chi), \tag{4.66}$$

in order to rewrite $\phi_{a_i,a_j}(t)$ as

$$\phi_{a_i,a_j}(t) = \sum_K V_{a_i}(K) \left[e^{\hat{\mathbf{r}}t} \right]_K V_{a_j}(K). \tag{4.67}$$

We can use this formalism to evaluate also the correlation times. Substituting Eq. (4.65) in Eq. (2.26), performing the integral over t and simplifying the results, we obtain

$$\tau^{LL'}_{mm',nn'} = \sum_{K\neq 0} \frac{V^L_{m,n}(K) V^{L'}_{m',n'}(K)}{[\widehat{\mathbf{r}}]_K}. \tag{4.68}$$

Repeating the process to the axial correlation time gives

$$\tau_{a_i,a_j} = \sum_{K\neq 0} \frac{V_{a_i}(K) V_{a_j}(K)}{[\widehat{\mathbf{r}}]_K}. \tag{4.69}$$

We can test the precision of the algorithm by two complementary methods. The first method, is to inspect the maximum eigenvalue of the transition matrix $\widehat{\mathbf{R}}$. The second method is to compare the asymptotically solution for the equation (4.65) when $t = 0$ and $t \to \infty$ with the static values computed by Eqs.(2.30) and (2.31) with the integrals performed by another numerical package (in our case, we used Mathematica

and Scypy).

4.4 Model parameters

To proceed we need to define the values for the parameters used in the model. Even though, we are not interested to fit any particular case; in order to product a set of plausible values, we will use existing theories to estimate the model constants whenever possible.

The rotational diffusion of particle solvated in fluid with viscosity coefficient γ can be estimated using the Perrin-Einstein relations [71, 72], which are obtained solving the Stokes-Einstein equation with stick boundary conditions. For a sphere with radius R, the roto-diffusion coefficient $D^s(R)$ is given by

$$D^s(R) = \frac{k_B T}{8\pi\gamma R^3}. \tag{4.70}$$

For particles with anisotropic shape, we will have different coefficients for different axes, for instance, a uniaxial ellipsoid have two of them , one parallel $D_\parallel$ and one perpendicular $D_\perp$ to its axes of symmetry.

The equations for the coefficients take different forms depending on the aspect ratio $\rho \equiv a_\perp / a_\parallel$. For a prolate ellipsoid ($\rho < 1$) roto-diffusion coefficient parallel to the director $D_\parallel^{prolate}$ is given by

$$\frac{D_\parallel^{prolate}}{D^s(d)} = \frac{3}{2(1-\rho^2)} \left\{ 1 - \frac{\rho^2}{\sqrt{1-\rho^2}} \ln \left[\frac{1+\sqrt{1-\rho^2}}{\rho} \right] \right\} \tag{4.71}$$

while the coefficient perpendicular to the director $D_\perp^{prolate}$ by

$$\frac{D_\perp^{prolate}}{D^s(d)} = \frac{3\rho^2}{2(1-\rho^4)} \left[\frac{2-\rho^2}{\sqrt{1-\rho^2}} \ln \left\{ \frac{1+\sqrt{1-\rho^2}}{\rho} \right] - 1 \right\}, \tag{4.72}$$

where $D^s(d)$ is the roto-diffusion of a sphere with hydrodynamic radius $d = \sqrt[3]{a_\perp{}^2 a_\parallel}$.

For an oblate ellipsoid ($\rho > 1$), the roto-diffusion coefficients parallel to the sym-

metry axis is given by

$$\frac{D_{\parallel}^{oblate}}{D^s(d)} = \frac{3}{2(1-\rho^2)}\left[1 - \frac{\rho^2}{\sqrt{\rho^2-1}}\arctan\left(\sqrt{\rho^2-1}\right)\right] \tag{4.73}$$

and the perpendicular roto-diffusion $D_{\perp}^{oblate}$ by

$$\frac{D_{\perp}^{oblate}}{D^s(d)} = \frac{3\rho^2}{2(1-\rho^4)}\left[\frac{2-\rho^2}{\sqrt{\rho^2-1}}\arctan\left(\sqrt{\rho^2-1}\right) - 1\right]. \tag{4.74}$$

To the best of our knowledge, there is no analytic expression to obtain effective potential as a function of the solute particle shape, however we can use the method developed in the previous chapter to make an estimate of the shape-dependence of the effective parameter $u^2_{0,0}(\chi)$. Since we are studying the effect of the environment biaxiality on the experimental observables, instead of estimating also $u^2_{2,0}(\chi)$, here we will take

$$u^2_{2,0}(\chi) = \lambda u^2_{0,0}(\chi) \tag{4.75}$$

where λ will be used as a free parameter. In this way, we can analyse the effect of the extra interaction in the correlation functions and correlations times, and consequently in the experimental observables.

4.5 Results

As in chapter 3, our particle can assume three shapes: a sphere, a prolate and a oblate ellipsoid. In all three shapes the axis lengths were chosen to give an unitary hydrodynamics radius $d(\chi) = 1$. We also assume that any shape can switch to any shape as sketched in figure 4.1 and that the exchange-ratio is equal for all transitions, i.e $\zeta(\chi,\chi') = \zeta$ for all χ and χ'. Since we are interested in the general properties of the proposed model, we can make the analyses much more convenient performing the following set of transformations:

$$t^* = D^s t, \qquad \zeta^*(\chi,\nu) = \zeta(\chi,\nu),$$
$$D_{\parallel}^{\chi*} = D_{\parallel}^{\chi}/D^s, \qquad D_{\perp}^{\chi,*} = D_{\perp}^{\chi}/D^s.$$

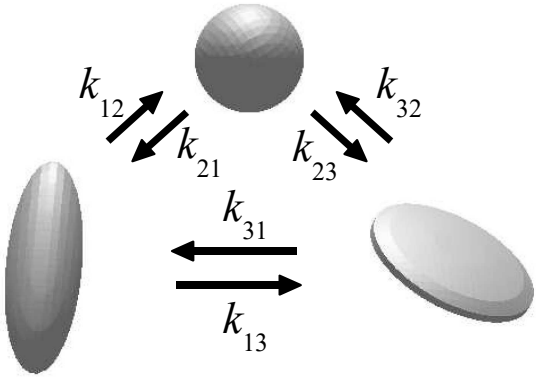

Figure 4.1: Sketch of shape switching process.

.

Table 4.1: Parameters used in the numerical calculations.

χ	Shape	$a_\perp$	$a_\parallel$	$D_\perp^\chi$	$D_\parallel^\chi$	$u_{0,0}^2$
Prolate	1	0.69	2.08	0.42	1.35	-3.85
Sphere	2	1.00	1.00	1.00	1.00	0.00
oblate	3	1.59	0.40	0.54	0.44	2.36

The parameters for each shape can be visualized in Tab. 4.1. For the numerical algorithm, we took Wigner functions until $L_{max} = 12, n_{max} = m_{max} = 8$ and $i_{max} = 12, j_{max} = k_{max} = 8$ for the shape transition operator. With these values, the biggest equilibrium eigenvalue was $\hat{\mathbf{r}}_K \approx 10^{-8}$.

In our first group of analyses, we kept the intrinsic shape distribution constant and varied the exchange ratio ζ^* and the biaxiality λ. We chose three values for ζ^*, giving different shape-exchange regime relatively to the roto-diffusion: 0.1 (one scale slower), 1.0 (same scale) and 10.0 (one scale faster). For λ we chose the values $\lambda = \{0, 0.15, 0.3\}$. We call attention to the fact that a $\lambda = 0.0$ represents an uniaxial sample, while the maximum value possible for λ is $1/\sqrt{6}$. The first rank correlation functions can be seen in Fig. 4.2 and the second rank in Fig. 4.3.

We can separate the correlation functions in families by their general features. Functions like $\phi_{00,00}^{LL}$ are modulated only by β angle, therefore, they show the same fast and slow shape transition regime reported for the uniaxial potential in chapter 3. However, here the curves shapes are mildly altered by the biaxiality λ.

Other functions with characteristic behaviour are $\phi_{L-L,nn}^{LL}$. They are intrinsically 0 in absence of biaxiality and their shapes are strongly dependent on λ. Even though

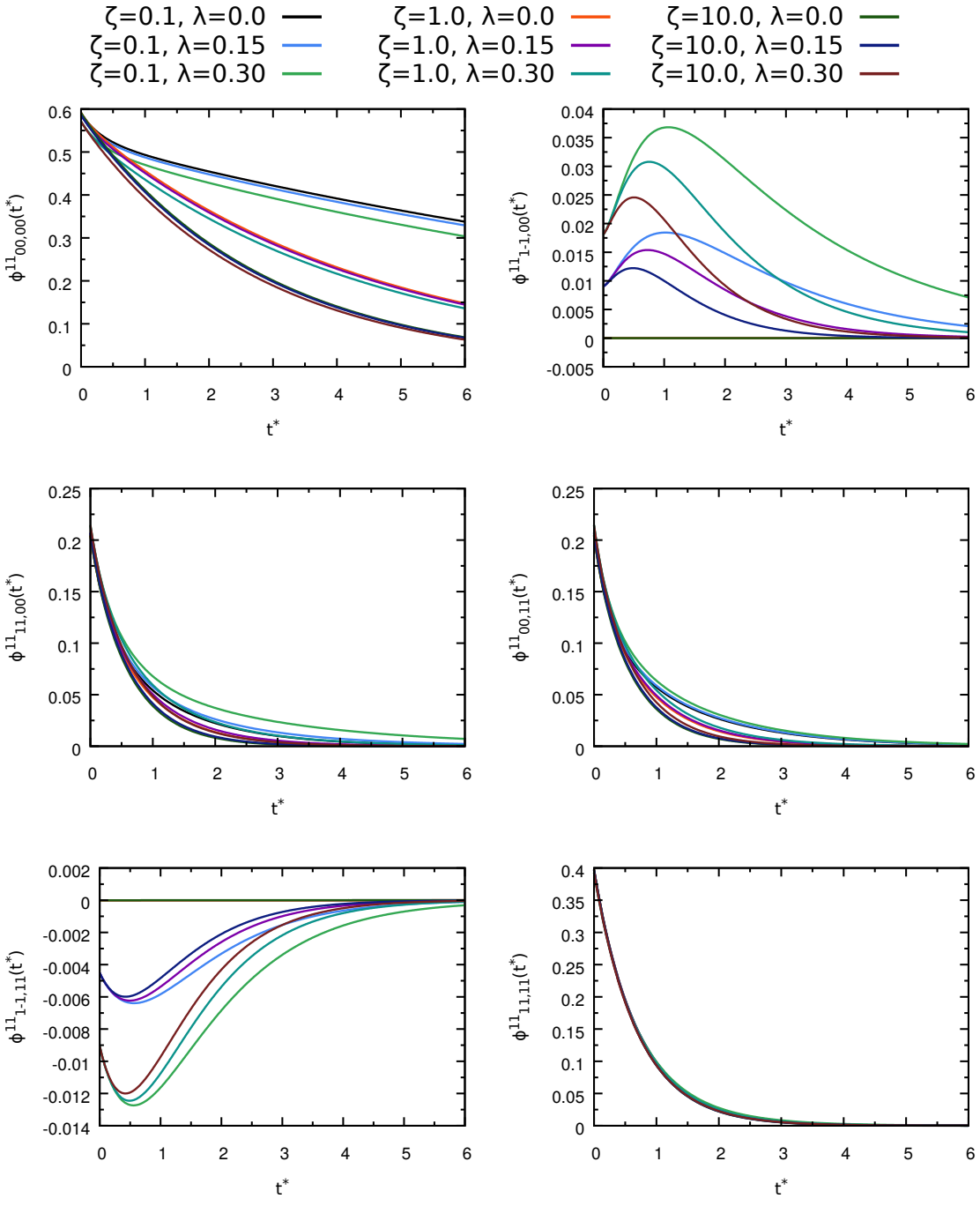

Figure 4.2: First order correlation functions. In all calculations we used $p_0(\chi) = 1/3$ for all shapes.

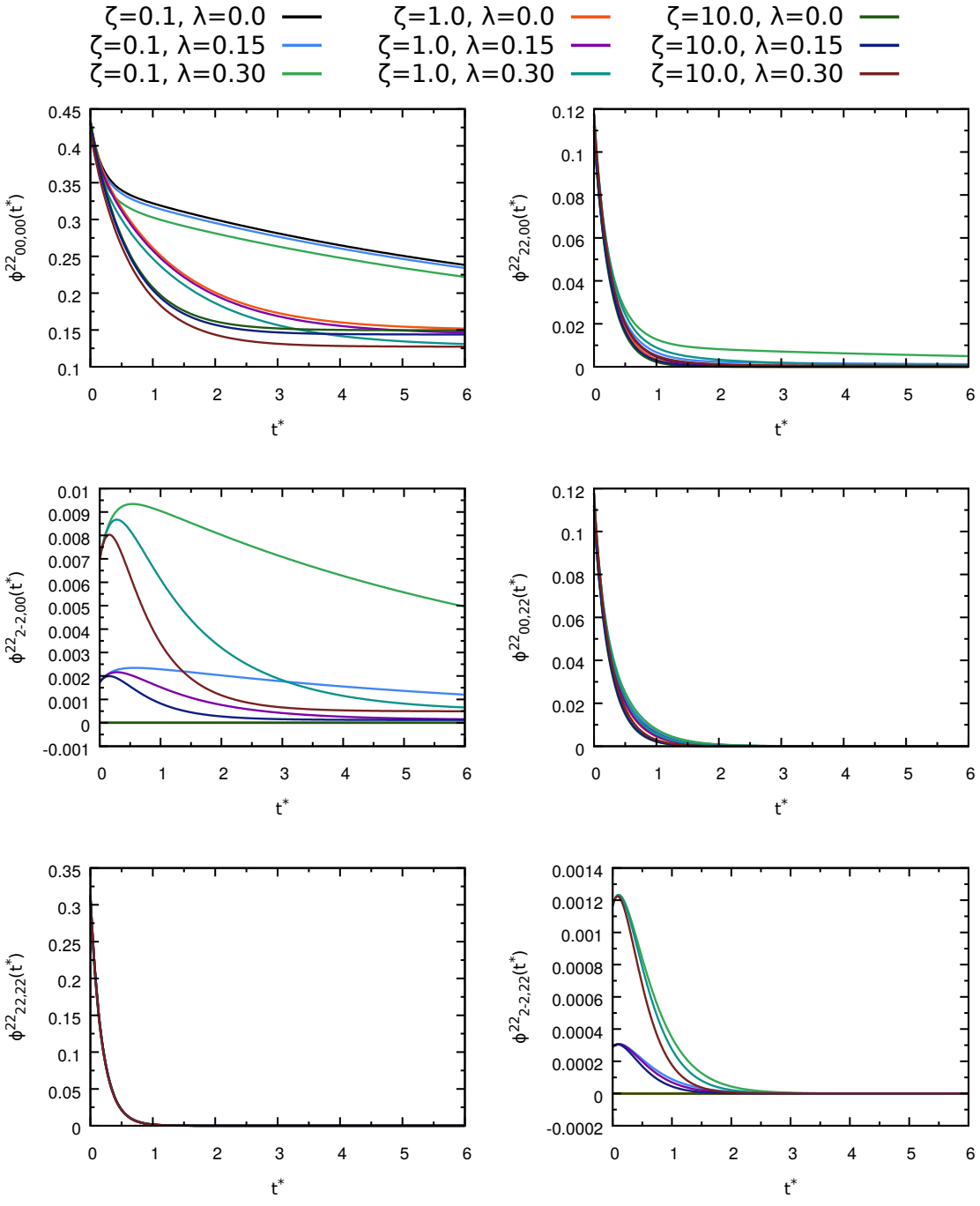

Figure 4.3: Second order correlation functions. In all calculations we used $p_0(\chi) = 1/3$ for all shapes.

they also show fast and slow diffusion regimes when $\zeta^* >> 1$ and $\zeta^* << 1$, as the index n increases the different regimes become less distinguishable due to the modulation by the Euler angle γ.

Another group of functions are formed by $\phi^{LL}_{LL,00}$ and $\phi^{LL}_{00,LL}$. Here we can not distinguish the fast and slow relaxation regimes, although the shape of the correlation functions is weak dependent on λ. As expected, set $\phi^{LL}_{mm,00}$ modulated by γ is more dependent on λ.

Surprisingly, the fourth family of correlation functions $\phi^{LL}_{LL,LL}$ are almost independent of exchange ratio and biaxiality λ.

In the second part of our analyses, we let the exchange ratio ζ^* constant while we varied $p_0(\chi)$ and λ. All three shapes have completely distinct dynamics; therefore, we expect the dynamics and static behaviour of all correlation functions to be dependent on p_0. In order to consider only some representative examples, without loosing generality, we are going to always keep $p_0(\text{disk}) = p_0(\text{sphere})$ while varying $p_0(\text{rod})$. The results can be visualized in two sets of figures: the first order correlation functions can be seen in Fig. 4.4 and the second order can be seen in Fig. 4.5

The biggest visible difference is when $m = -m'$, where each correlation function show a very distinct behavior. For instance, the shape of the first rank seems more dependent on $p_0(\chi)$, while the second rank is mainly dependent on the biaxiality λ.

Again the shape of the correlation functions $\phi^{11}_{11,11}(t)$ and $\phi^{22}_{22,22}(t)$ shows little dependence on p_0, and consequently little to none dependence on biaxiality λ. We deduce that deconvoluting data from these correlation function in a noise experiment will be harder, if not unfeasible.

The remaining correlation functions show similar behaviour. If we take the same index, the functions which share the same distribution $p_0(\chi)$ possess very similar behaviour, while the biaxiality acts as a perturbation. If these are the only correlation functions available experimentally, we expect the shape effects to be visible, however the information about the biaxiality parameter λ will be hard to obtain.

In the last part of our analyses, we are going to investigate the relaxation times of the correlation functions. Even though the shape of the correlation curves gives an idea of the relaxation process, the correlation times provides numerical values that we can use for comparison. The correlation times of some selected correlation

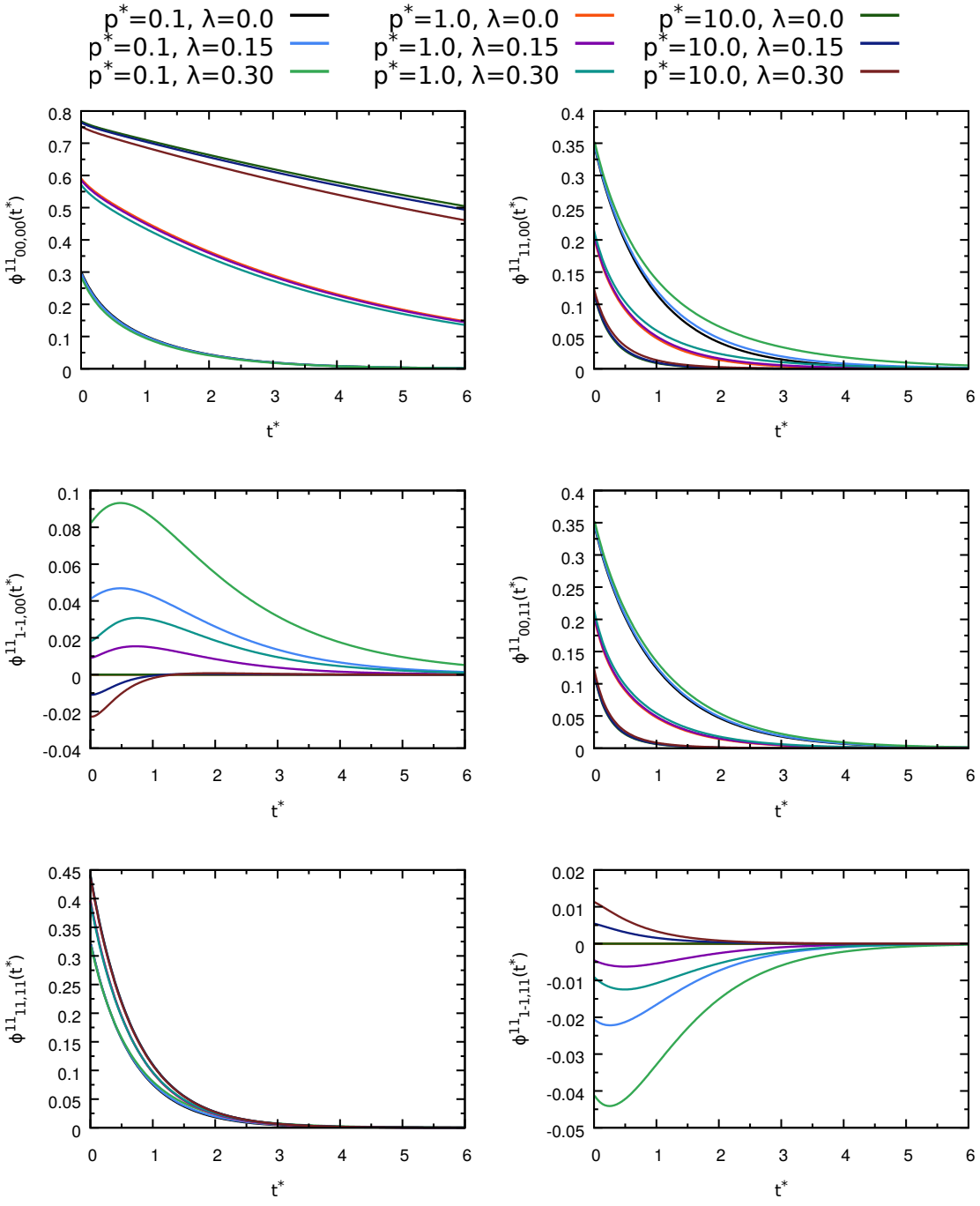

Figure 4.4: First rank correlation functions calculate for various values of p_0 and $\zeta^* = 1.0$.

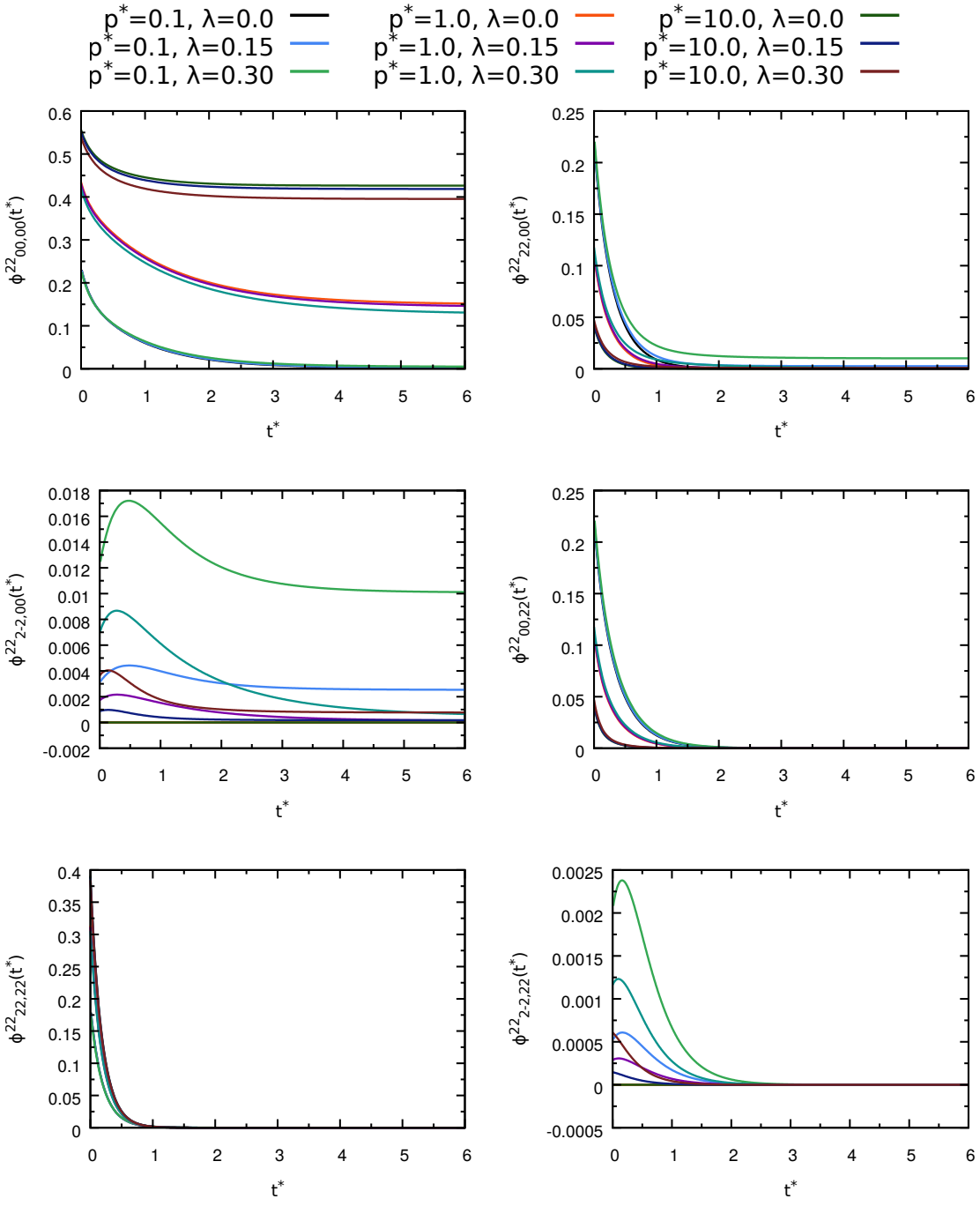

Figure 4.5: Second rank correlation functions calculated for various values of p_0 and $\zeta^* = 1.0$.

functions can be found in figure 4.6

Before we start, is important to state that the direct comparison of correlations times absolute values associates with functions with different indexes can lead to errors due to their difference in scale, for instance $\phi^{22}_{00,00}$ is two order of magnitude bigger than $\phi^{22}_{2-2,00}$. In the correlation times, we can observe all the similar trends we identified for the correlations functions, but we can also directly evaluate the interplay between ζ^* and p^*_0.

The correlation times show better than any other parameter the complexity of the problem we are dealing with. In general, the correlation times are strongly dependent on p_0. All correlation function functions that showed clearly fast and slow regime relaxation process are, of course, strongly dependent on ζ^*, while λ can be disregarded. The parameter λ plays an important role in the relaxation with $m = -m'$ and on a minor scale in $\tau^{LL}_{00,nn}$ with $n \neq 0$.

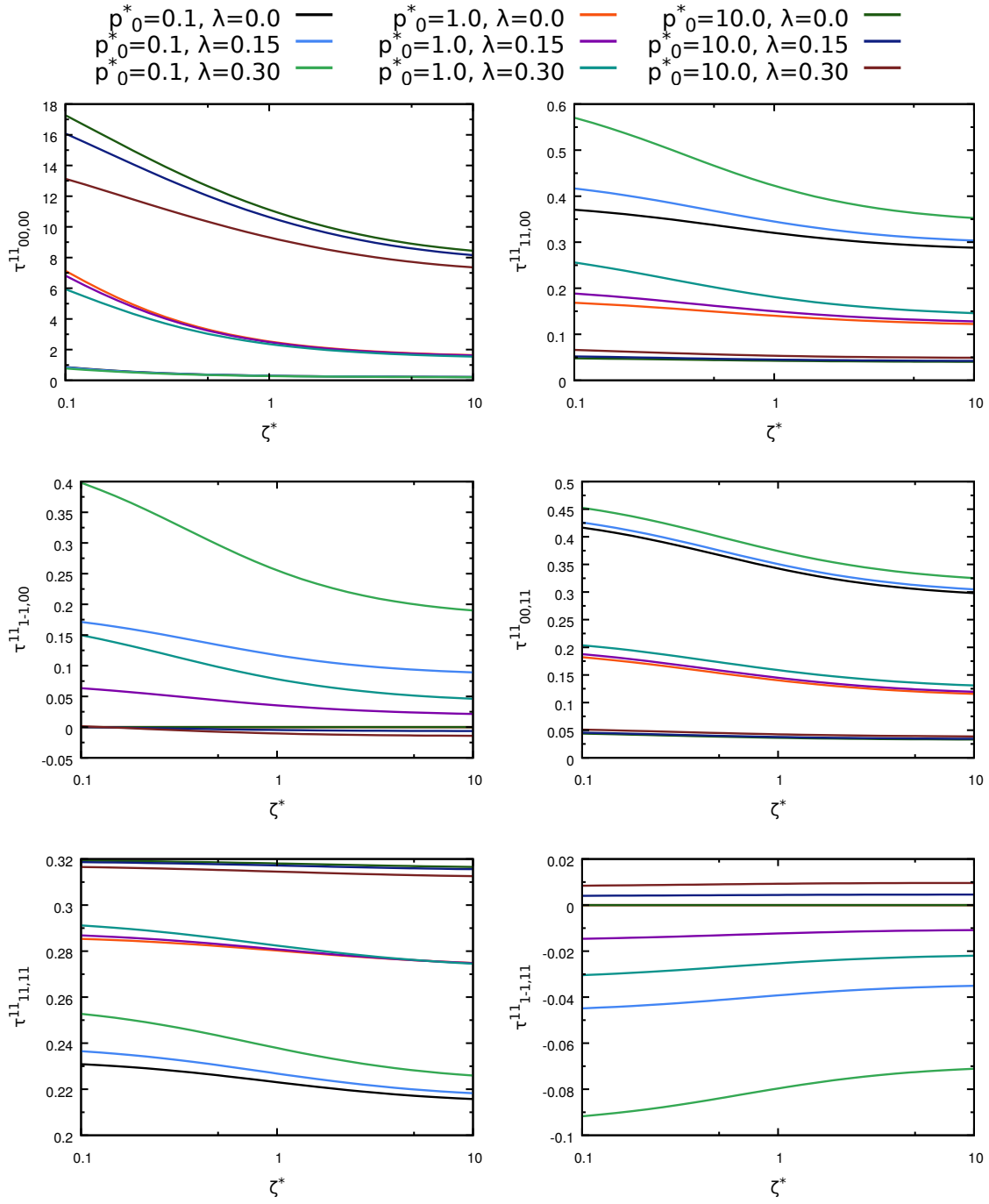

Figure 4.6: First rank correlation times.

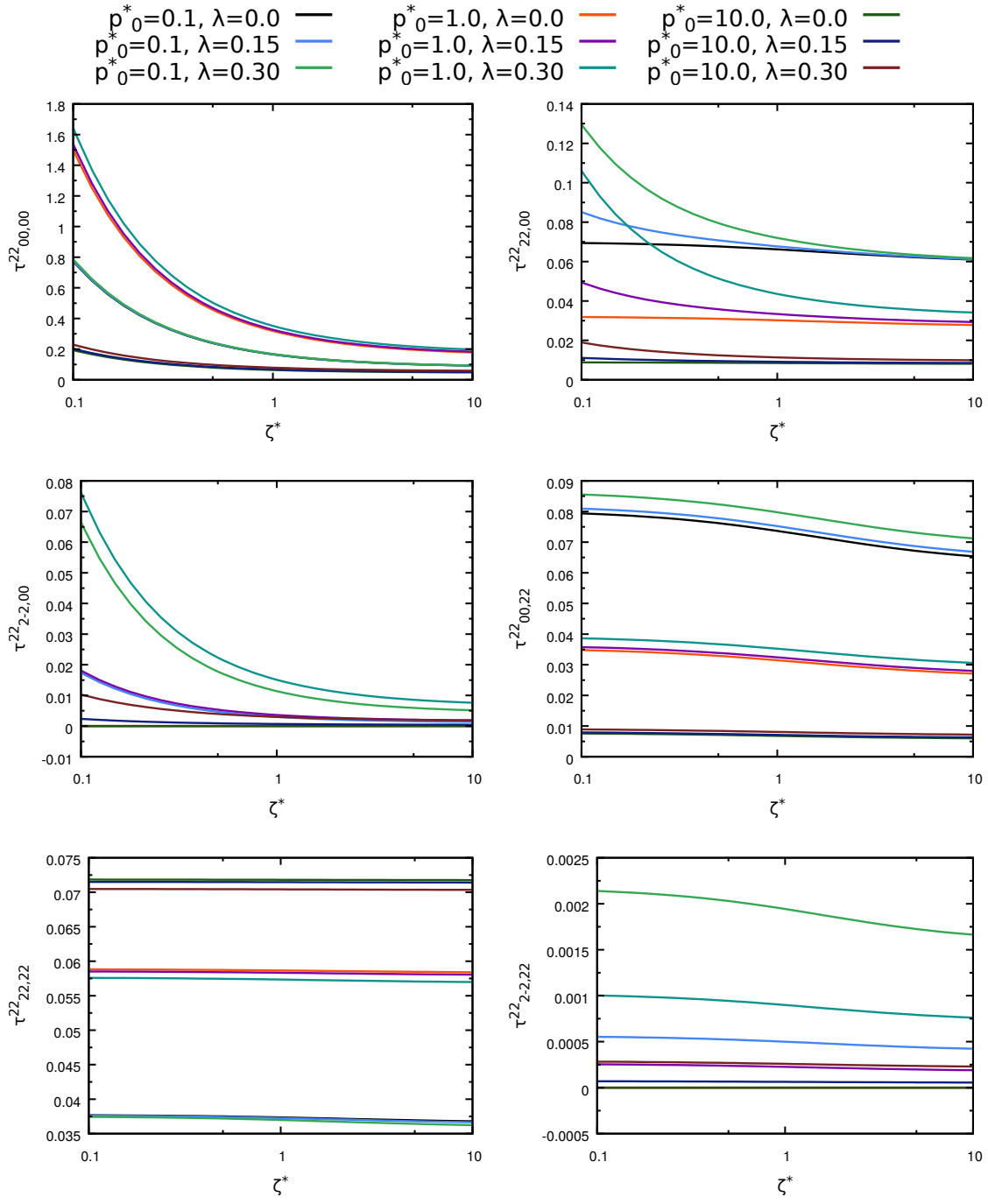

Figure 4.7: Second rank correlation times.

Part II

Active particles

Chapter 5

Introduction to Molecular Dynamics Simulations

The formation of non-equilibrium ordered structures in system of active, self-propelled particles or living individuals systems is a fascinating topic, that has recently received much attention for isotropic and anisotropic systems [13, 74].

Currently, there is no universal framework which can capture the complexity of all kinds of active systems. However, some theories are being developed which attempt to provide an unified description based on the conserved quantities and on the system symmetries. Models in which the total momentum is conserved, denominated "wet", take into account the exchange of moment between the active particles and the environment. This framework is generally used to study synthetic particles dispersed in different types of medium, for instance, active gels [74].

In the so called "dry" models, there is no momentum conservation due to a friction with the substrate [74]. Some living systems are studied in this framework, for example, flow of bacterial suspensions, flocks of birds and schools of fishes[1] [75]. Dry models are also used to study synthetic systems such as systems of granular rods subjected to a outside shocking [13].

A continuum type theory description of the macroscopic properties of active systems can be obtained within the framework of non-equilibrium statistical mechanics. For instance, the flow of a low density suspension of active particles can be investigated by coarse-graining a modified version of Boltzmann equation [74, 76]. In partic-

[1] Is really sarcastic that the models used to study school of fishes are classified as "dry".

ular, the hydrodynamic of systems of self-propelled rods [77,78], active filaments [79], and active nematics [80] has been investigated by this methodology. One problem of the Boltzmann approach is that it works better when most of particle collisions are binary, however some interesting phenomena, like the formation of polar patterns need multi-particle collisions [81].

One alternative is to derive the hydrodynamics equations phenomenologically taking advantage of the system symmetries, using a procedure similar to the one used to derive the nematodynamics equations [1]. This approach provides a set of equations with a few free parameters, which can be used to fit the behaviour of specific systems. This framework, pioneered by Toner and Tu [82, 83], was successfully used to study active nematics [80, 84], nematic colloids [11, 85] and defect dynamics in active nematics [86]. One of its drawbacks is the absence of information about the free parameters or the microscopic behaviour which gives rise to it.

A complementary approach to either the Boltzmann and the phenomenological hydrodynamic ones is to use molecular dynamics simulations to model the system at the microscopic, particle, level. In this way, multi-particle collisions enter naturally in the particle dynamics and macroscopic properties can be computed using out of equilibrium statistical mechanics. Furthermore, the same framework can be used to study the order of the system and the emergence of self-organized structures.

The investigation of liquid crystal systems containing active particles appears particularly interesting for the combination of spontaneous order at equilibrium with dynamic effects due to the presence and action of self-propelled swimmers. Moreover, the long-range orientational order of liquid crystals can be used to guide the active particles in the sample, for example, the liquid crystal director can direct the swimming direction of bacteria [6] or even determine the trajectory of synthetic nanomotors [7].

In this chapter we will develop the theoretical framework necessary to describe active particles dissolved in liquid crystals, using molecular dynamics simulations.

5.1 Molecular Dynamics Simulations

Whenever we perform an experimental measurement of a physical observable A, we are in fact measuring the average of $A(t)$, whose values can and do fluctuate during the measurement. The average value of $A(t)$ can be obtained as

$$\bar{A}(t_0,t) = \frac{1}{\Delta t}\int_{t_0}^{t} A(t')dt'. \tag{5.1}$$

with $t - t_0 = \Delta t$ being the measurement time. The time dependence $\bar{A}(t_0,t)$ refers not only to the duration of the measurement, but also to the initial conditions t_0. As we increase the measurement time, the random fluctuations are averaged out, and the measurement of A becomes independent of time. In this way, as we increase t, we have:

$$\langle A\rangle_t \equiv \lim_{t\to\infty}\frac{1}{t}\int_{0}^{t} A(t')dt'. \tag{5.2}$$

Macroscopically, we can look at $A(t)$ as an observable which fluctuates from time to time. At microscopic level, however, we will see a system of particles evolving between many different states. Here we will refer to the state of a group of particles as Γ. In quantum systems, Γ is specified by the eigenstates of each particle, while for classical systems, it refers to set the coordinates of particles in the phase space.

The bridge between the macroscopic and microscopic descriptions is laid by statistical mechanics, whose main purpose is to derive the macroscopic behavior of a system based on the interaction of its constituents. In this way, if we know how to compute A as a function of Γ_t, whose time dependence is now implicit in the microscopic state, we can rewrite Eq. (5.2) as [87, 88]:

$$\langle A(\Gamma)\rangle_t \equiv \lim_{t\to\infty}\frac{1}{t}\int_{0}^{t} A(\Gamma_t)dt. \tag{5.3}$$

reducing the problem to the knowledge of the of Γ_t over the time t.

If our thermodynamic system is completely isolated from its surroundings, there will be no exchange of matter, volume or energy, therefore the number of particles N, the volume V and the energy E will be kept constant. In this case, we have no a priori reason to infer that one of the possibles micro states Γ is favoured over the others. Therefore, it is reasonable to suppose that after an infinitely long time, each micro

state will be visited an equal amount of time. As a consequence, we can substitute the time average in Eq. (5.3) with an average over all phase space given by

$$\langle A(\Gamma)\rangle_{\Gamma} \equiv \frac{\int_{\Gamma} A(\Gamma)\delta(E - H(\Gamma))d\Gamma}{\int_{\Gamma} \delta(E - H(\Gamma))d\Gamma}, \tag{5.4}$$

where δ is a Dirac delta and H is the system Hamiltonian, which will be discussed later. This is the so called micro-canonical ensemble, also called NVE ensemble[2].

Now suppose our system is constrained in volume V and has a fixed number of particles N, but is in thermal equilibrium with a reservoir at a temperature T. In this case, the energy E of our sample can fluctuate in time and, as a consequence, there will be no energy constraint in the micro states in which our system can be found. Furthermore, we cannot suppose that all micro states will be equally visited, since the presence of the thermal reservoir will favour some temperatures over others. If the thermal reservoir do not change its temperature while exchanging heat with the sample, the phase space average can be performed with the following equation:

$$\langle A(\Gamma)\rangle_{\Gamma} \equiv \frac{\int_{\Gamma} A(\Gamma)e^{-H(\Gamma)/k_B T}d\Gamma}{\int_{\Gamma} e^{-H(\Gamma)/k_B T}d\Gamma}, \tag{5.5}$$

where k_B is the Boltzmann constant, T is the temperature of the thermal reservoir and the integral is performed over the phase space Γ. This is called canonical ensemble or NVT ensemble. In a statistical sense, we are performing a weighted average, where the exponential $\exp[-H(\Gamma)/k_B T]$ is the weight of each micro state. For this reason, it is often called Boltzmann weight or measure.

In general, both the time integral in Eq. (5.3) and the ensemble averages in equations (5.5) and (5.4) can be treated analytically just for the simplest cases. A wide range of numerical methods were developed to tackle this problem. In this thesis, we shall derive the observables of interest from classical molecular dynamics simulations.

In molecular dynamics, we model the objects in the investigated system as classical particles interacting with each other by virtue of inter-particle potentials. Using one of the classical dynamic formalisms[3] we can set the equations of motion for each

[2]Most textbooks on molecular dynamics refer to the NVE convention.

[3]Newtonian, Lagrangian, Gaussian and Hamiltonian are some examples [89].

particle in our sample and solve them numerically.

Here we will use the Hamiltonian formalism, since it generates a first order set of differential equations and it deals naturally with constrained degrees of freedom. To model a system in this formalism, we need to specify the dynamic variables, called generalized coordinates $\mathbf{x}^i$ and generalized momentum $\mathbf{X}^i$, for each particle i. As a consequence, the micro state of a system composed by N particles can be specified as $\Gamma = \{\mathbf{x}^1, \mathbf{X}^1, \ldots, \mathbf{x}^N, \mathbf{X}^N\}$, and its Hamiltonian can be written as

$$H(\Gamma) = K(\Gamma) + U(\mathbf{x}^1, \cdots, \mathbf{x}^N) \tag{5.6}$$

Where $K(\Gamma)$ is the kinetic energy and $U(\mathbf{x}^1, \cdots, \mathbf{x}^N)$ is the system potential, which is assumed to depend only on the generalized coordinates $\mathbf{x}^1, \cdots, \mathbf{x}^i$. The dynamic evolution of the the elements of Γ are governed by the canonical equations

$$\begin{aligned} \frac{\partial}{\partial t} x^i_j &= \frac{\partial}{\partial X^i_j} H(\Gamma), \\ \frac{\partial}{\partial t} X^i_j &= -\frac{\partial}{\partial x^i_j} H(\Gamma). \end{aligned} \tag{5.7}$$

In this way, knowing the potential, the kinetic energy and the initial coordinates Γ_0, we can derive the dynamic variables Γ at any time t.

It is not possible to obtain an explicit solution for equations (5.7) which is continuous in time. Instead, given a initial state $\Gamma(t = 0)$, we can use a discretized version of Eqs. (5.7) to estimate the value of $\Gamma(t = \Delta t)$, where Δt is a small interval of time. We can repeat this procedure recursively and estimate $\Gamma(t = n\Delta t)$ for any finite integer value of n. With the values of Γ computed in discrete time intervals, we can evaluate the integral in Eq. (5.3) or, even better, the ensemble averages.

The solution of the system of Eqs. (5.7) provides a time sequence of micro states. Moreover, the micro states will be visited with equal probability in the micro-canonical ensemble, while they will be populated according to a Boltzmann distribution in the canonical ensemble. If we possess a large number N of micro states, we can estimate the values of any $\langle A \rangle_\Gamma$ of both Eq. (5.5) and Eq .(5.4) by

$$\langle A(\Gamma) \rangle_\Gamma \approx \frac{1}{N} \sum_{i=1}^{N} A\left(\Gamma(i\Delta t)\right). \tag{5.8}$$

Even though the problem is simple to define, its solutions are not trivial to obtain. A typical macroscopic thermodynamic system is composed by a number of molecules of the order of 10^{23}. Actually, the storage of this amount of information is technically prohibitive. Moreover, even if we were able to store all the data, its manipulation would pose another problem. Assuming only pairwise interactions as the best case scenario, a system composed of N molecules requires the calculation of $\sim N^2/2$ pairwise terms and the solution of system of $\sim N$ ordinary differential equations, which is only feasible for systems composed of up to a few millions of particles, sufficient to get good estimates of observable properties.

The sample size problem related to the number of particles can be tackled by using approximate techniques to find numerical solutions. In the next sections we will discuss the principal numerical methods available and, in particular, those used in this work. A brief overview of other methods is also provided for completeness. More detailed explanations and a discussion of a wider range of methods can be found in references [87, 88, 90].

5.2 Modelling rigid particles

In active systems, the component particles have typical sizes which can range from the nanometre to the micrometer scale, with the possibility of being composed of thousands of atoms [91]. The description of a system of active particles at an atomistic level of detail is impossible to achieve with the current computational power. Therefore, instead of treating particles as a collection of atoms, we will use coarse-grained models with a reduced number of interaction sites.

Several types of coarse-grained models are available, which vary depending on the level of description provided. In the united atoms approach, we remove the light and fast moving atoms, (typically hydrogen atoms) and include their effect directly into the heavier atom they are bound to. This level of description can be successfully used to model big organic molecules [92], but it is still too detailed for dealing with the kind of systems we aim to study.

The computational cost of a model can be further reduced by representing a molecule as a set of interacting sites, which is known as a site-site potential [88].

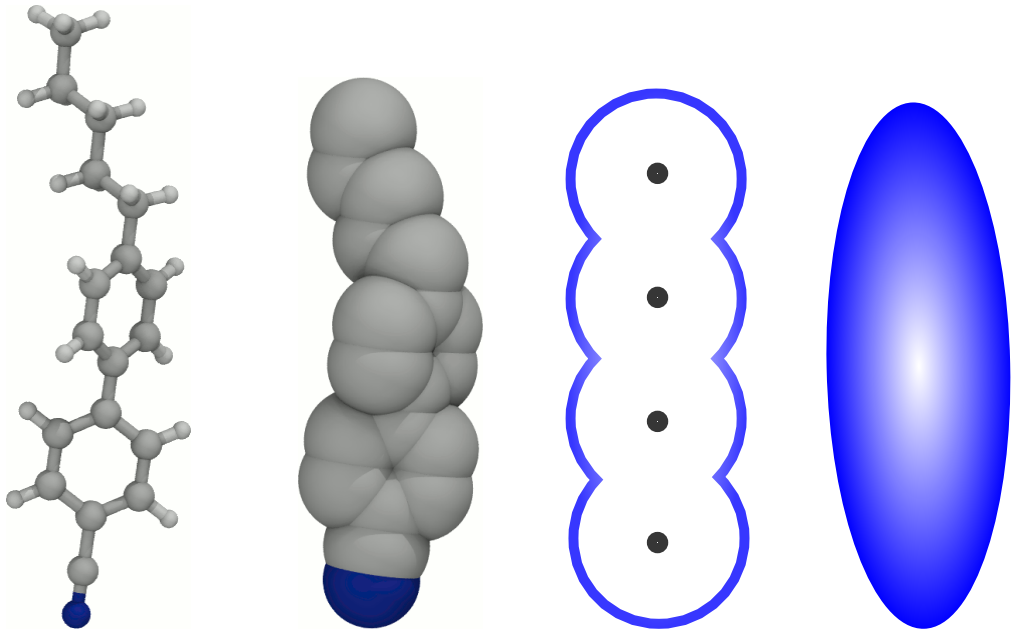

(a) Full atomistic (b) United atoms (c) 4 sites (d) Single object

Figure 5.1: The molecule of the nematic liquid crystal 5CB represented at different levels of description.

The sites are described by short-range repulsion potentials, while the long-range electrostatic interactions are added to the model by a distribution of point charges or multipole expansion [88]. A drawback of the site-site potential is that the computation cost increases rapidly with the number of sites used, and often an adequate representation requires many of them [88].

A coarser level of description can be achieved by representing a whole molecule with a single rigid body. In this approach, the pairwise interactions between particles are chosen to represent the symmetries found in the original molecule, if present. A comparison between different levels of coarse graining is shown in Figure 5.1.

In this thesis work we aim to describe systems of active particles dispersed in a liquid crystal medium. To reach this goal, we will represent every molecule in the system as a single anisotropic object, whose position is described by the three coordinates $\mathbf{r}^i = \{r^i_x, r^i_y, r^i_z\}$ for its centre of mass, with an additional set of coordinates for its orientation [89]. The orientation can be expressed in several different ways, for example, in the previous chapters we used Euler angles $\Omega = \{\alpha, \beta, \gamma\}$ for this task. Unfortunately, the equations of motions written in the Euler formalism have a inconvenient spurious singularity when $\beta = 0$ [89]. This problem can be avoided by using

quaternions to represent the orientation of particles.

Therefore, the generalized set of coordinates for each particle i will be:

- The centre of mass $\mathbf{r}^i$ to represent the position of the particle in the Cartesian space.
- The quaternion $\mathbf{q}^i$ to describe the orientational degrees of freedom.
- The conjugate momenta $\mathbf{p}$ and $\mathbf{Q}$ for the position and orientation, respectively.

In this way, the micro state of a system composed of N particles (is configuration) is completely specified by $\Gamma = \{\mathbf{r}^1, \mathbf{q}^1, \mathbf{p}^1, \mathbf{Q}^1, \cdots, \mathbf{r}^N, \mathbf{q}^N, \mathbf{p}^N, \mathbf{Q}^N\}$.

It is beyond the scope of this thesis to show how quaternions generate the rotation group. Here, we will only show how to use quaternions to represent the orientation and how to convert the Newtonian torques and angular velocities in and out of this representation. For the reader interested in a more detailed review, we refer the book of Altman [93].

Quaternions are elements of four dimensional space $\mathbf{q} = \{q_0, q_1, q_2, q_4\}$ with the operations of addition $\mathbf{q} + \mathbf{q}'$, multiplication by constant $a_0\mathbf{q}$ and dot product $\mathbf{q} \cdot \mathbf{q}'$ defined as normal vectors, a norm defined as $|\mathbf{q}| = \sum_i {q_i}^2$, plus an outer product $\mathbf{q}'' = \mathbf{q}'\mathbf{q}$ defined as [94]

$$\mathbf{q}'' = \mathbf{S}(\mathbf{q}')\mathbf{q} = \begin{bmatrix} q'_0 & -q'_1 & -q'_2 & -q'_3 \\ q'_1 & q'_0 & -q'_3 & q'_2 \\ q'_2 & q'_3 & q'_0 & -q'_1 \\ q'_3 & -q'_2 & q'_1 & q'_0 \end{bmatrix} \begin{bmatrix} q_0 \\ q_1 \\ q_2 \\ q_3 \end{bmatrix}, \tag{5.9}$$

the matrix in the product definition can be inverted to give the quaternion inversion rule: $\mathbf{q}^{-1} = \{q_0, -q_1, -q_2, -q_3\}/|\mathbf{q}|$. Notice that if the quaternion is of norm one, we also have $\mathbf{S}^{-1}(\mathbf{q}) = \mathbf{S}^T(\mathbf{q})$.

We can represent any Cartesian vector $\mathbf{u} = \{u_1, u_2, u_4\}$ as a quaternion by the rule $\mathbf{u}^{(4)} = \{0, u_1, u_2, u_3\}$, where the superscript (4) indicates the quaternion representation of a vector. In the quaternion representation, any rotation of a vector $\mathbf{u}^{(4)}$ around an axis indicated by the unit vector $\hat{\mathbf{n}}$ by an angle α can be obtained by

$$\mathbf{u}_r^{(4)} = \mathbf{q}^{-1}(\alpha, \hat{\mathbf{n}})\mathbf{u}^{(4)}\mathbf{q}(\alpha, \hat{\mathbf{n}}), \tag{5.10}$$

where $\mathbf{u}_r^{(4)}$ is the rotated quaternion and $\mathbf{q}(\alpha,\hat{\mathbf{n}})$ is the rotation quaternion, whose components are $q_0 = \cos(\alpha/2)$, $q_1 = n_x \sin(\alpha/2)$, $q_2 = n_y \sin(\alpha/2)$ and $q_3 = n_z \sin(\alpha/2)$. The double quaternion multiplication in Eq. (5.10) can be summarized by [94]

$$\mathbf{u}_r^{(4)} = \begin{bmatrix} 1 & 0 & 0 & 0 \\ 0 & 1-{q_2}^2-{q_3}^2 & 2q_1q_2+2q_0q_3 & 2q_1q_3-2q_0q_2 \\ 0 & 2q_1q_2-2q_0q_3 & 1-{q_1}^2{q_3}^2 & 2q_3q_2+2q_0q_1 \\ 0 & 2q_1q_3+2q_0q_2 & 2q_2q_3-2q_0q_1 & 1-{q_2}^2-{q_1}^2 \end{bmatrix} \begin{bmatrix} 0 \\ u_1 \\ u_2 \\ u_3 \end{bmatrix} = \mathbf{R}^{(4)}(\mathbf{q})\mathbf{u}^{(4)}, \tag{5.11}$$

where we dropped the dependence on $(\alpha,\hat{\mathbf{n}})$, since any quaternion which satisfies $|\mathbf{q}| = 1$ can be mapped into a rotation matrix.

Due to the block nature of the matrix $\mathbf{R}^{(4)}(\mathbf{q})$, we can write an equivalent rotation matrix for a Cartesian vector as

$$\mathbf{R}(\mathbf{q}) = \begin{bmatrix} 1-{q_2}^2-{q_3}^2 & 2q_1q_2+2q_0q_3 & 2q_1q_3-2q_0q_2 \\ 2q_1q_2-2q_0q_3 & 1-{q_1}^2{q_3}^2 & 2q_3q_2+2q_0q_1 \\ 2q_1q_3+2q_0q_2 & 2q_2q_3-2q_0q_1 & 1-{q_2}^2-{q_1}^2 \end{bmatrix}, \tag{5.12}$$

again with $|\mathbf{q}| = 1$.

With the relations (5.10) and (5.12) we can rotate any vector $\mathbf{r}_{\mathrm{LAB}} = \{r_x^{LAB}, r_y^{LAb}, r_z^{LAb}\}$ from the laboratory system of reference (i.e. LAB frame) , where the measurements are performed, to the molecular fixed frame (i.e. MOL frame) $\mathbf{r}_{\mathrm{MOL}}$:

$$\mathbf{r}_{\mathrm{MOL}} = \mathbf{R}(\mathbf{q})\mathbf{r}_{\mathrm{LAB}}, \tag{5.13}$$

therefore, with the knowledge of the particle quaternion $\mathbf{q}$, we can determine any orientation-dependent quantity.

Now we need to specify how to obtain other mechanical quantities in terms of quaternions, and how they are related to their Cartesian analogues. By defining the

extended inertia tensor $\mathbf{I}^{(4)}_{\mathrm{MOL}}$ in the molecular frame as

$$\mathbf{I}^{(4)}_{\mathrm{MOL}} = \begin{bmatrix} 1 & 0 & 0 & 0 \\ 0 & I_{xx} & 0 & 0 \\ 0 & 0 & I_{yy} & 0 \\ 0 & 0 & 0 & I_{zz} \end{bmatrix}, \tag{5.14}$$

where I_{ii} are the usual inertia tensor components in the molecular frame, we can write the rotational kinetic energy of particle i as [95]

$$K_{rot}(\mathbf{q}^i, \mathbf{Q}^i) = \frac{1}{8}\mathbf{Q}^{i\,T}\mathbf{S}(\mathbf{q})\mathbf{I}^{(4)\,-1}_{\mathrm{MOL}}\mathbf{S}^T(\mathbf{q})\mathbf{Q}^i, \tag{5.15}$$

therefore the Hamiltonian of the system can be written as

$$H(\Gamma) = \sum_i \left(\frac{1}{8}\mathbf{Q}^{i\,T}\mathbf{S}(\mathbf{q})\mathbf{I}^{(4)\,i\;\;-1}_{\mathrm{MOL}}\mathbf{S}^T(\mathbf{q})\mathbf{Q}^i + \sum_j \frac{p^i_j p^i_j}{2m^i} \right) + U(\mathbf{r}^1, \mathbf{q}^1 \cdots, \mathbf{r}^N, \mathbf{q}^N), \tag{5.16}$$

where m^i is the ith particle mass. The Eq. (5.16) can be substituted in Eq. (5.7) to give the equations of motion for all the generalized coordinates and their conjugate moments.

The conjugate moments and torques can be easily related to their Cartesian counterparts. For instance, the angular velocities $\boldsymbol{\omega}^{(4)\,i}_{\mathrm{MOL}} = \{0, \omega^{\mathrm{MOL}}_x, \omega^{\mathrm{MOL}}_y, \omega^{\mathrm{MOL}}_z\}$ in the molecular frame can be calculated by [95]

$$\boldsymbol{\omega}^{(4)\,i}_{\mathrm{MOL}} = 2\mathbf{S}^T(\mathbf{q}^i)\dot{\mathbf{q}}^i, \tag{5.17}$$

where the dot indicates the time derivative. The Cartesian torques $\boldsymbol{\tau}^{(4)\,i}_{\mathrm{LAB}} = \{0, \tau_x, \tau_y, \tau_Z\}$ in the laboratory frame, can be obtained from a quaternion-dependent potential $U(\mathbf{r}^1, \mathbf{q}^1 \cdots, \mathbf{r}^N, \mathbf{q}^N)$ by using the relation [95]:

$$\boldsymbol{\tau}^{(4)\,i}_{\mathrm{LAB}} = -\frac{1}{2}\mathbf{S}^T(\mathbf{q}^i)\nabla_{q^i} U(\mathbf{r}^1, \mathbf{q}^1 \cdots, \mathbf{r}^N, \mathbf{q}^N), \tag{5.18}$$

where $\nabla_{q^i} = \{\partial_{q^i_0}, \partial_{q^i_1}, \partial_{q^i_2}, \partial_{q^i_3}\}$ is the quaternion gradient. The forces can be obtained

from the potential gradient expression

$$\mathbf{f}^i = -\nabla_{r^i} U(\mathbf{r}^1, \mathbf{q}^1 \cdots, \mathbf{r}^N, \mathbf{q}^N), \tag{5.19}$$

being $\nabla_{r^i} = \{\partial_{r_x^i}, \partial_{r_y^i}, \partial_{r_z^i}\}$ the translational gradient.

5.3 Interaction with an external reservoir

In most active system, the active propellers are suspended in some sort solvent, that can work as a thermal bath. In these situations, the time evolution of Γ_t requires to model each element of the thermodynamic system together with the elements of the thermal reservoir, which is virtually impossible.

To avoid this problem, we need to decouple the degrees of freedom due to the thermal reservoir. One approach is to abandon Eq. (5.3) and focus on generating an equilibrium distribution of microscopic states, which can averaged to obtain the desired properties. One of the most used method derived from this approach is the Nose-Hoover thermostat [87, 88]. However, in active systems there are additional problems hindering its use. Since the active particles are constantly introducing energy into the system due to the active force, the system is intrinsically out of equilibrium, and we cannot be sure that the distribution of micro states follows Boltzmann statistics. Moreover, the temperature of active systems is more complicated to define, since it is not easy to separate the velocity due to thermal motions from the coherent motion due to active forces.

In order to thermalize these systems, it is necessary to use procedures acting on each particle individually. Such procedures are called local thermostats. To this aim, the work presented here will be based on the Langevin thermostat. This thermostat was originally developed to model the movements of particles in solutions, but it was shown that at long times it actually generates micro states with a Boltzmann distribution. Therefore, it can be used to thermalize pure systems as well [90].

Langevin thermostat

In the systems of active particles cited previously, all samples are composed of dissolved particles which are much bigger than solvent particles. Due to their reduced size, the time scale of solvent particles can be one to two orders of magnitude faster than the dissolved ones. If we write and solve the Hamiltonian for the whole system, most part of the computing time will be spent on calculating trajectories that, in principle, we are not interested in.

To avoid these problems, instead of describing each degree of freedom of the thermal reservoir, we will take into account the average effect that it has on the particles of the system of interest. Following the Mori-Zwanzig projection operator approach, it is possible to remove the degrees of freedom of the bath and include their effect on the guest particles by adding a frictional and a random term in their equations of motion [90]. If we assume that the thermal bath responds to the particles movement instantaneously, we can show that a particle with the Hamiltonian described in equation (5.16) will obey the following Langevin type equations of motion:

$$\begin{aligned} \dot{\mathbf{p}}^i(t) &= \mathbf{f}^i(t) - \gamma \mathbf{p}^i(t) + \boldsymbol{\sigma}_i^t(t), \\ \dot{\mathbf{r}}^i(t) &= \mathbf{p}^i(t) \end{aligned} \tag{5.20}$$

where γ is the friction parameter modulating the interaction between the system and the thermal-dissipative medium, and $\boldsymbol{\sigma}_i^t(t) = \{\sigma_{i,x}^t(t), \sigma_{i,y}^t(t), \sigma_{i,z}^t(t)\}$ are three dimensional vectors, where each element is a Gaussian white noise with correlation

$$\langle \sigma_{\alpha,i}^t(t) \sigma_{\beta,j}^t(t') \rangle = \sqrt{2\gamma m k_B T} \delta(t-t') \delta_{i,j} \delta_{\alpha,\beta}, \tag{5.21}$$

being k_B is the Boltzmann constant and T the bath temperature. The (5.21) ensures that the fluctuation dissipation theorem is respected.

The only free parameter in this thermostat is the friction term γ. For spherical particles, γ can be related to the friction term η present in the Perrin-Einstein equation. The use of a friction term gives the right diffusive behaviour to the simulated particles. In this case, even though any simulation will show different molecular trajectories due to the random term, any trajectory can be assumed to be a particular

realization from the space of all possible trajectories.

Even though the Langevin thermostat was formally developed for particles dissolved in a large system acting as a thermal bath, it can still be used for particles belonging to a pure systems. In this situation, the solution of the Langevin equations of motion ensures that the succession of micro states in the trajectory obeys a Boltzmann distribution. As a consequence, the resulting trajectory can be used to perform the ensemble averages in Eq. (5.8). This result holds for any reasonable value of γ.

This formalism can be extended to rigid anisotropic particles by adding a combination of random and a dissipative torques representing the interaction with the bath. The equations of motion expressing the orientation are then given by

$$\begin{aligned} \dot{\mathbf{L}}^i_{\mathrm{LAB}}(t) &= \boldsymbol{\tau}^i_{\mathrm{LAB}}(t) - \gamma_r \mathbf{I}^i_{\mathrm{MOL}} \boldsymbol{\omega}^i_{LAB}(t) + \boldsymbol{\sigma}^r_i(t), \\ \dot{\mathbf{q}}^i(t) &= \frac{1}{2}\mathbf{S}\left(\boldsymbol{\omega}^{(4)\,i}_{\mathrm{LAB}}(t)\right)\mathbf{q}^i(t), \end{aligned} \tag{5.22}$$

where $\mathbf{L}^i_{\mathrm{LAB}}(t)$, $\boldsymbol{\tau}^i_{\mathrm{LAB}}(t)$ and $\boldsymbol{\omega}^{(4)\,i}_{\mathrm{LAB}}(t) = \{0, \omega^i_x, \omega^i_y, \omega^i_z\}$ are the ith particle angular momentum, torque and angular velocity in the LAB frame, γ_r is another friction constant and $\boldsymbol{\sigma}^r_i(t) = \{\sigma^r_{i,x}(t), \sigma^r_{i,y}(t), \sigma^r_{i,z}(t)\}$ is another Gaussian white-noise which correlations given by

$$\langle \sigma^r_{\alpha,i}(t)\sigma^r_{\beta,j}(t')\rangle = \sqrt{2\gamma I^{mol}_{ij} k_B T}\,\delta(t-t')\delta_{ij}. \tag{5.23}$$

where I^{mol}_{ij} are the components of the inertia tensor in the molecular frame.

5.3.1 Interaction Potential

In this work we approximate all the molecules in a given system with single particles having the properties of a non-spherical rigid body. The crucial part of this approximation is to derive an interaction potential that reproduces, at least approximately, the physics of a real system or of a system simulate with atomistic detail. For instance, an anisotropic molecule will be represented by an ellipsoid, and the potential acting between ellipsoidal particles needs to display different interaction energies when the particles are aligned in different orientations. An example of the relative orientation of ellipsoidal particles and the corresponding nomenclature of

each configuration is given in Figure 5.2.

A successful example of such potential is that developed by Gay and Berne [96] for uniaxial ellipsoids and generalized by to arbitrary particles by Berardi et. al. [97]. The uniaxial Gay-Berne potential considers the interacting particles as revolution ellipsoids with breadth and length σ_s and σ_e. The potential is pairwise, which means that the total energy for a system of N particles will be:

$$U_{\mathrm{GB}}(\mathbf{r}^1,\mathbf{q}^1\cdots,\mathbf{r}^N,\mathbf{q}^N)=\sum_{i=1}^{N}\sum_{j>i}^{N}U_{\mathrm{GB}}(\mathbf{r}^i,\mathbf{q}^i,\mathbf{r}^j,\mathbf{q}^j), \tag{5.24}$$

where $\mathbf{r}^i$ is the centre of mass of the ith particle and $\mathbf{q}^i$ the ith particle quaternion.

More specifically, the Gay-Berne potential energy of two ellipsoids with symmetry axis aligned along the unit vectors $\hat{\mathbf{u}}^i(\mathbf{q}^i)$ and $\hat{\mathbf{u}}^j(\mathbf{q}^j)$ with the inter-molecular vector $\mathbf{r}^{ij}=\mathbf{r}^i-\mathbf{r}^j$ connecting their centre of mass will be given by [98]

$$\begin{aligned}U_{\mathrm{GB}}(\mathbf{r}^i,\mathbf{q}^i,\mathbf{r}^j,\mathbf{q}^j)&\equiv U_{\mathrm{GB}}(\hat{\mathbf{u}}^i,\hat{\mathbf{u}}^j,\mathbf{r}^{ij})\\&=4\epsilon(\hat{\mathbf{u}}^i,\hat{\mathbf{u}}^j,\hat{\mathbf{r}}^{ij})\left\{\left(\frac{\sigma_s}{r^{ij}-\sigma(\hat{\mathbf{u}}^i,\hat{\mathbf{u}}^j,\hat{\mathbf{r}}^{ij})+\sigma_s}\right)^{12}-\left(\frac{\sigma_s}{r^{ij}-\sigma(\hat{\mathbf{u}}^i,\hat{\mathbf{u}}^j,\hat{\mathbf{r}}^{ij})+\sigma_s}\right)^{6}\right\}\end{aligned} \tag{5.25}$$

where $\sigma(\hat{\mathbf{u}}^i,\hat{\mathbf{u}}^j,\hat{\mathbf{r}}^{ij})$ is approximately the contact distance between the ellipsoids i and j, which is expressed as

$$\sigma(\hat{\mathbf{u}}^i,\hat{\mathbf{u}}^j,\hat{\mathbf{r}}^{ij}) \quad = \quad \sigma_s\left\{1-\frac{\chi}{2}\left[\frac{(\hat{\mathbf{u}}^i\cdot\hat{\mathbf{r}}^{ij}+\hat{\mathbf{u}}^j\cdot\hat{\mathbf{r}}^{ij})^2}{1+\chi(\hat{\mathbf{u}}^i\cdot\hat{\mathbf{u}}^j)}+\frac{(\hat{\mathbf{u}}^i\cdot\hat{\mathbf{r}}^{ij}-\hat{\mathbf{u}}^j\cdot\hat{\mathbf{r}}^{ij})^2}{1-\chi(\hat{\mathbf{u}}^i\cdot\hat{\mathbf{u}}^j)}\right]\right\}^{-1/2}$$

with

$$\chi=\frac{\kappa^2-1}{\kappa^2+1}$$

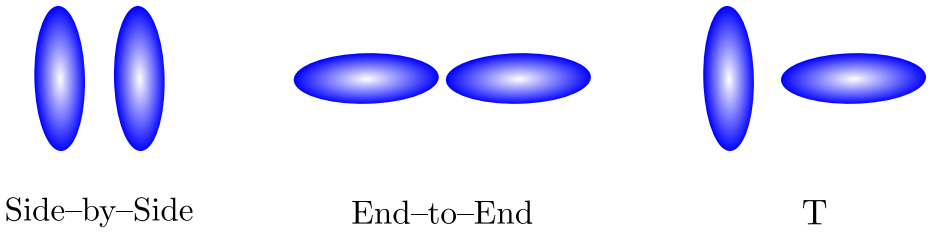

Figure 5.2: Representation of the particle alignment side–by–side, end–to–end and T.

being $\kappa \equiv \sigma_e/\sigma_s$ the shape anisotropy.

The term $\epsilon(\hat{\mathbf{u}}^i, \hat{\mathbf{u}}^j, \hat{\mathbf{r}}_{ij})$ is a weighting factor for the energy, based on the relative orientation of the particles, expressed as

$$\epsilon(\hat{\mathbf{u}}^i, \hat{\mathbf{u}}^j, \mathbf{r}^{ij}) = \epsilon_0 \epsilon'^{\mu}(\hat{\mathbf{u}}^i, \hat{\mathbf{u}}^j, \mathbf{r}^{ij}) \epsilon^{\nu}(\hat{\mathbf{u}}^i, \hat{\mathbf{u}}^j) \tag{5.26}$$

where μ and ν are parameters that can be used to tune the shape of the potential well in a way appropriate to the chemical nature of the particles, with

$$\epsilon(\hat{\mathbf{u}}^i, \hat{\mathbf{u}}^j) = \left[1 - \chi^2 (\hat{\mathbf{u}}^i \cdot \hat{\mathbf{u}}^j)^2\right]^{-1/2} \tag{5.27}$$

and $\epsilon'^{\mu}(\hat{\mathbf{u}}_1, \hat{\mathbf{u}}^j, \mathbf{r}^{ij})$ given by

$$\epsilon'(\hat{\mathbf{u}}^i, \hat{\mathbf{u}}^j, \hat{\mathbf{r}}^{ij}) = \left\{1 - \frac{\chi'}{2}\left[\frac{(\hat{\mathbf{u}}^i \cdot \hat{\mathbf{r}}^{ij} + \hat{\mathbf{u}}^j \cdot \hat{\mathbf{r}}^{ij})^2}{1 + \chi'(\hat{\mathbf{u}}^i \cdot \hat{\mathbf{u}}^j)} + \frac{(\hat{\mathbf{u}}^i \cdot \hat{\mathbf{r}}^{ij} - \hat{\mathbf{u}}^j \cdot \hat{\mathbf{r}}^{ij})^2}{1 - \chi'(\hat{\mathbf{u}}^i \cdot \hat{\mathbf{u}}^j)}\right]\right\}^{-1/2} \tag{5.28}$$

with

$$\chi' = \frac{\kappa^{1/\mu} - 1}{\kappa^{1/\mu} + 1}$$

where $\kappa' = \epsilon_s/\epsilon_e$ is the interaction anisotropy. The parameters ϵ_s and ϵ_e correspond to the depth of the potential wells when the particles are aligned side–by–side and end–to–end, respectively.

Finally, if the symmetry axis are aligned along with z axis in the molecular frame (i.e. $\hat{\mathbf{u}}^i_{\text{mol}} = \{0, 0, 1\}$), the components of $\hat{\mathbf{u}}^i$ in the LAB frame can be computed by the expression:

$$\hat{\mathbf{u}}^i = R^T(\mathbf{q}^i)\hat{\mathbf{u}}^i_{\text{mol}} = \begin{bmatrix} 2(q^i_1 q^i_3 + q^i_2 q^i_0) \\ 2(q^i_2 q^i_3 - q^i_0 q^i_1) \\ {q^i_0}^2 - {q^i_1}^2 - {q^i_2}^2 + {q^i_3}^2 \end{bmatrix}. \tag{5.29}$$

The phase diagram of systems of particles described by the Gay-Berne potential has been studied in the literature for a few parametrizations. In particular, the phase diagram of a system of particles interacting only via a Gay-Berne potential with parameters $\{\mu = 1, \nu = 3, \kappa = 3, \kappa' = 5\}$ has been show to display the isotropic, nematic,

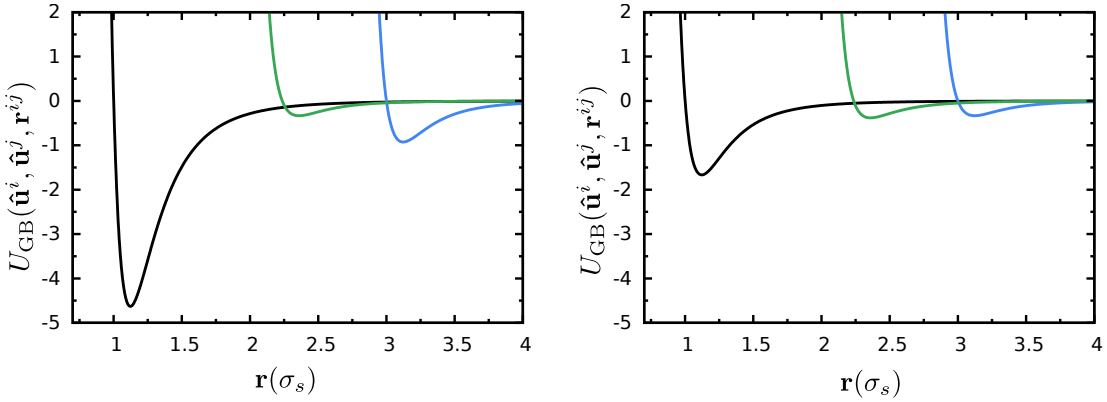

(a) $\mu = 1$ and $\nu = 3$ **(b)** $\mu = 2$ and $\nu = 1$

Figure 5.3: Gay-Berne potential energy curves calculated for the geometries: side–by–side (black), end–to–end (blue) and T (green). For both panels, $\kappa = 3$, $\kappa' = 5$ and the distance is expressed in units of σ_s.

and smectic phases typical of liquid crystals [98]. Conversely, the set of parameters $\{\kappa = 3, \kappa' = 5, \mu = 2, \nu = 1\}$ generates isotropic, nematic, smectic A, smectic B and crystal phases [99]. An example of Gay-Berne potentials energy curves calculated for different geometries and sets of parameters, is given in Figure 5.3.

Calculation of forces and torques

In this section we will carry out in detail the calculations of forces and torques involved in the uniaxial Gay-Berne potential. Following Luckhurst et. al. [99], we can simplify the algebraic manipulations defining:

$$R = \frac{r^{ij} - \sigma(\hat{\mathbf{u}}^i, \hat{\mathbf{u}}^j, \hat{\mathbf{r}}^{ij}) + \sigma_s}{\sigma_s} \tag{5.30}$$

and

$$g(\chi) = 1 - \frac{\chi}{2r^{ij\,2}} \left[\frac{(\hat{\mathbf{u}}^i \cdot \mathbf{r}^{ij} + \hat{\mathbf{u}}^j \cdot \mathbf{r}^{ij})^2}{1 + \chi(\hat{\mathbf{u}}^i \cdot \hat{\mathbf{u}}^j)} + \frac{(\hat{\mathbf{u}}^i \cdot \mathbf{r}^{ij} - \hat{\mathbf{u}}^j \cdot \mathbf{r}^{ij})^2}{1 - \chi(\hat{\mathbf{u}}^i \cdot \hat{\mathbf{u}}^j)} \right]. \tag{5.31}$$

The function $g(\chi)$ is related to $\sigma(\hat{\mathbf{u}}^i, \hat{\mathbf{u}}^j, \hat{\mathbf{r}}^{ij})$ and $\epsilon'(\hat{\mathbf{u}}^i, \hat{\mathbf{u}}^j, \hat{\mathbf{r}}^{ij})$ by the relations:

$$g(\chi)^{-1/2} = \frac{\sigma(\hat{\mathbf{u}}^i, \hat{\mathbf{u}}^j, \hat{\mathbf{r}}^{ij})}{\sigma_s},$$
$$g(\chi') = \epsilon'(\hat{\mathbf{u}}^i, \hat{\mathbf{u}}^j, \hat{\mathbf{r}}^{ij}). \tag{5.32}$$

Since the Gay-Berne potential is pairwise, the total force and torque acting on each particle can be obtained calculating the pairwise components separately and summing them together:

$$\begin{aligned}\mathbf{f}^i &= \sum_j -\nabla_{r^i} U_{\mathrm{GB}}(\hat{\mathbf{u}}^i, \hat{\mathbf{u}}^j, \mathbf{r}^{ij}) = \sum_j \mathbf{f}^{ij} \\ \boldsymbol{\tau}^{(4)\,i}_{\mathrm{LAB}} &= \sum_j -\nabla_{q^i} U_{\mathrm{GB}}(\hat{\mathbf{u}}^i, \hat{\mathbf{u}}^j, \mathbf{r}^{ij}) = \sum_j \boldsymbol{\tau}^{(4)\,ij}_{\mathrm{LAB}}.\end{aligned} \tag{5.33}$$

The x component of the force in the ith particle due to the interaction with the jth particle ($\mathbf{f}^{ij}$) can be obtained by

$$\begin{aligned}f_x^{ij} = -\frac{\partial}{\partial r_x^i} U_{\mathrm{GB}}(\hat{\mathbf{u}}^i, \hat{\mathbf{u}}^j, \mathbf{r}^{ij}) = -\epsilon_0 \Bigg\{ &\epsilon(\hat{\mathbf{u}}^i, \hat{\mathbf{u}}^j) g^{\mu}(\chi') \left[6R^{-7} - 12R^{-13}\right] \left(\frac{\partial}{\partial r_x^i} R\right) \\ &+ (R^{-12} - R^{-6}) \mu g^{\mu-1}(\chi') \frac{\partial}{\partial r_x^i} g(\chi) \Bigg\}\end{aligned} \tag{5.34}$$

where

$$\frac{\partial}{\partial r_x^i} R = \frac{\partial}{\partial r_x^i} r^{ij} + \frac{\sigma_s}{2} g^{-3/2}(\chi) \frac{\partial}{\partial r_x^i} r^{ij}, \tag{5.35}$$

with

$$\frac{\partial}{\partial r_x^i} r^{ij} = \frac{r_x^{ij}}{r^{ij}} \tag{5.36}$$

and

$$\begin{aligned}\frac{\partial}{\partial r_x^i} g(\chi) = -\frac{\chi}{{r^{ij}}^2} \Bigg[&\frac{(\hat{\mathbf{u}}^i \cdot \hat{\mathbf{u}}^j + \hat{\mathbf{u}}^j \cdot \hat{\mathbf{r}}^{ij})}{1 + \chi(\hat{\mathbf{u}}^i \cdot \hat{\mathbf{u}}^j)} \left\{ \frac{\partial}{\partial r_x^i} (\mathbf{r}^{ij} \cdot \hat{\mathbf{u}}^i) + \frac{\partial}{\partial r_x^i} (\mathbf{r}^{ij} \cdot \hat{\mathbf{u}}^j) \right\} \\ &+ \frac{(\hat{\mathbf{u}}^i \cdot \hat{\mathbf{u}}^j - \hat{\mathbf{u}}^j \cdot \hat{\mathbf{r}}^{ij})}{1 - \chi(\hat{\mathbf{u}}^i \cdot \hat{\mathbf{u}}^j)} \left\{ \frac{\partial}{\partial r_x^i} (\mathbf{r}^{ij} \cdot \hat{\mathbf{u}}^i) - \frac{\partial}{\partial r_x^i} (\mathbf{r}^{ij} \cdot \hat{\mathbf{u}}^j) \right\} \Bigg] \\ &+ \frac{x\chi}{r^{ij}} \left[\frac{(\hat{\mathbf{u}}^i \cdot \hat{\mathbf{u}}^j + \hat{\mathbf{u}}^j \cdot \hat{\mathbf{r}}^{ij})^2}{1 + \chi(\hat{\mathbf{u}}^i \cdot \hat{\mathbf{u}}^j)} + \frac{(\hat{\mathbf{u}}^i \cdot \hat{\mathbf{u}}^j - \hat{\mathbf{u}}^j \cdot \hat{\mathbf{r}}^{ij})^2}{1 - \chi(\hat{\mathbf{u}}^i \cdot \hat{\mathbf{u}}^j)} \right]\end{aligned} \tag{5.37}$$

with

$$\frac{\partial}{\partial r_x^i} (\mathbf{r}^{ij} \cdot \hat{\mathbf{u}}^i) = \hat{\mathbf{u}}_x^i. \tag{5.38}$$

Due to the symmetries in the set of equations, the calculation of the other compo-

nents of the force can be performed substituting x by y or z in all vectors.

We will proceed in a similar manner to compute the torques. The quaternion gradient of the Gay-Berne potential is given by

$$\frac{\partial}{\partial \mathbf{q}_1^i} U_{\mathrm{GB}}(\hat{\mathbf{u}}^i, \hat{\mathbf{u}}^j, \mathbf{r}^{ij}) = \sum_l \frac{\partial}{\partial \hat{u}_l^i} U_{\mathrm{GB}}(\hat{\mathbf{u}}^i, \hat{\mathbf{u}}^j, \mathbf{r}^{ij}) \frac{\partial}{\partial q_k^i} \hat{u}_k^i, \tag{5.39}$$

which can be organized in the matrix form

$$\begin{bmatrix} \frac{\partial}{\partial q_1^i} U_{\mathrm{GB}}(\hat{\mathbf{u}}^i, \hat{\mathbf{u}}^j, \mathbf{r}^{ij}) \\ \frac{\partial}{\partial q_2^i} U_{\mathrm{GB}}(\hat{\mathbf{u}}^i, \hat{\mathbf{u}}^j, \mathbf{r}^{ij}) \\ \frac{\partial}{\partial q_3^i} U_{\mathrm{GB}}(\hat{\mathbf{u}}^i, \hat{\mathbf{u}}^j, \mathbf{r}^{ij}) \\ \frac{\partial}{\partial q_4^i} U_{\mathrm{GB}}(\hat{\mathbf{u}}^i, \hat{\mathbf{u}}^j, \mathbf{r}^{ij}) \end{bmatrix} = \begin{bmatrix} q_2^i & -q_1^i & q_0^i \\ q_3^i & -q_0^i & -q_1^i \\ q_0^i & q_3^i & -q_2^i \\ q_1^i & q_2^i & q_3^i \end{bmatrix} \begin{bmatrix} \frac{\partial}{\partial \hat{u}_x^i} U_{\mathrm{GB}}(\hat{\mathbf{u}}^i, \hat{\mathbf{u}}^j, \mathbf{r}^{ij}) \\ \frac{\partial}{\partial \hat{u}_y^i} U_{\mathrm{GB}}(\hat{\mathbf{u}}^i, \hat{\mathbf{u}}^j, \mathbf{r}^{ij}) \\ \frac{\partial}{\partial \hat{u}_z^i} U_{\mathrm{GB}}(\hat{\mathbf{u}}^i, \hat{\mathbf{u}}^j, \mathbf{r}^{ij}) \end{bmatrix}, \tag{5.40}$$

where we substituted the values of $\hat{u}_i$ to evaluate the first matrix in the r.h.s.

To integrate the equations of motion (5.22), we need the torques expressed in the Cartesian frame. If we substitute Eq. (5.40) in Eq. (5.18) and perform the matrix operation, we obtain

$$\begin{bmatrix} 0 \\ \tau_{\mathrm{LAB},x}^{ij} \\ \tau_{\mathrm{LAB},y}^{ij} \\ \tau_{\mathrm{LAB},z}^{ij} \end{bmatrix} = - \begin{bmatrix} 2q_0^i q_2^i + 2q_1^i q_3^i & 2q_2^i q_3^i - 2q_0^i q_1^i & 1 - 2q_1^{i\,2} - 2q_2^{i\,2} \\ 0 & 2q_1^{i\,2} + 2q_2^{i\,2} - 1 & 2q_2^i q_3^i - 2q_0^i q_1^i \\ 1 - 2q_1^{i\,2} - 2q_2^{i\,2} & 0 & -2q_0^i q_2^i - 2q_1^i q_3^i \\ 2q_0^i q_1^i - 2q_2^i q_3^i & 2q_0^i q_2^i + 2q_1^i q_3^i & 0 \end{bmatrix} \begin{bmatrix} \frac{\partial U_{\mathrm{GB}}(\hat{\mathbf{u}}^i, \hat{\mathbf{u}}^j, \mathbf{r}^{ij})}{\partial \hat{u}_x^i} \\ \frac{\partial U_{\mathrm{GB}}(\hat{\mathbf{u}}^i, \hat{\mathbf{u}}^j, \mathbf{r}^{ij})}{\partial \hat{u}_y^i} \\ \frac{\partial U_{\mathrm{GB}}(\hat{\mathbf{u}}^i, \hat{\mathbf{u}}^j, \mathbf{r}^{ij})}{\partial \hat{u}_z^i}. \end{bmatrix}. \tag{5.41}$$

In the previous equations we can recognize the elements of the first matrix on the r.h.s as the components of the unit vector $\hat{\mathbf{u}}$. Therefore, this equation can be simplified to

$$\boldsymbol{\tau}_{\mathrm{LAB}}^{ij} = \hat{\mathbf{u}}^{\mathbf{i}} \times \frac{\partial}{\partial \hat{\mathbf{u}}^{\mathbf{i}}} U_{\mathrm{GB}}(\hat{\mathbf{u}}^i, \hat{\mathbf{u}}^j, \mathbf{r}^{ij}). \tag{5.42}$$

The derivatives of the Gay-Berne potential relative to the orientation unit vector

components $\hat{u}_i$ are given by

$$\frac{\partial}{\partial \hat{u}_x^i} U_{\mathrm{GB}}(\hat{\mathbf{u}}^i, \hat{\mathbf{u}}^j, \mathbf{r}^{ij}) = (R^{-12} - R^{-6}) \frac{\partial}{\partial \hat{u}_x^i} \epsilon(\hat{\mathbf{u}}^i, \hat{\mathbf{u}}^j, \hat{\mathbf{r}}^{ij}) + \epsilon(\hat{\mathbf{u}}^i, \hat{\mathbf{u}}^j, \hat{\mathbf{r}}^{ij})(6R^{-7} - 12R^{-13}) \frac{\partial}{\partial \hat{u}_x^i} R \tag{5.43}$$

where

$$\frac{\partial}{\partial \hat{u}_x^i} \epsilon(\hat{\mathbf{u}}^i, \hat{\mathbf{u}}^j, \hat{\mathbf{r}}^{ij}) = \epsilon_0 \epsilon^{\nu}(\hat{\mathbf{u}}^i, \hat{\mathbf{u}}^j) \mu g^{\mu-1}(\chi') \frac{\partial}{\partial \hat{u}_x^i} g(\chi') + \epsilon_0 g^{\mu}(\chi') \nu \epsilon^{\nu-1}(\hat{\mathbf{u}}^i, \hat{\mathbf{u}}^j) \frac{\partial}{\partial \hat{u}_x^i} \epsilon(\hat{\mathbf{u}}^i, \hat{\mathbf{u}}^j) \tag{5.44}$$

and

$$\frac{\partial}{\partial \hat{u}_x^i} \epsilon(\hat{\mathbf{u}}^i, \hat{\mathbf{u}}^j) = \chi^2 \epsilon^3(\hat{\mathbf{u}}^i, \hat{\mathbf{u}}^j) \hat{u}_x^j \tag{5.45}$$

being

$$\frac{\partial}{\partial \hat{u}_x^i} R = \frac{1}{2} \left[\frac{\sigma(\hat{\mathbf{u}}^i, \hat{\mathbf{u}}^j, \hat{\mathbf{r}}^{ij})}{\sigma_s} \right]^3 \frac{\partial}{\partial \hat{u}_x^i} g(\chi). \tag{5.46}$$

Finally, the derivative of $g(\chi)$ can obtained from the expression

$$\frac{\partial}{\partial \hat{u}_x^i} g(\chi) = -\frac{\chi}{2} \left[\hat{r}_x^{ij} \left\{ \frac{2(\hat{\mathbf{u}}^i \cdot \hat{\mathbf{r}}^{ij} + \hat{\mathbf{u}}^j \cdot \hat{\mathbf{r}}^{ij})}{1 + \chi(\hat{\mathbf{u}}^i \cdot \hat{\mathbf{u}}^j)} + \frac{2(\hat{\mathbf{u}}^i \cdot \hat{\mathbf{r}}^{ij} - \hat{\mathbf{u}}^j \cdot \hat{\mathbf{r}}^{ij})}{1 - \chi(\hat{\mathbf{u}}^i \cdot \hat{\mathbf{u}}^j)} \right\} + \chi \hat{u}_x^j \left\{ \frac{(\hat{\mathbf{u}}^i \cdot \hat{\mathbf{r}}^{ij} + \hat{\mathbf{u}}^j \cdot \hat{\mathbf{r}}^{ij})^2}{1 + \chi(\hat{\mathbf{u}}^i \cdot \hat{\mathbf{u}}^j)} + \frac{(\hat{\mathbf{u}}^i \cdot \hat{\mathbf{r}}^{ij} - \hat{\mathbf{u}}^j \cdot \hat{\mathbf{r}}^{ij})^2}{1 - \chi(\hat{\mathbf{u}}^i \cdot \hat{\mathbf{u}}^j)} \right\} \right] \tag{5.47}$$

5.3.2 Self Propelling Force

Besides the interaction potential and the thermal bath, the active particles are also endowed with a "molecular propeller" which can be switched on providing an external source of energy, whose effect will depends on the details of the active particles themselves. Here we are interested in self-propelled rods which are pushed by the active engine in the direction of the symmetry axis $\hat{\mathbf{u}}$. This can be accomplished by adding a velocity or an acceleration term to the usual list of interactions [76, 100].

In practice we have used propelling force $\mathbf{f_s}^i$, which acts on each active particle according to

$$\mathbf{f_s}^i = f_s \hat{\mathbf{u}}^i. \tag{5.48}$$

The only free parameter in this model is f_s, which modulates the strength of the propelling action and is assumed to be the same for all active particles.

5.4 Integration of the equations of motion

Now that all the internal and external agents acting in our sample are defined, we can finally integrate the equations of motion. Before developing the numerical algorithms, we need to rewrite some expressions in a more convenient way.

Knowing that $\dot{\mathbf{v}}^i = \dot{\mathbf{p}}^i / m^i$, we can write the equation of motion for the translation as

$$\begin{aligned} \dot{\mathbf{r}}^i(t) &= \mathbf{v}^i(t), \\ \dot{\mathbf{v}}^i(t) &= \frac{\mathbf{f}_G^i(t)}{m^i}, \end{aligned} \tag{5.49}$$

where $\mathbf{f}_G^i(t)$ is a generalized force with the form

$$\mathbf{f}_G^i(t) = \mathbf{f}^i(t) - \gamma m \mathbf{v}^i(t) + \boldsymbol{\sigma}_i^r(t) + f_s \hat{\mathbf{u}}^i. \tag{5.50}$$

We can perform a similar transformation with the terms in Eq. (5.22) to obtain

$$\begin{aligned} \dot{\mathbf{L}}_{LAB}^i(t) &= \boldsymbol{\tau}_G^i(t), \\ \dot{\mathbf{q}}^i(t) &= \mathbf{S}\left(\boldsymbol{\omega}_{LAB}^{(4)\,i}(t)\right)\mathbf{q}^i(t), \end{aligned} \tag{5.51}$$

where $\boldsymbol{\tau}_G^i(t)$ is a generalized torque given by

$$\boldsymbol{\tau}_G^i(t)^i = \boldsymbol{\tau}_{\mathrm{LAB}}^i(t) - \gamma \mathbf{I}_{\mathrm{MOL}}^i \boldsymbol{\omega}_{LAB}^i(t) + \boldsymbol{\sigma}_i^r(t), \tag{5.52}$$

where the first terms in r.h.s. are the Cartesian torques obtained using the transformation in Eq. (5.18).

The integration of the translational degrees of freedom can be performed in a straightforward way with the velocity Verlet algorithm [88], which comprises the following steps:

- Use the forces calculated at t to update the velocity of all particles by half a

timestep:

$$\mathbf{v}^i\left(t+\frac{1}{2}\Delta t\right)=\mathbf{v}^i(t)+\frac{1}{2}\Delta t\mathbf{f}^i(t) \tag{5.53}$$

- Use the new velocities $\mathbf{v}^i\left(t+\frac{1}{2}\Delta t\right)$ to update the position of all particles by a full timestep:

$$\mathbf{r}^i(t+\Delta t)=\mathbf{r}^i(t)+\Delta t\mathbf{v}^i\left(t+\frac{1}{2}\Delta t\right) \tag{5.54}$$

- Use the new positions $\mathbf{r}^i(t+\Delta t)$ to calculate the forces $\mathbf{f}^i(t+\Delta t)$ and to update the velocities for the last half timestep:

$$\mathbf{v}^i(t+\Delta t)=\mathbf{v}^i\left(t+\frac{1}{2}\Delta t\right)+\frac{1}{2}\Delta t\mathbf{f}^i(t+\Delta t) \tag{5.55}$$

In the calculation of the forces, the only point that needs more attention is the computation of the random noise $\boldsymbol{\sigma}_i^r(t)$. Even though it was said that the random noise needs to be Gaussian, Duwheg and Paul showed that a uniform distribution can be used with little loss of accuracy [101]. Therefore, the components of each vector can be computed as

$$\sigma_{i,j}^t=\sqrt{2\gamma mk_BT}\delta,$$

where δ is a uniform distribution with range [-0.5,0.5].

The rotational degrees of freedom are integrated with a similar version of the velocity Verlet, but the quaternions are updated with the Richardson method [73] to reduce the error. To proceed this way, we are going to estimate $\mathbf{q}'^{\mathbf{i}}(t+\Delta t)$ and $\mathbf{q}''^{\mathbf{i}}(t+\Delta t)$ before performing the actual estimation of $\mathbf{q}^{\mathbf{i}}(t+\Delta t)$. Here we used primed letters to indicate auxiliary variables that can be discarded at the end of the procedure.The algorithm is thus composed of the following steps:

- Use the current torques to update the angular momentum by a half timestep:

$$\mathbf{L}_{LAB}^i\left(t+\frac{1}{2}\Delta t\right)=\mathbf{L}_{LAB}^i(t)+\frac{1}{2}\Delta t\boldsymbol{\tau}_{LAB}^i(t). \tag{5.56}$$

- Use the updated angular momenta $\mathbf{L}_{LAB}^i\left(t+\frac{1}{2}\Delta t\right)$ and orientations $\mathbf{q}^i(t)$ to com-

pute the angular velocity for all particles at $\left(t+\frac{1}{2}\Delta t\right)$:

$$\boldsymbol{\omega}'^{i}{}_{LAB}\left(t+\frac{1}{2}\Delta t\right)=\mathbf{R}(\mathbf{q}^{i}(t))\left(\mathbf{I}^{i}{}_{MOL}\right)^{-1}\mathbf{R}(\mathbf{q}^{i}(t))^{T}\mathbf{L}^{i}_{LAB}\left(t+\frac{1}{2}\Delta t\right). \tag{5.57}$$

where $\mathbf{R}(\mathbf{q}^{i}(t))$ are the rotation matrices specified in (5.12).

- Use the angular velocity to compute the quaternion derivative using:

$$\dot{\mathbf{q}}'^{\mathbf{i}}\left(t+\frac{1}{2}\Delta t\right)=\frac{1}{2}\mathbf{S}\left(\boldsymbol{\omega}^{(4)\prime i}_{LAB}\left(t+\frac{1}{2}\Delta t\right)\right)\mathbf{q}(t). \tag{5.58}$$

- Carry out a full timestep integration of the quaternion derivative $\mathbf{q}'^{\mathbf{i}}(\mathbf{t})$:

$$\mathbf{q}'^{\mathbf{i}}(t+\Delta t)=\mathbf{q}'^{\mathbf{i}}(t)+\Delta t\dot{\mathbf{q}}'^{\mathbf{i}}\left(t+\frac{1}{2}\Delta t\right). \tag{5.59}$$

which completes the estimation of $\mathbf{q}'^{\mathbf{i}}(t+\Delta t)$.

- Compute the derivative of quaternions $\mathbf{q}''^{\mathbf{i}}$, using $\dot{\mathbf{q}}'^{\mathbf{i}}\left(t+\frac{1}{2}\Delta t\right)$ by half a timestep:

$$\mathbf{q}''^{\mathbf{i}}\left(t+\frac{1}{2}\Delta t\right)=\mathbf{q}^{\mathbf{i}}(t)+\frac{\Delta t}{2}\dot{\mathbf{q}}'^{\mathbf{i}}\left(t+\frac{1}{2}\Delta t\right). \tag{5.60}$$

- Use the new positions $\mathbf{q}''^{\mathbf{i}}\left(t+\frac{1}{2}\Delta t\right)$ to estimate the angular velocity:

$$\begin{aligned}\boldsymbol{\omega}''^{i}_{LAB}\left(t+\frac{1}{2}\Delta t\right)=&\mathbf{R}\left(\mathbf{q}''^{\mathbf{i}}\left(t+\frac{1}{2}\Delta t\right)\right)\left(\mathbf{I}^{i}{}_{MOL}\right)^{-1}\\&\times\mathbf{R}\left(\mathbf{q}''^{\mathbf{i}}\left(t+\frac{1}{2}\Delta t\right)\right)^{T}\mathbf{L}^{i}_{LAB}\left(t+\frac{1}{2}\Delta t\right).\end{aligned} \tag{5.61}$$

- Use the angular velocity to compute the derivative of quaternions by half a timestep:

$$\dot{\mathbf{q}}''^{\mathbf{i}}\left(t+\frac{1}{2}\Delta t\right)=\frac{1}{2}\mathbf{S}\left(\boldsymbol{\omega}^{(4)\prime\prime i}_{LAB}\left(t+\frac{1}{2}\Delta t\right)\right)\mathbf{q}''^{\mathbf{i}}\left(t+\frac{1}{2}\Delta t\right). \tag{5.62}$$

- The last half time step is performed in the quaternion

$$\mathbf{q}''^{\mathbf{i}}(t+\Delta t)=\mathbf{q}''^{\mathbf{i}}\left(t+\frac{1}{2}\Delta t\right)+\frac{1}{2}\Delta\dot{\mathbf{q}}''^{\mathbf{i}}\left(t+\frac{1}{2}\Delta t\right). \tag{5.63}$$

- Use the auxiliary quaternion $\mathbf{q}''^{\mathbf{i}}(t+\Delta t)$ and $\mathbf{q}'^{\mathbf{i}}(t+\Delta t)$ to compute the new

quaternions $\mathbf{q}^{\mathbf{i}}(t+\Delta t)$ for the last half timestep:

$$\mathbf{q}^{\mathbf{i}}(t+\Delta t) = 2\mathbf{q}''^{\mathbf{i}}(t+\Delta t) - \mathbf{q}'^{\mathbf{i}}(t+\Delta t). \tag{5.64}$$

In this process, each quaternion is re-normalized after any manipulation.

The random torque component was calculated by

$$\sigma^{r}_{\alpha,i} = \sqrt{2\gamma I^{mol}_{ij} k_B T}\,\delta \tag{5.65}$$

where δ is a uniform distribution with range [-0.5,0.5].

Chapter 6

Simulations of Active particles suspended in liquid crystals

In the previous chapter we developed the theory necessary for performing molecular simulations of active systems. A similar framework was used several times to study different models for active matter in the simpler case of two dimensions. For instance, the organization in 2 dimensions of living matter has been studied with the model pioneered by Viczek and with its variants [102–104]. A version of the Lennard-Jones soft potential in a (quasi)two-dimensional liquid was used to study agglomeration of isotropic active particles [105, 106], and a long range repulsive interaction model was also developed for the same reason [107]. However, in these cases the particles were constrained to move in a plane. In 3D, the segregation of active Brownian particles interacting by Weeks– Chandler–Andersen potential was studied by Stenhammar et al. [108].

In materials composed by anisotropic particles, Backwell et al developed a 2D model for motor driven liquid crystals and studied their hydrodynamics for different densities [109]. Segregation and clustering of (quasi)two-dimensional mixture of active and passive rods was studied by S.R. McCandlish et al. (low and high densities) [110]. However we did not find studies at microscopic level for active particles dissolved in liquid crystals in three dimensions, clearly the system of more obvious importance.

Here we wish to consider a fully 3D system and we investigate a sample composed of a mixture of "active" anisotropic particles capable of self propelling, and identical

but passive particles. The questions we ask are (i) if it is possible to get dynamic orientational order from a system which is isotropic at equilibrium and (ii) if not, if there are differences in the type of ordering or structuring upon activating the propelling force, when the phase at rest (when all particles are in their inactive state) is already nematic or smectic. In particular, does the activation destroy or enhance the order? Here we address the problem using the very successful Gay-Berne model, where as already mentioned, system of uniaxial or biaxial particles endowed with attractive and repulsive forces have shown able to generate isotropic, nematic and smectic.

6.1 Model parameters

More in detail to study effects due solely to the activity, we model the self-propelled rods with exactly the same physical parameters of length and interaction as the passive ones in the pair potential.

For the inter-particle interactions we have chosen the Gay-Berne parametrized by Berardi et. al [98], using $\mu = 1.0$, $\nu = 4$, $\epsilon_0 = 1$, $\sigma_e = 3.0$, $\sigma_s = 0.1$, $\epsilon_s = 1.0$, $\epsilon_e = 0.2$ and cutoff = 4.0 for both active and passive particles, where we employ the following set of dimensionless units: lengths are expressed in units of σ_s, masses in m, energies in ϵ_0, temperature in ϵ_0/k_B and time in $\sqrt{m_0\sigma^2/\epsilon_0}$. The remaining parameters are expressed as combinations of the previous ones.

Our samples have in total $N \approx 10000$ particles each, contained in a cubic box with periodic boundary conditions in all three dimensions. The length of the box edges are $L \approx 31\ \sigma_s$, giving a packing fraction of $\phi \approx 0.5$ and a density $\rho = 0.3$. The detailed lengths and number of particle for each will be discussed in a later section.

All simulations were performed in the NVT ensemble with the temperature controlled using a Langevin thermostat for both active and passive particles. Even though some properties might depend on the value of γ [111], here we will treat γ as a fixed parameter. We used $\gamma = \gamma_r = 1.0$ for all simulations, since it gave reasonable values for the sample temperature. When tested the value $\gamma = \gamma_r = 10$ gave an over damped regime, while the value $\gamma = \gamma_r = 0.1$ showed strong instabilities. Small variations of $\{\gamma, \gamma_r\}$ around the value 1 did not change the computed parameters sig-

nificantly.

We modelled activity by adding a constant self-propelling force f_s in the direction of the long axis of the active particles, as explained in section 5.3.2. Even though the Gay-Berne interaction is apolar (it does not distinguish ellipsoids heads and tails), the self-propelling force introduces polarity in the active particles. Finally, we used $\delta t = 0.01\ \sqrt{m_0\sigma^2/\epsilon_0}$ for the timestep and each simulation was performed typically for 4×10^6 timesteps.

The simulations were performed using the open source LAMMPS code, version 05/09/2014, which we have slightly modified to remove the friction and noise around the molecule symmetry axis and to add the self-propelled forces for active particles.

We performed a grid of simulations varying 3 parameters: thermostat temperature, concentration of active particles and self-propelled force intensity. We varied the active particles concentration p from 5% to 16% in steps of 1% and from 16% to 30% in steps of 2%. We chose the values of f_s to be 0.75 ϵ/σ, 1.5 ϵ/σ, 2.25 ϵ/σ and 3.0 ϵ/σ, and the thermostat temperature of $T = 2.1\ \epsilon_0/k_B$, $T = 3.0\ \epsilon_0/k_B$ and $T = 3.3\ \epsilon_0/k_B$ which yield a smectic liquid crystal, a well oriented nematic, a weak oriented nematic and an isotropic fluid, respectively. In total we run approximately 250 simulations over many months of work.

6.2 Sample preparation

To get as close as possible to simulate the effect of a liquid crystalline environment, we equilibrated our sample with the self-propelling force deactivated, and activated it only in the production run. As a consequence we could use the same initial conditions for all simulations with the same thermostat temperature T.

The starting structures for each sample were taken from a previous work [98]. In the present work, we replicated the samples 3 times on each direction x,y,z and performed an equilibration run for 2×10^6 timesteps. After that, we sliced the central cube of the simulation and re-equilibrated it for another 2×10^6. The details about the box sizes together with the number of particle in each sample can be seen in Tab. 6.1 and the snapshot of the starting configurations can be visualized in Fig. 6.1.

With the samples in thermodynamic equilibrium we chose randomly a fraction of

Table 6.1: Detailed information of box sizes $\sigma_i$and number of particles N for samples with different thermostats temperatures.

	Box length				
T	σ_x	σ_y	σ_z	$\langle P_2 \rangle$	N
2.10	31.705	31.705	31.7050	0.93	9561
3.00	31.950	31.9506	31.9506	0.73	9785
3.30	31.9376	31.9376	31.9376	0.66	9773
3.8	31.8972	31.8972	31.8972	0.12	9736

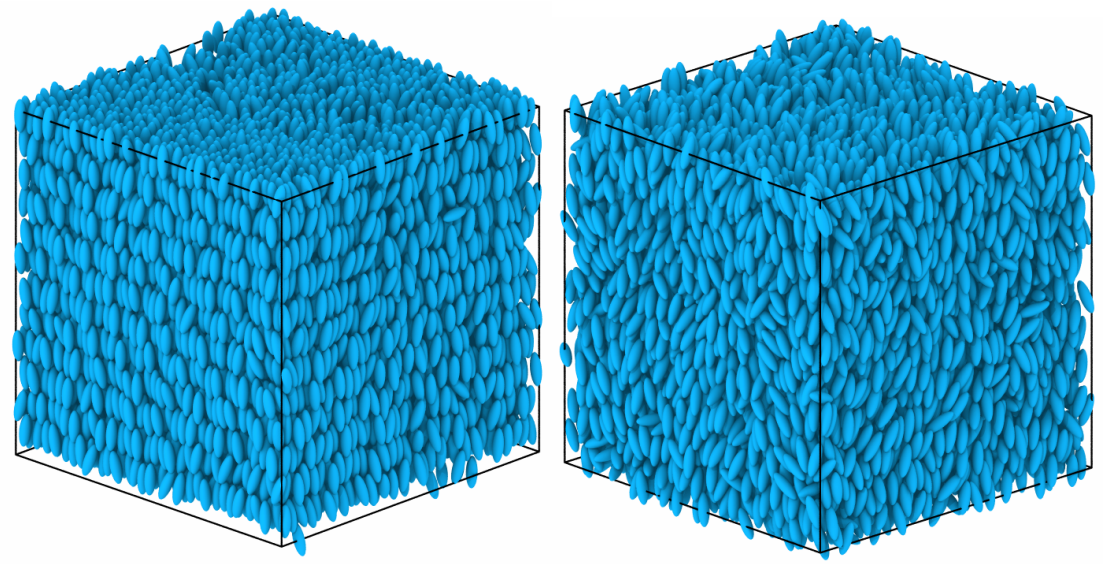

(a) $T = 2.10$ **(b)** $T = 3.00$

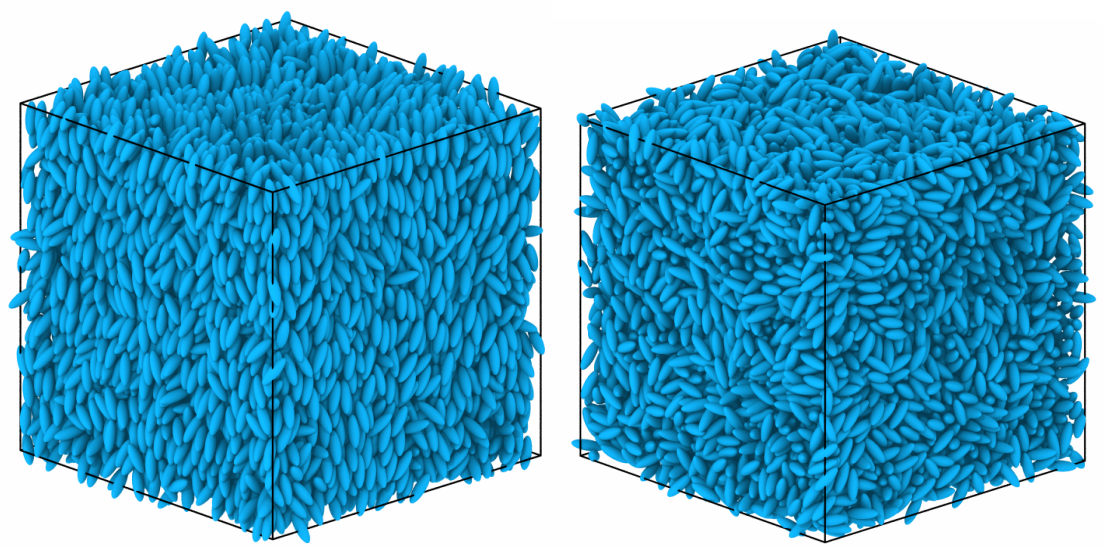

(c) $T = 3.30$ **(d)** $T = 3.80$

Figure 6.1: Starting configuration for different temperatures.

particles to be the active ones. The production runs were then performed assigning $f_s \neq 0$ to the active particles and $f_s = 0$ to the passive ones.

6.3 Results

6.3.1 Aggregation of self-propelled particles

Depending on the parameters $\{T, p, f_s\}$, after turning on the self-propelled force, the randomly dispersed active particles started to aggregate in clusters, which then further evolved to flowing particle lanes similar to the ones reported in [108]. An example can be visualized in Fig. 6.2.

The condition for the onset of the aggregation phenomenon depends on all three parameters studied: self-propelling force, thermostat temperature and concentration of active particles. In particular, force and thermostat temperature show a critical behaviour. We have found no aggregation for self-propelling force $f_s = 0.75\ \epsilon/\sigma$ nor in the isotropic phase, when temperatures was set $T = 3.8\ \epsilon_0/k_B$. Even performing a series of simulations with high concentrations (until $p = 50\%$) for $f_s = 0.75\ \epsilon/\sigma$, no aggregation was observed. There is also a concentration threshold for the aggregation phenomenon, however its value depends on both temperature and force.

The cluster formation shows a nucleation like dynamics. At the beginning of the aggregation, we have the formation of small clusters that grow independently of each other. During this process, clusters flowing in the same direction tend to fuse when they approach. Clusters can also divide in smaller ones, although this phenomenon happens less often. In this way, in most samples, after a sufficient amount of time, there will be two giant lanes, flowing in opposite directions. A series of snapshots illustrating these findings can be visualized in Fig. 6.3.

The only notable exceptions are the samples simulated with $f_s = 3.00\ \epsilon/\sigma$, where the giant lanes are not stable. In this case, the fast movement of the particles inside these lanes causes bending deformations which grow in time. The intensity of the deformations increases until the lane breaks into small clusters. These spare particles form new small clusters or are absorbed by the closest flock increasing its size. A sequence of snapshots showing this phenomenon can be observed in Fig. 6.4.

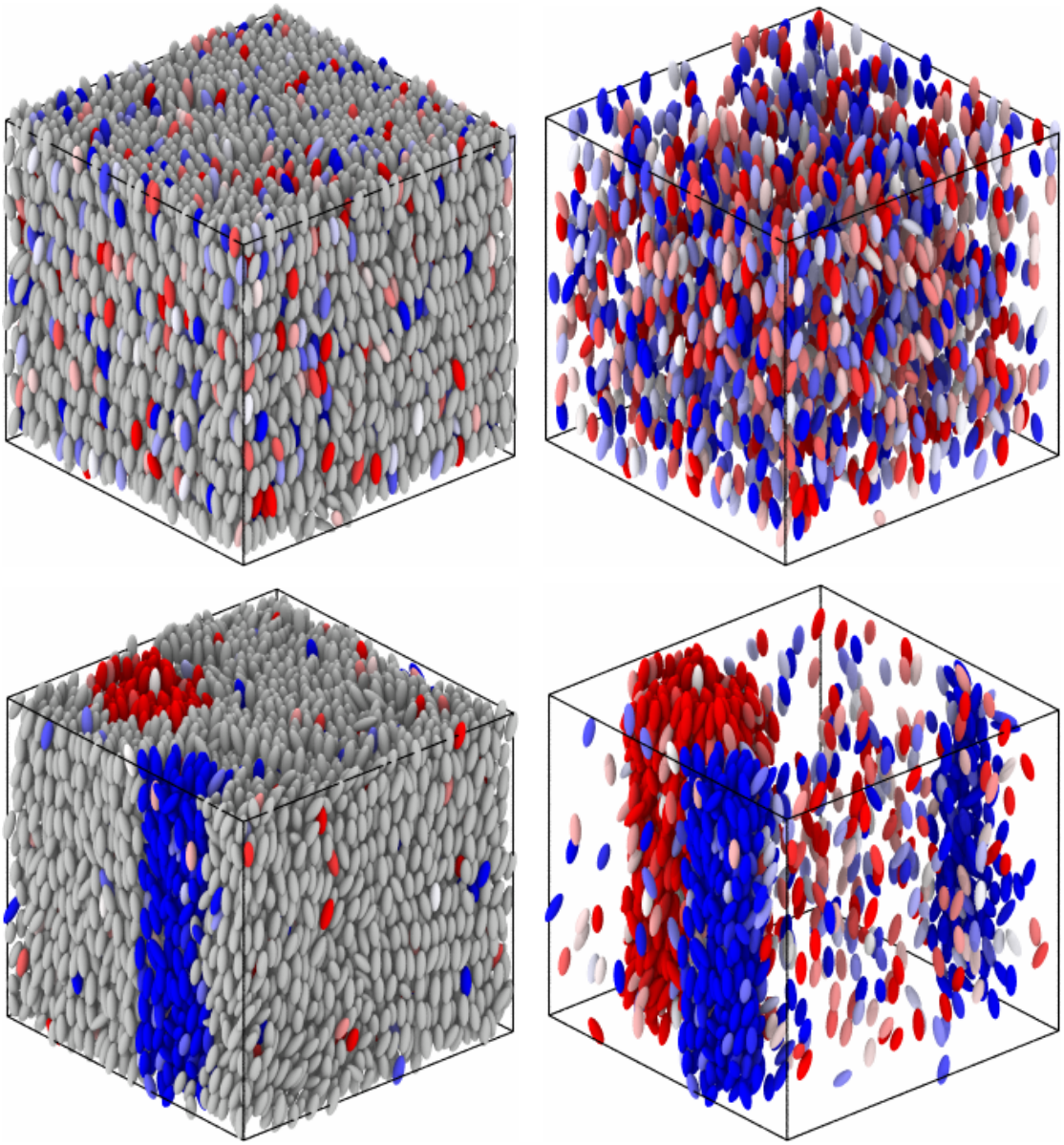

Figure 6.2: Lane formation for the system with parameters $f_s = 1.5\ \epsilon/\sigma$, $p = 20\%$ and $T = 2.1\ \epsilon_0/k_B$ at $t = 0\ \sqrt{m_0\sigma^2/\epsilon_0}$ (top left) and $t = 25000\ \sqrt{m_0\sigma^2/\epsilon_0}$ (bottom left). Passive particles are coloured in grey and self-propelled one in a scale of red-blue depending on the direction and intensity of the component $\hat{z}$ of the velocity. On the right hand side we report the same snapshots, $t = 0$ (top right) and $t = 25000\ \sqrt{m_0\sigma^2/\epsilon_0}$ (top left) with passive particles removed to facilitate the visualization.

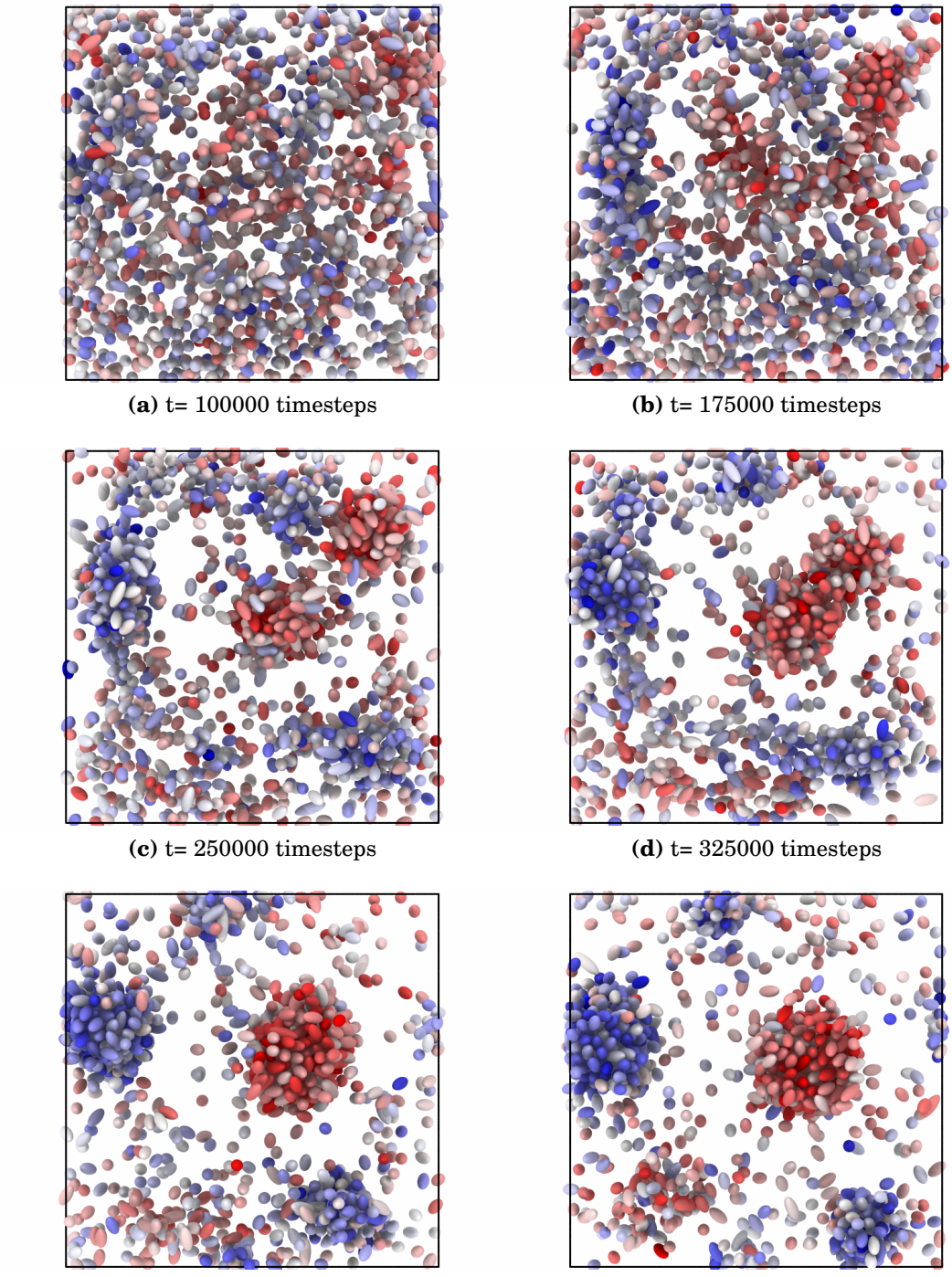

(a) t= 100000 timesteps

(b) t= 175000 timesteps

(c) t= 250000 timesteps

(d) t= 325000 timesteps

(e) t= 400000 timesteps

(f) t= 475000 timesteps

Figure 6.3: Top view of snapshots illustrating cluster formation. The simulation parameters were: $T = 2.10\ \epsilon_0/k_B$, $f_s = 2.25\ \epsilon/\sigma$ and $p = 16\%$. Particles that are moving upstream are coloured in blue while particles moving downstream were coloured in red,. For both cases the colours intensity were assigned following a scale depending on the value of v_z.

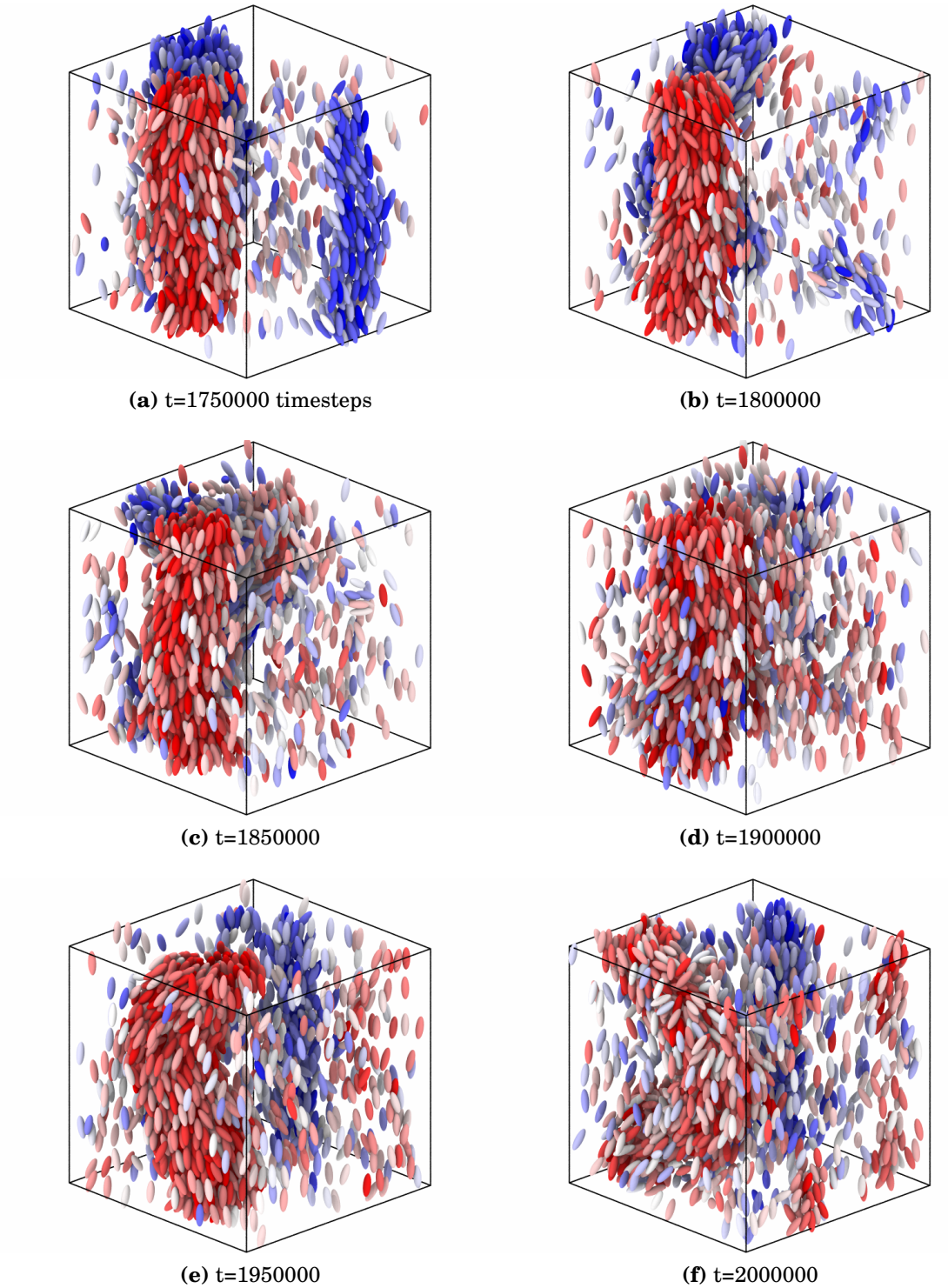

(a) t=1750000 timesteps

(b) t=1800000

(c) t=1850000

(d) t=1900000

(e) t=1950000

(f) t=2000000

Figure 6.4: Snapshots showing cluster bending. The figures were taken from the simulation with $T = 2.10\ \epsilon_0/k_B$, $f_s = 3.00\ \epsilon/\sigma$ and $p = 20\%$. Particles that are moving upstream are coloured in blue, while particles moving downstream were coloured in red,. For both cases the colour intensities were assigned following a scale depending on the value of v_z.

To analyse quantitatively the aggregation of active particles, we used a modified DBSCAN algorithm (the original version of the algorithm is reported in appendix A). Since each combination of $\{T, p, f_s\}$ produced clusters with different sizes and characteristics lengths, tuning the DBSCAN parameters to perform a proper division in all cases was no easy task. First, the phase is highly anisotropic due to the existence of the liquid crystal director and moreover our particles are anisotropic with a certain length to breadth ratio. As a consequence molecules positioned end–to–end are found at distances higher than the ones positioned side–by–side. Second, as we have seen, the clusters usually appears in pairs flowing in opposite directions. A classification taking into account solely the particles distances would recognize them as a single unit when they approach each other.

To overcome these problems, we found easier to set $minPoints = 1$ and to manipulate the metric function (see Appendix). We defined three different metrics D_i, each one involving a different couple of parameters with their respective threshold distances ϵ_i. A particle is considered connected to another if $D_i < \epsilon_i \; \forall \; i$, where

$$\begin{aligned} D_1(\mathbf{r}^i, \mathbf{r}^j) &= |\mathbf{r}^i - \mathbf{r}^j|^2, \\ D_2(\mathbf{u}^i, \mathbf{u}^j) &= -\mathbf{u}^i \cdot \mathbf{u}^j, \\ D_3(\mathbf{v}^i, \mathbf{v}^j) &= -\mathbf{v}^i \cdot \mathbf{v}^j. \end{aligned} \tag{6.1}$$

In the present work we used $\{\epsilon_1 = 3.5, \epsilon_2 = 0.0, \epsilon_3 = 0\}$.

To compare samples with different concentrations of self-propelling particles, we will present cluster sizes as the fraction of the number of active particles in the sample, expressed by:

$$X_i(t) = \frac{N_i(t)}{N_{active}}, \tag{6.2}$$

being N_i the number of active particles in the ith cluster and N_{active} the number of active particles in the system. Since tiny clusters can hinder the statistical analyses of the phenomenon, we discarded any cluster with number of particles smaller then 20. The time average of the cluster size can be visualized in figure 6.5.

The clusters formed at the temperature $T = 2.1 \; \epsilon_0/k_B$ are the most stable ones, also, they are bigger than the ones formed at $T = 3.00 \; \epsilon_0/k_B$ and at $T = 3.30 \; \epsilon_0/k_B$.

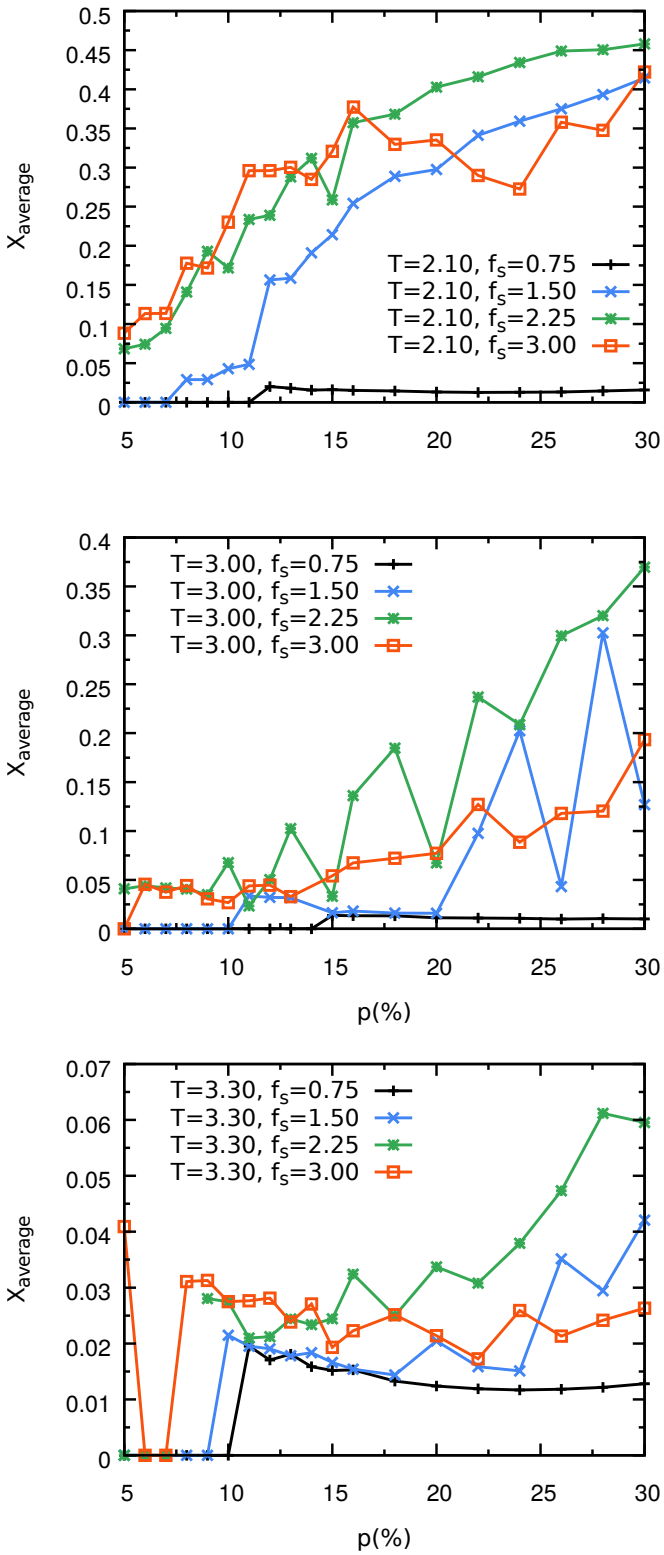

Figure 6.5: Average cluster size calculate from $t = 40000\ \sqrt{m_0\sigma^2/\epsilon_0}$ to $t = 50000\ \sqrt{m_0\sigma^2/\epsilon_0}$, with values taken every $t = 50\ \sqrt{m_0\sigma^2/\epsilon_0}$.

Table 6.2: Time averaged principal values of the gyration tensor. In table N_e is the number of clusters detected in the period, and the number in parenthesis is the standard deviation. Values extracted from simulations performed with $f_s = 1.5\ \epsilon/\sigma$ and $T = 2.10\ \epsilon_0/k_B$.

p	N_e	λ_1	λ_2	λ_3
7	0	0.00 (0.00)	0.00 (0.00)	0.00 (0.00)
8	4	0.98 (0.21)	3.26 (1.14)	19.31 (12.36)
9	46	0.96 (0.41)	2.54 (1.18)	17.04 (13.58)
10	74	0.91 (0.48)	2.63 (1.15)	18.40 (18.27)
11	523	2.02 (0.79)	4.00 (1.78)	52.87 (31.59)
12	424	2.84 (0.68)	4.62 (1.90)	75.24 (19.62)
13	421	3.01 (0.66)	4.52 (0.97)	76.85 (18.18)
14	400	3.58 (0.54)	5.81 (2.28)	82.25 (8.04)
15	404	3.90 (0.43)	5.33 (0.66)	82.28 (7.85)
16	402	4.47 (0.42)	5.91 (0.51)	82.97 (5.33)
22	402	6.80 (0.45)	8.19 (0.50)	83.55 (2.90)
28	400	8.92 (2.00)	11.82 (5.07)	83.59 (1.97)
30	400	10.41 (2.76)	12.60 (5.20)	83.80 (1.70)

The results also indicates that high concentrations favour aggregation in bigger clusters, rather than forming groups of smaller ones. Again we have an exception for the force $f_s = 3.00\ \epsilon/\sigma$ which shows a non monotonic behaviour with p and shows giant fluctuations (.i.e instabilities) for $p > 15\%$.

To study the cluster geometry, we calculated the distribution of self-propelled particles around the geometric centre of each cluster formed in the sample, given by the gyration tensor

$$S_{ij} = \frac{1}{2N^2} \sum_{k=1}^{N} \sum_{l=1}^{N} (r_i^k - r_i^l)(r_j^k - r_j^l) \tag{6.3}$$

where S_{ij} are the components of the gyration tensor, r_i^k is the ith position component of the kth particle and N the number of particles present in the cluster. The eigenvalues of the gyration tensor λ_i give the shape of the distribution of particles around the axis given by the associated eigenvector. The eigenvalues averaged over the number of cluster and time are reported in table 6.2.

We can identify two different transitions, the first happening at $p = 8\%$, marking the formation of the first clusters, and the second at $p = 11\%$, where there is a jump in the number of clusters and their geometry. These points will be used to divide our data into regions that we will analyse separately. The region between $p = 8\%$ and $p = 11\%$ possesses a small number of small clusters, which are organized with

no clear shape $\lambda_1 \neq \lambda_2 \neq \lambda_3$. The leading dimension λ_3 is usually oriented along the liquid crystal director. Even though we have just 4 cluster at $p = 8\%$, the trend repeats itself in the region $p = 10 \sim 11\%$, allowing us to make this inference.

The second phase transition shows a change in the cluster geometry, where the aggregates increased in all sizes, being the leading dimension the one that growth the most. Also, the flock shape shows a clear cylindrical geometry $\lambda_1 \approx \lambda_2 < \lambda_3$.

6.3.2 Ordering and activity

Berardi et al. [98] described the ordering of a passive sample with the same parameters of the ones presented here, however, the introduction of active particles can change the phase behaviour and the order parameter.

In order to investigate this effect, we need a precise definition of the thermodynamic parameters involved. However, the definition of temperature in active systems is non trivial, since it is difficult to distinguish the coherent motion induced by the activity from the random thermal movement. For this reason, we computed the temperature just for the passive particles. Also, in out-of-equilibrium simulations it is important to distinguish between the thermostat temperature T and the sample temperature T_s.

The self-propelling force introduces energy into the system that is not removed instantaneously, increasing the medium temperature [111, 112]. If we assume the equipartition theorem to hold for the passive particles, their temperature can be calculated from the following expression

$$T_s(t) = \frac{1}{6N_{\text{pas}}} \sum_{i=1}^{N_{\text{pas}}} \left(\frac{\mathbf{p}^i(t) \cdot \mathbf{p}^i(t)}{2m^i} + \frac{\boldsymbol{\omega}^i_{MOL}(t) \mathbf{I}^i_{MOL} \boldsymbol{\omega}^i_{MOL}(t)}{2} \right), \tag{6.4}$$

where the summation is performed over all passive particles N_{pas}. Here we are going to monitor only the passive particles temperature, in this way, we avoid the mentioned problems.

The ordering of both active and passive particles can be quantified by the order parameter $\langle P_2 \rangle$. To compute $\langle P_2 \rangle$, first we calculate the order tensor $\mathbf{Q}_{ij}$ whose com-

ponents are given by

$$Q_{ij} = \frac{1}{N}\left(\sum_{k=1}^{N} \hat{u}_i^k \hat{u}_j^k - \frac{1}{3}\delta_{i,j}\right), \tag{6.5}$$

where u_i^k are the components of the unit vector aligned with the symmetry axis of the kth particle and defining its orientation. The order parameter at a given time can be computed by

$$P_2 = \frac{3}{2}\max(\lambda_1, \lambda_2, \lambda_3) \tag{6.6}$$

being λ_i the eigenvalues of $\mathbf{Q}$.

To distinguish the possible self-organization of both active and passive particles in the system, we calculated their order parameter separately. The time averaged order parameter, for both active and passive particles, as a function of active particles concentration p can be seen in Fig. 6.6.

We can notice that the increase the self propelled force intensity or active particle concentration, reduces the order in both active and passive particles. Comparing the results for the various choices of parameters, we see that the order reduction is more dependent on the self-propelling force intensity, while concentration plays a secondary role. For lower to intermediate forces ($f_s < 3.00$), as we increase concentration the order parameter saturates at plateau. However, when $f_s = 3.00$, the order parameter decays faster and does not shows the same saturation point.

We attribute the order reduction in the passives particles to the increase in the sample temperature. A scatter plot showing the dependence of the order parameter on the sample temperature for both active and passive particles can be seen on Fig 6.7.

In the passive particles plot, points with the same temperature have close values of order parameter $\langle P_2 \rangle$, independent of the self-propelling force intensity. This supports our argument that the rise in the sample temperature is the reason of the reduction of order parameter of the passive particles.

The same evidence is not valid for the active particles. We can observe that there is a reduction of order coupled with increase of temperature, however, for intermediate forces ($f_s = 1.5$ and $f_s = 2.25$) there is a saturation point where the temperatures increases, but is not accompanied by a decrease in the order parameter.

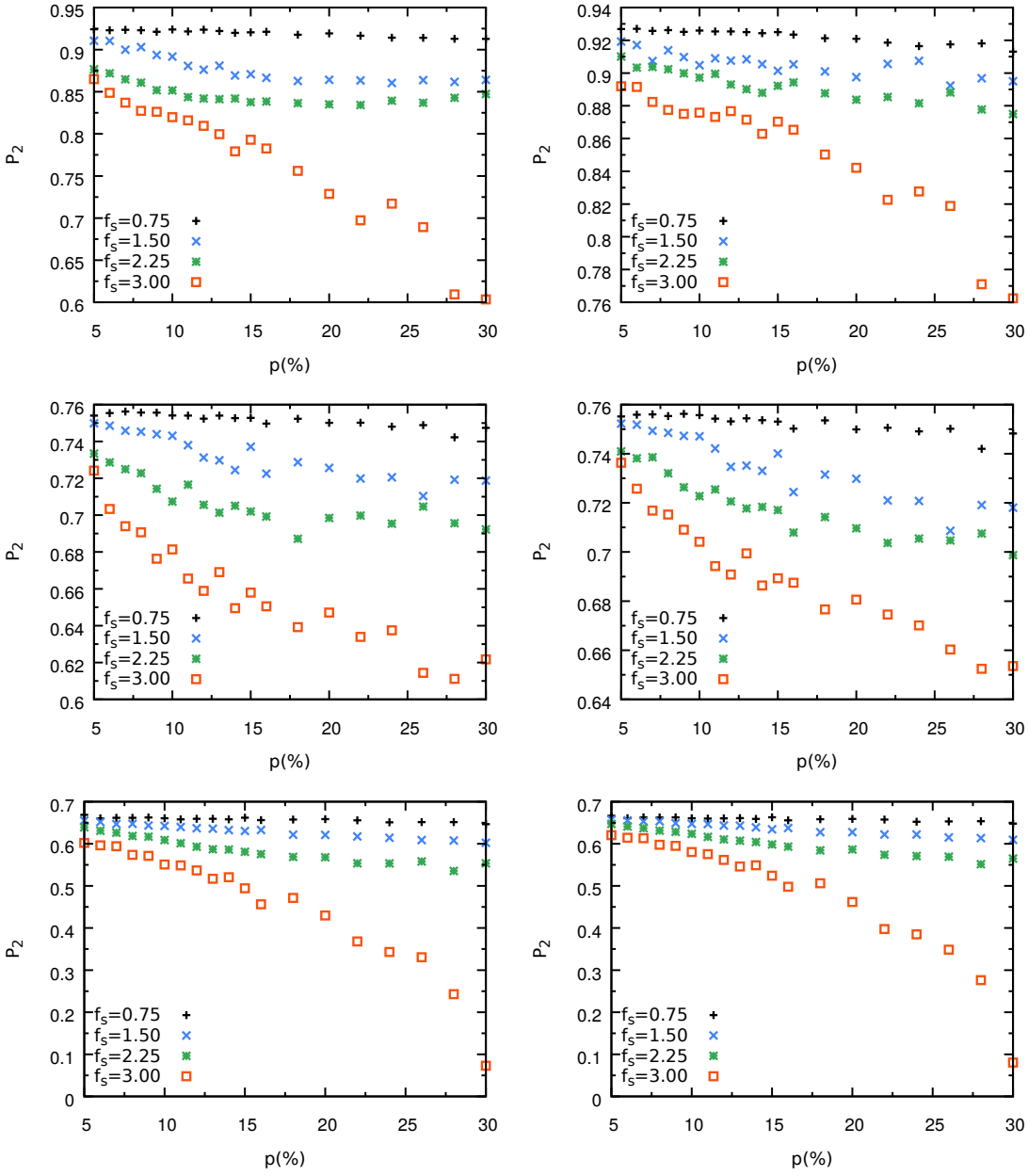

Figure 6.6: Time averaged order parameter $\langle P_2 \rangle$ as a function of active particles concentration calculated separately for active (left) and passive particles (right) and for the temperatures $T = 2.10\ \epsilon_0/k_B$ (top), $T = 3.00\ \epsilon_0/k_B$ (middle) and $T = 3.30\ \epsilon_0/k_B$ (top). For the average we have taken snapshots from $t = 40000\ \sqrt{m_0\sigma^2/\epsilon_0}$ until $t = 50000\ \sqrt{m_0\sigma^2/\epsilon_0}$ in steps of $\Delta t = 50\ \sqrt{m_0\sigma^2/\epsilon_0}$. With self-propelling set to 0 ($f_s = 0$) the sample temperature is $T_s = 2.10\ \epsilon_0/k_B$ and the order parameter is $\langle P_2 \rangle = 0.93$.

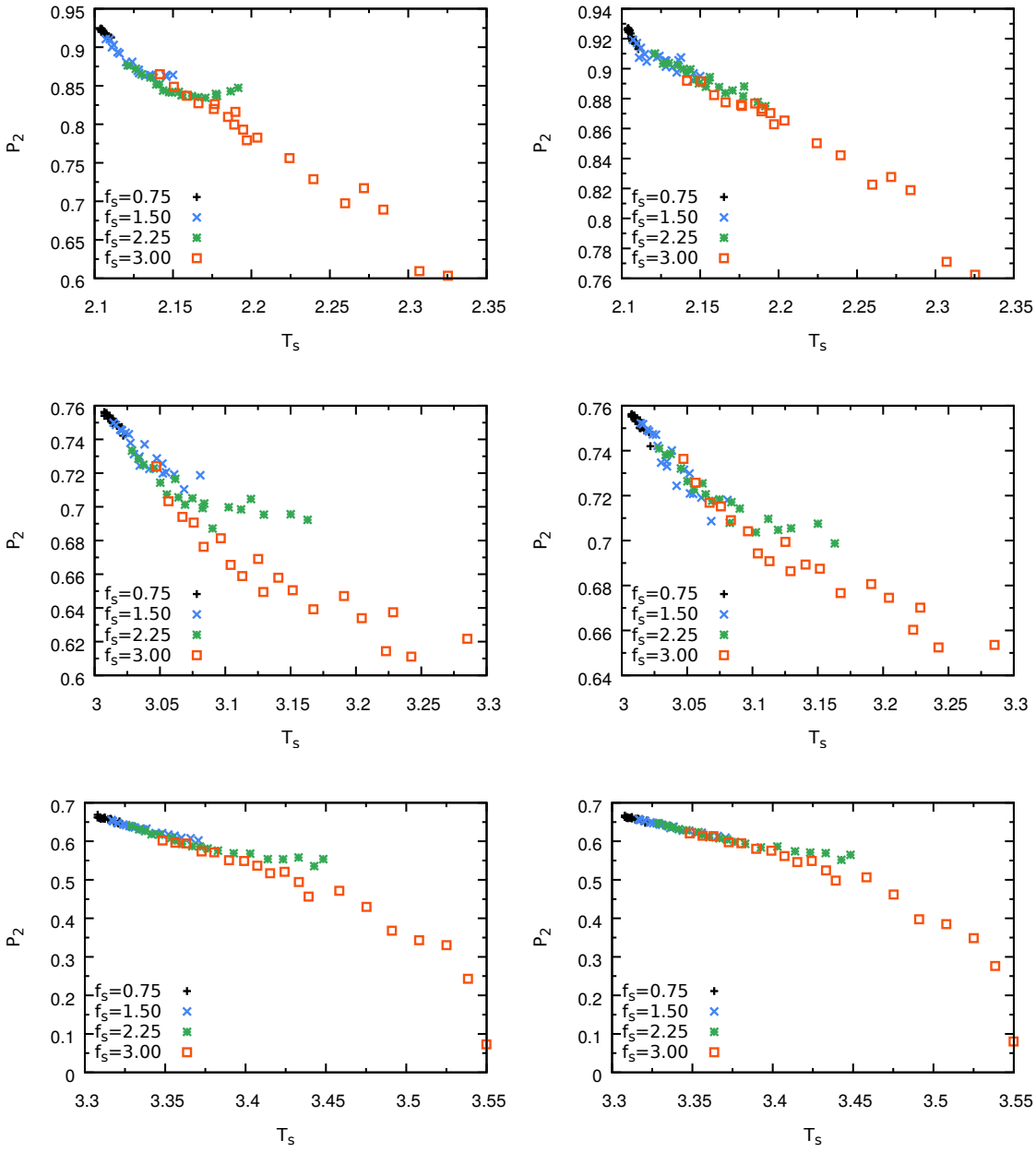

Figure 6.7: Time averaged order parameter $\langle P_2 \rangle$ for the active (top) and passive (bottom) for the temperatures $T = 2.10\ \epsilon_0/k_B$ (left) and $T = 3.00\ \epsilon_0/k_B$ (right). For the average we have taken snapshots from $t = 40000\ \sqrt{m_0\sigma^2/\epsilon_0}$ until $t = 50000\ \sqrt{m_0\sigma^2/\epsilon_0}$ in steps of $\Delta t = 50\ \sqrt{m_0\sigma^2/\epsilon_0}$. Without the self-propelling force the sample temperature is $T_s = 2.10\ \epsilon_0/k_B$ and the order is $\langle P_2 \rangle = 0.93$.

The usual order parameter provide information on how the system is ordered, but another useful information that we can extract is how the velocities are ordered. Here we define the velocity ordering tensor as

$$\widehat{\mathbf{V}}_{ij} = \frac{1}{N}\left(\sum_{k=1}^{N} \hat{v}_i^k \hat{v}_j^k - \frac{1}{3}\delta_{i,j}\right), \tag{6.7}$$

where v_i^k is the ith component of the kth particle velocity unit vector. We can obtain the velocity order parameter is by

$$P_{2v} = \frac{3}{2}\max(\lambda_1^v, \lambda_2^v, \lambda_3^v) \tag{6.8}$$

being λ_i^v the eigenvalues of the velocity order tensor. We can use this parameter to decouple movement noise from coherent movement. We calculated the velocity order parameter as a function of time and the time-averaged velocity order parameter for the active particles in our system, the results can be visualized in Fig. 6.8.

When $f_s = 0.75$, the velocity order is close to 0 indicating that particles movements are due exclusively to thermal noise and thermal collisions, this behavior is sustained independent of the concentration of the active particles. Increasing the force to $f_s = 1.5$, we have exactly the same behavior for simulations with low concentration p of active particles, but after the threshold $p = 11\%$ there is a increase in $\langle P_{2v} \rangle$. This is surprising, since we already have cluster formations at $p = 10 \sim 11\%$ but not coherent velocity orientation. This suggests that the clusters formation do not depends on the velocity alignment.

For higher forces $f_s = 2.25$ and $f_s = 3.00$ we have $\langle P_{2v} \rangle \neq 0$ for all studied concentrations, even for the cases where there is no clustering,which reinforces our argument that the clustering do not need velocity alignment

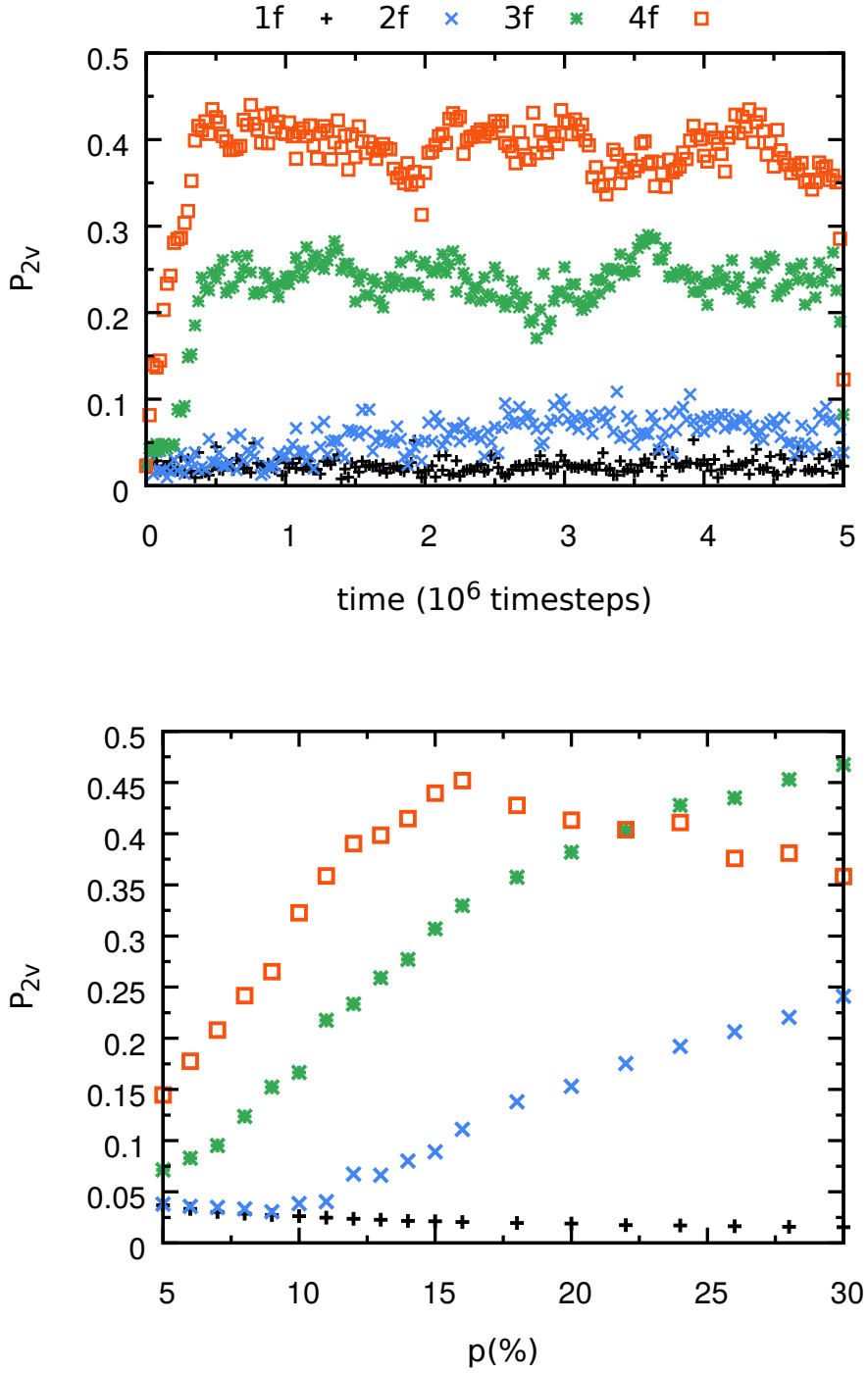

Figure 6.8: Velocity/Dynamic order parameter (top) and average Velocity/Dynamic order parameter $\langle P_{2v} \rangle$ (bottom) for concentration for p=12%. We start the averaging process after 2×10^6 timesteps and finishes it after another 2×10^6 timsteps taking values every 50000 timesteps.

Chapter 7

Concluding Remarks

7.1 Shape Changing particles

In the first part of the thesis we proposed a simple model to describe the roto-diffusion of a shape changing particle in an anisotropic environment. We developed the mathematical formalism and operators and numerically solved the system of equations obtained for two cases: a uniaxial particle dissolved in a uniaxial and a biaxial liquid crystal phase. The solutions can be used to calculate correlation functions and correlation times depending on the changes in the orientations or in the shape of the particles.

For the uniaxial case, we analysed the correlation times for a probe particle which can assume three shapes. For exchange rates much smaller than the rotational diffusion coefficient, the correlation functions of the probe particle are the weighted average of the individual correlation functions of each rigid shape.

We also analysed the relation between the shape exchange rate and the correlation times and noticed that increasing the shape exchange rate decreases the correlation times until a certain limiting value is reached. The limiting value depends on the intrinsic distribution of shapes.

For the biaxial case, we developed a completely different numerical procedure. The new approach is mathematical more cumbersome, however, it is more efficient for numerical calculations.

We solved an example of a particle which can assume the three distinct shapes and we analysed how the biaxiality of environment affects the time dependence of

some selected correlation functions. We also identified in which case we can perform the uniaxial approximation without loss of information.

Even though we used a small discrete set of shapes in both cases, the model can be easily generalized to the quasi continuum case by increasing the number of shapes to be taken into account and by adding some restrictions to the operator $k_{\chi,\nu}(x)$. The same procedure can be used to take into account fluctuations in the particle orientation that can happen during the shape changing process.

We hope that the availability of a theory for the interpretation of spectroscopic data for particles reorienting and changing shape while being embedded in a fluid anisotropic environment will stimulate experimental investigations as was the case e.g. for rigid biaxial particles where experiments (see, e.g. [30, 113]) followed the development of a theoretical framework.

In future work we plan to extend the formalism to include particles with arbitrary shape and also develop a explicit framework for particles that change shape continuously instead of doing discrete jumps.

7.2 Active particles

In the second part of the present thesis, we have studied self-propelled particles dispersed in a isotropic liquid and, more importantly, smectic and nematic liquid crystal phases. We modelled all particles as Gay-Berne ellipsoids, where the active particles were also endowed with a constant force along their symmetry axis.

We observed that active particles can aggregate and flow in coherent lanes when certain conditions are met. The sizes and geometry of the lanes depends on both the self-propelled particle concentration and self-propelling force. Interestingly, the size of the stable lanes formed in the sample decays fast as we increase the temperature. This suggest that in this specific system, the order of the host is essential to the formation of lanes.

We also studied the ordering of the active and passive particles. We found that the introduction of energy by the activity increases the temperature of the host, which in turn disorder it. The order of the active particles is also reduced as we increase the activity, however, it decays slower than the passive ones. Furthermore, for the sam-

ples simulated with the thermostat temperature set to $T = 2.10\ \epsilon_0/k_B$, we identified a limiting value for the decrease in the order parameter, suggesting that the active particles can organize themselves differently than the passive ones.

In future works, we plan to repeat the simulations with the same system parameters, however, this time with the sample composed only of active particles. In this way we hope to understand if the host order is strictly necessary for the formation of lanes. We also plan to extend our model to simulate other kind of systems, for instance, increasing the size of the active particles to make them behave more like colloids or a Janus particle.

We also have the intention to add a feedback force in a manner similar to the one done by Viczek. In this way we should be able to extend our model to simulate living matter in three dimensions as well.

Appendix A

Clustering with DBSCAN

One interesting characteristic of active systems is to display a collective behaviour leading to phenomena like: self-assembly, aggregation in clusters or phase separation. Even though these phenomena can be qualitatively identified by visual inspection in trajectories computed from molecular dynamics simulations, the quantitative study of these phenomena relies on clustering algorithms. The importance of big data grew enormously in recent years. With it, the array of clustering techniques became a science by itself, whose main interest is to recognize patterns in data mixed with noise. There is a wide range of techniques at stake, but all of them need some information on the system, for instance, the K-means clustering [114] divides the system in a pre-defined number of clusters, which needs to be defined *a priori*.

In our case, we may know the number of clusters at one point of the simulation by visual inspection, however this number may change over time. Moreover, during the simulation there may be particles that do not belong to any cluster, and need to be treated as noise. The most suitable algorithm available in this scenario is the GDBSCAN (Generalized Density Based Spatial Clustering of Applications with Noise) [115,116], which groups data into clusters based on the density of data, in our case using the density of particles in space.

Before looking at how GDBSCAN works, we need to make some definitions. Given a metric function $D(p_1, p_2)$ that computes the distance between two data points p_1 and p_2, we can define a neighbour region of p_1, here called $N(p_1)$, as one containing all points which satisfy

$$D(p_1, p_2) < \epsilon \tag{A.1}$$

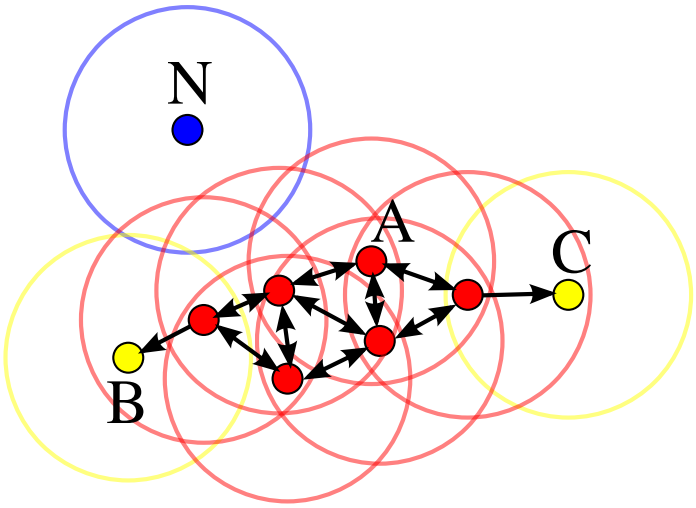

Figure A.1: Graphical example of the concepts at the base of the DBSCAN algorithm. Setting $min_{\text{Points}} = 3$, we have: Core points in red, border point sin yellow and noise points in blue. Notice that the border points B and C are not core points themselves, but they are density reachable from from A, therefore, they belong to the same cluster. Figure provided by Chire (Own work) [CC BY-SA 3.0 (http://creativecommons.org/licenses/by-sa/3.0)], via Wikimedia Commons

where ϵ is a chosen threshold value for the distance. We now define a core point, which is any point with a number of neighbouring points $|N(p_1)|$ satisfying

$$|N(p_1)| > min_{\text{Points}} \tag{A.2}$$

where the min_{Points} is an integer number given as input to the algorithm.

Following the nomenclature introduced by Ester et al. [115], we call a particle p_2 "directly density reachable" from p_1 if: p_1 is a core particle and p_2 belongs to p_1 neighbourhood. Also, we call a particle p_n "density reachable" from p_1 if there is a chain of directly density-reachable particles $\{p_2, p_3..p_{N-1}\}$, from which p_1 and p_n are directly density reachable from one of its members. Finally, a point p_i that is density reachable from a core p_j, but it is not a core in itself, is called a border point. A graphical representation of the concepts used in DBSCAN is given in Figure A.1.

GDBSCAN is an algorithm to separate a database into a set of density reachable points, given a distance ϵ and a minimum of points min_{Points}. The procedure can be visualized as a flow chart in figure A.2 and explained below.

1. A list of neighbours $N(p_i)$ is computed for a point p_i, chosen randomly from the database composed of all points.

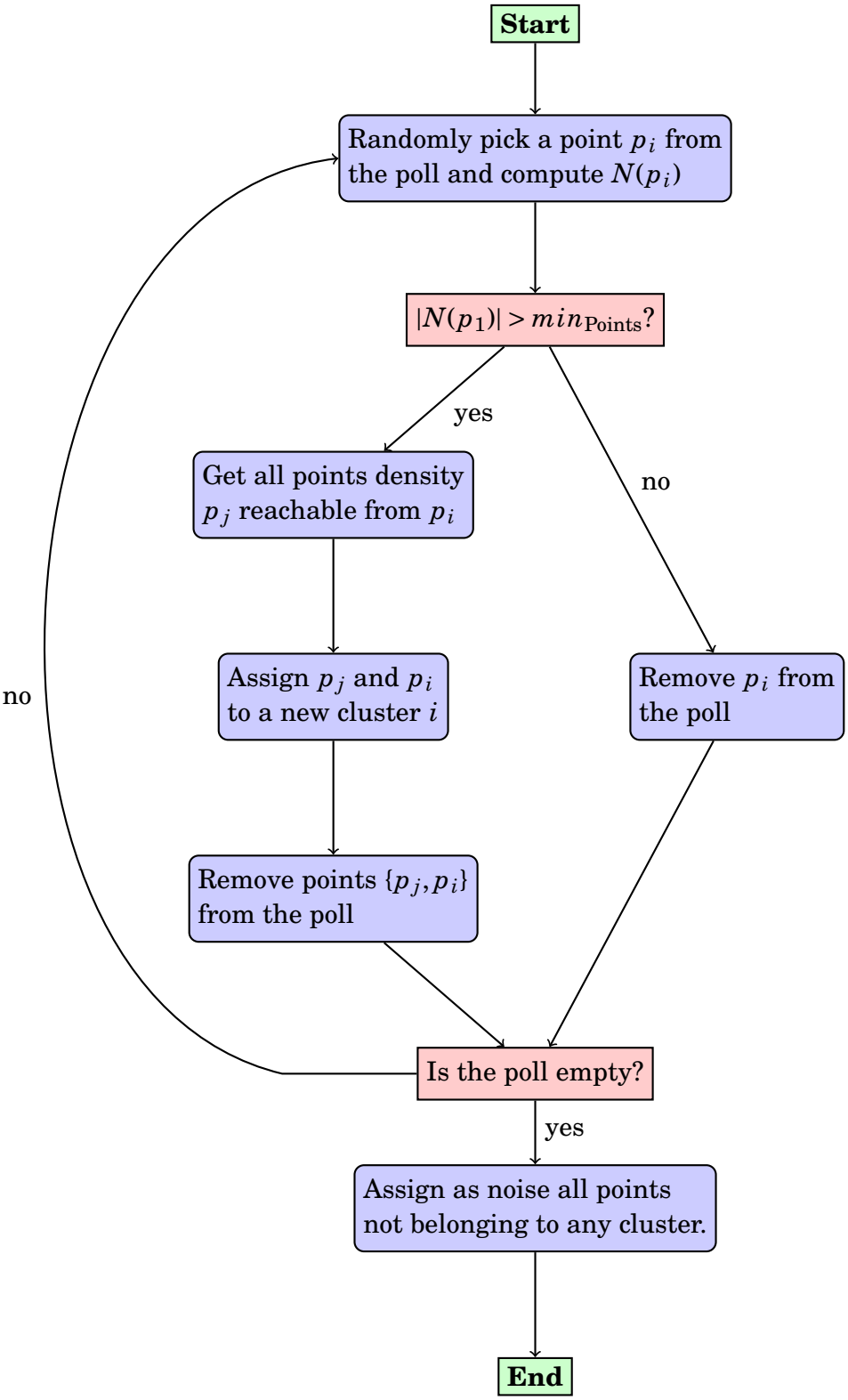

Figure A.2: Flow chart for the DBSCAN algorithm.

2. If p_i is not a core point, e.g. $|N(p_1)| < min_{\text{Points}}$, remove p_i from the database and restart the process at (1). If p_i is a core point, assign a new cluster cluster index i to p_i and remove it from the database.

3. For each one of the reaming points which $p_j \in N(p_i)$, assign to it the same index a and calculates it's neighbourhood $N(p_j)$.

4. If any p_j is a core point, take each element of $N(p_j)$ and repeat the process. The process is repeated until all points in all neighbourhoods are examined and no more core points were found. Assign the same cluster index i to the core points and to the points in its neighbourhood.

5. Remove from the database all points which had a cluster index assigned to them.

6. If there still points in the database, restart procedure at (1). If not, assign any point without a cluster index as noise and terminate the algorithm.

All core points are assigned in a deterministic way to their respective cluster. However, in the original version the border points can be assigned differently depending on the order with which the particles are chosen. This issue can be solved by adding a second stage to the algorithm [117]. Now, whenever we identify a border point, instead of assigning it to a index, we will move it to a second database (border database) and proceed as usual. At the end of the algorithm, when all core points are already assigned to their respective clusters, we can decide if to assign the border points to the clusters detected, for example, we can assign a point to the cluster containing the closest core point. This procedure generates clusters in a deterministic way [117].

The DBSCAN algorithm have some characteristics which we would like to remark. All clusters have at least min_{Points} points since every cluster has at least one core point. Due to its ability to handle noise separately from the cluster, GDBSCAN produces robust results which are not affected by the presence of outlying points.

References

[1] P. G. de Gennes and J. Prost, *The Physics of Liquid Crystals*. Oxford University Press, 1993.

[2] H. K. Bisoyi and S. Kumar, "Liquid-crystal nanoscience: an emerging avenue of soft self-assembly.," *Chemical Society Reviews*, vol. 40, pp. 306–319, 2011.

[3] R. J. Cox, "Liquid Crystal Guest-Host Systems," *Molecular Crystals and Liquid Crystals*, vol. 55, pp. 1–32, 1979.

[4] M. D. Lynch and D. L. Patrick, "Organizing Carbon Nanotubes with Liquid Crystals," *Nano Letters*, vol. 2, pp. 1197–1201, 2002.

[5] K. J. Wu, K. C. Chu, C. Y. Chao, Y. F. Chen, C. W. Lai, C. C. Kang, C. Y. Chen, and P. T. Chou, "CdS nanorods imbedded in liquid crystal cells for smart optoelectronic devices," *Nano Letters*, vol. 7, pp. 1908–1913, 2007.

[6] S. Zhou, A. Sokolov, O. D. Lavrentovich, and I. S. Aranson, "Living liquid crystals.," *Proceedings of the National Academy of Sciences of the United States of America*, vol. 111, pp. 1265–70, 2014.

[7] S. Hernàndez-Navarro, P. Tierno, J. A. Farrera, J. Ignés-Mullol, and F. Sagués, "Reconfigurable Swarms of Nematic Colloids Controlled by Photoactivated Surface Patterns," *Angewandte Chemie International Edition*, vol. 53, pp. 10696–10700, 2014.

[8] Q. Liu, C. Beier, J. Evans, T. Lee, S. He, and I. I. Smalyukh, "Self-alignment of dye molecules in micelles and lamellae for three-dimensional imaging of lyotropic liquid crystals," *Langmuir*, vol. 27, pp. 7446–7452, 2011.

[9] J.-W. Yoo and S. Mitragotri, "Polymer particles that switch shape in response to a stimulus," *Proceedings of the National Academy of Sciences of the United States of America*, vol. 107, pp. 11205–11210, 2010.

[10] J. E. Marshall, S. Gallagher, E. M. Terentjev, and S. K. Smoukov, "Anisotropic colloidal micromuscles from liquid crystal elastomers.," *Journal of the American Chemical Society*, vol. 136, pp. 474–9, 2014.

[11] M. Conradi, M. Ravnik, M. Bele, M. Zorko, S. Žumer, and I. Muševič, "Janus nematic colloids," *Soft Matter*, vol. 5, p. 3905, 2009.

[12] P. H. Colberg, S. Y. Reigh, B. Robertson, and R. Kapral, "Chemistry in Motion: Tiny Synthetic Motors," *Accounts of Chemical Research*, vol. 47, pp. 3504–3511, 2014.

[13] V. Narayan, S. Ramaswamy, and N. Menon, "Long-Lived Giant Number Fluctuations," *Science*, vol. 317, pp. 105–108, 2007.

[14] I. Buttinoni, J. Bialké, F. Kümmel, H. Löwen, C. Bechinger, and T. Speck, "Dynamical clustering and phase separation in suspensions of self-propelled colloidal particles," *Physical Review Letters*, vol. 110, pp. 1–5, 2013.

[15] L. T. Muus and P. W. Atkins, eds., *Electron Spin Relaxation in Liquids*. New York: Plenum Press, 1972.

[16] B. J. Berne and R. Pecora, *Dynamic Light Scattering*. New York: Dover, 2000.

[17] W. Haase and S. Wrobel, eds., *Relaxation Phenomena*. Berlin: Springer, 2003.

[18] G. R. Luckhurst and e. Veracini (eds), C. A., *The Molecular Dynamics of Liquid Crystals*. C. A. Dordrecht: Kluwer, 2012.

[19] P. L. Nordio and U. Segre, "Rotational diffusion," in *The Molecular Physics of Liquid Crystals* (G. R. Luckhurst and G. Gray, eds.), pp. 411–426, London: Academic Press, 1979.

[20] W. H. Furry, "Isotropic rotational Brownian motion," *Physical Review*, vol. 107, pp. 7–13, 1957.

[21] L. D. Favro, "Theory of the rotational Brownian motion of a free rigid body," *Physical Review*, vol. 119, pp. 53–62, 1960.

[22] P. L. Nordio and P. Busolin, "Electron Spin Resonance line shapes in partially ordered systems," *The Journal of Chemical Physics*, vol. 55, pp. 5485–5490, 1971.

[23] C. F. Polnaszek and J. H. Freed, "Electron-Spin Resonance studies of anisotropic ordering, spin relaxation, and slow tumbling in liquid-crystalline solvents," *The Journal of Chemical Physics*, vol. 79, pp. 2283–2306, 1975.

[24] J. H. Freed, "Theory of slow tumbling ESR spectra for nitroxides," in *Spin Labeling. Theory and Applications* (L. J. Berliner, ed.), pp. 53–132, New York: Academic Press, 1976.

[25] G. R. Luckhurst, M. Setaka, and C. Zannoni, "Electron Spin Resonance investigation of molecular motion in the smectic mesophase of a liquid crystal," *Molecular Physics*, vol. 28, pp. 49–68, 1974.

[26] A. Arcioni, F. Bertinelli, R. Tarroni, and C. Zannoni, "Time resolved fluorescence depolarization in a nematic liquid crystal," *Molecular Physics*, vol. 61, pp. 1161–1181, 1987.

[27] E. Berggren, R. Tarroni, and C. Zannoni, "Rotational diffusion of uniaxial probes in biaxial liquid crystal phases," *The Journal of Chemical Physics*, vol. 99, pp. 6180–6200, 1993.

[28] R. Tarroni and C. Zannoni, "On the rotational diffusion of asymmetric molecules in liquid- crystals," *The Journal of Chemical Physics*, vol. 95, pp. 4550–4564, 1991.

[29] E. Berggren and C. Zannoni, "Rotational diffusion of biaxial probes in biaxial liquid- crystal phases," *Molecular Physics*, vol. 85, pp. 299–333, 1995.

[30] S. Huo and R. R. Vold, "Deuterium NMR relaxation study of fluorene-d(10) in licristal-phase-5," *The Journal of Chemical Physics*, vol. 99, pp. 12391–12400, 1995.

[31] R. Y. Dong, *Nuclear Magnetic Resonance of Liquid Crystals*. New York: Springer, 1997.

[32] A. Arcioni, M. A. M. J. van Zandvoort, P. Bartolini, R. Torre, R. Tarroni, R. Righini, and C. Zannoni, "Effective shape and the dynamics of chlorophyll A in a nematic liquid crystal," *The Journal of Physical Chemistry B*, vol. 102, pp. 1624–1631, 1998.

[33] A. Loman, I. Gregor, C. Stutz, M. Mund, and J. Enderlein, "Measuring rotational diffusion of macromolecules by fluorescence correlation spectroscopy.," *Photochemical & Photobiological Sciences*, vol. 9, pp. 627–36, 2010.

[34] C. M. Pieper and J. Enderlein, "Fluorescence correlation spectroscopy as a tool for measuring the rotational diffusion of macromolecules," *Chemical Physics Letters*, vol. 516, pp. 1–11, 2011.

[35] Orville-Thomas, ed., *Internal Rotations in Molecules*. London: Wiley, 1974.

[36] C. Zannoni, "An internal order parameter formalism for non-rigid molecules," in *Nuclear Magnetic Resonance of Liquid Crystals* (J. Emsley, ed.), vol. 141, pp. 35–52, Dordrecht: Reidel, 1985.

[37] D. Torchia, "NMR studies of dynamic biomolecular conformational ensembles," *Progress in Nuclear Magnetic Resonance Spectroscopy*, vol. 84, pp. 14–32, 2015.

[38] N. J. Zabusky, E. Segre, J. Deschamps, V. Kantsler, and V. Steinberg, "Dynamics of vesicles in shear and rotational flows: Modal dynamics and phase diagram," *Physics Fluids*, vol. 23, p. 041905, 2011.

[39] J. Deschamps, V. Kantsler, and V. Steinberg, "Phase diagram of single vesicle dynamical states in shear flow," *Physical Review Letters*, vol. 102, p. 118105, 2009.

[40] S. Bolisetty, M. Hoffmann, S. Lekkala, T. Hellweg, M. Ballauff, and L. Harnau, "Coupling of rotational motion with shape fluctuations of core-shell microgels having tunable softness," *Macromolecules*, vol. 42, pp. 1264–1269, 2009.

[41] J. Crassous, A. Mihut, L. Mansson, and P. Schurtenberger, "Anisotropic responsive microgels with tuneable shape and interactions," *Nanoscale*, vol. 7, pp. 15971–15982, 2015.

[42] A. Viallat and M. Abkarian, "Red blood cell: from its mechanics to its motion in shear flow," *International Journal of Laboratory Hematology*, vol. 36, pp. 237–243, 2014.

[43] J. L. McWhirter, H. Noguchi, and G. Gompper, "Ordering and arrangement of deformed red blood cells in flow through microcapillaries," *New Journal of Physics*, vol. 14, p. 085026, 2012.

[44] V. Wong, D. A. Case, and A. Szabo, "Influence of the coupling of interdomain and overall motions on NMR relaxation.," *Proceedings of the National Academy of Sciences of the United States of America*, vol. 106, pp. 11016–11021, 2009.

[45] Y. Ryabov, G. M. Clore, and C. D. Schwieters, "Coupling between internal dynamics and rotational diffusion in the presence of exchange between discrete molecular conformations," *The Journal of Chemical Physics*, vol. 136, p. 034108, 2012.

[46] C. Kim, S. Mukherjee, P. Luchette, and P. Palffy-Muhoray, "Director orientation in deformed liquid crystal elastomer microparticles," *Soft Mater.*, vol. 12, pp. 159–165, 2014.

[47] Y. Zhao and T. Ikeda, eds., *Smart Light-Responsive Materials. Azobenzene Containing Polymers and Liquid Crystals*. Hoboken, NJ: Wiley, 2009.

[48] G. Tiberio, L. Muccioli, R. Berardi, and C. Zannoni, "How does the trans-cis photoisomerization of azobenzene take place in organic solvents?," *ChemPhysChem*, vol. 11, pp. 1018–1028, 2010.

[49] C. Zannoni, "Liquid crystal observables. static and dynamic properties," in *Advances in the Computer Simulations of Liquid Crystals* (P. Pasini and C. Zannoni, eds.), vol. 545, pp. 17–50, Dordrecht: Kluwer, 2000.

[50] M. E. Rose, *Elementary Theory of Angular Momentum*. New York: Wiley, 1967.

[51] L. Reichl, *A Modern Course in Statistical Physics*. Wiley, 1998.

[52] L. Muccioli and C. Zannoni, "A deformable Gay-Berne model for the simulation of liquid crystals and soft materials," *Chemical Physics Letters*, vol. 423, pp. 1–6, 2006.

[53] I. B. Bischofs, S. A. Safran, and U. S. Schwarz, "Elastic interactions of active cells with soft materials," *Physical Review E*, vol. 69, p. 021911, 2004.

[54] C. Zannoni, "A theory of time dependent fluorescence depolarization in liquid crystals," *Molecular Physics*, vol. 38, pp. 1813–1827, 1979.

[55] P. Pasini and C. Zannoni, "Tables of Clebsch - Gordan coefficients for integer angular momentum j=0-6," tech. rep., INFN, 1984.

[56] P. L. Nordio, G. Rigatti, and U. Segre, "Dielectric relaxation theory in nematic liquids," *Molecular Physics*, vol. 25, pp. 129–136, 1973.

[57] R. Gordon and T. Messenger, "Magnetic resonance line shapes in slowly tumbling molecules," in *Electron Spin Relaxation in Liquids* (L. T. Muus and P. W. Atkins, eds.), pp. 387–537, New York: Plenum Press, 1972.

[58] G. Moro, P. L. Nordio, and U. Segre, "ESR lineshapes of free radicals undergoing jump diffusion," *Gazzetta Chimica Italiana*, vol. 109, pp. 585–588, 1979.

[59] G. R. Luckhurst, "Molecular field theories of nematics," in *The Molecular Physics of Liquid Crystals* (G. Gray and G. Luckhurst, eds.), pp. 85–119, London: Academic Press, 1979.

[60] D. Catalano, C. Forte, C. A. Veracini, and C. Zannoni, "The orientational ordering of some non cylindrically symmetric solutes in nematic solvents.," *Israel J. Chem.*, vol. 23, pp. 283–289, 1983.

[61] R. N. Zare, *Angular Momentum. Understanding Spatial Aspects in Chemistry and Physics*. New York: Wiley, 1988.

[62] R. Berardi, F. Spinozzi, and C. Zannoni, "A multitechnique maximum entropy approach to the determination of the orientation and conformation of flexible molecules in solution," *The Journal of Chemical Physics*, vol. 109, pp. 3742–3759, 1998.

[63] C. Bacchiocchi, M. Brunelli, and C. Zannoni, "Energy Transfer and Orientational Dynamics," *Chemical Physics Letters*, vol. 336, pp. 253–261, 2001.

[64] R. Luckhurst, G, C. Zannoni, P. L. Nordio, and U. Segre, "A molecular field theory for uniaxial nematic liquid crystals formed by non-cylindrically symmetric molecules," *Molecular Physics*, vol. 30, pp. 1345–1358, 1975.

[65] R. L. Humphries, P. G. James, and G. R. Luckhurst, "Molecular field treatment of liquid crystalline mixtures," *Faraday Society Symposia*, vol. No. 5, pp. 107–118, 1971.

[66] G. R. Luckhurst and C. Zannoni, "Theory of dielectric relaxation in anisotropic systems," *Proceedings of the Royal Society A*, vol. 343, pp. 389–398, 1975.

[67] A. Sihvola, "Dielectric polarization and particle shape effects," *J. Nanonaterials*, p. 45090, 2007.

[68] H. C. Andersen, D. Chandler, and J. D. Weeks, "Roles of repulsive and attractive forces in liquids: the equilibrium theory of classical fluids," *Advances in Chemical Physics*, vol. 34, pp. 105–156, 1976.

[69] E. E. Burnell and C. A. de Lange, "Prediction from molecular shape of solute orientational order in liquid crystals," *Chemical Reviews*, vol. 98, pp. 2359–2387, 1998.

[70] S. Orlandi, E. Benini, I. Miglioli, D. Evans, V. Reshetnyak, and C. Zannoni, "Nanoparticle suspensions in nematics. a computer simulations study," *Physical Chemistry Chemical Physics*, vol. 18, pp. 2428–2441, 2016.

[71] F. Perrin, "Mouvement brownien d'un ellipsoide - I. Dispersion diélectrique pour des molécules ellipsoidales," *J. Phys. Radium*, vol. 5, pp. 497–511, 1934.

[72] S. H. Koenig, "Brownian motion of an ellipsoid. A correction to Perrin's results," *Biopolymers*, vol. 14, pp. 2421–2423, 1975.

[73] G. Miller, *Numerical Analysis for Engineers and Scientists*. Cambridge University Press, 2014.

[74] M. C. Marchetti, J. F. Joanny, S. Ramaswamy, T. B. Liverpool, J. Prost, M. Rao, and R. A. Simha, "Hydrodynamics of soft active matter," *Reviews of Modern Physics*, vol. 85, pp. 1143–1189, 2013.

[75] J. Parrish and W. Hamner, *Animal Groups in Three Dimensions: How Species Aggregate*. Psychiatry and Medicine, Cambridge University Press, 1997.

[76] G. de Magistris and D. Marenduzzo, "An introduction to the physics of active matter," *Physica A: Statistical Mechanics and its Applications*, vol. 418, pp. 65–77, 2014.

[77] A. Baskaran and M. C. Marchetti, "Nonequilibrium statistical mechanics of self-propelled hard rods," *Journal of Statistical Mechanics: Theory and Experiment*, vol. 2010, P04019, 2010.

[78] A. Baskaran and M. C. Marchetti, "Enhanced diffusion and ordering of self-propelled rods," *Physical Review Letters*, vol. 101, pp. 1–4, 2008.

[79] A. Ahmadi, T. B. Liverpool, and M. C. Marchetti, "Nematic and polar order in active filament solutions," *Physical Review E*, vol. 72, pp. 4–7, 2005.

[80] A. Baskaran and M. C. Marchetti, "Self-regulation in self-propelled nematic fluids," *European Physical Journal E*, vol. 35, 2012.

[81] R. Suzuki, C. a. Weber, E. Frey, and A. R. Bausch, "Polar pattern formation in driven filament systems requires non-binary particle collisions," *Nature Physics*, vol. 11, pp. 839–843, 2015.

[82] J. Toner and Y. Tu, "Long-range order in a two-dimensional dynamical XY model: How birds fly together," *Physical Review Letters*, vol. 75, pp. 4326–4329, Dec 1995.

[83] J. Toner and Y. Tu, "Flocks, herds, and schools: A quantitative theory of flocking," *Physical Review E*, vol. 58, pp. 4828–4858, Oct 1998.

[84] M. L. Blow, S. P. Thampi, and J. M. Yeomans, "Biphasic, Lyotropic, Active Nematics," *Physical Review Letters*, vol. 113, 248303, 2014.

[85] S. Čopar, M. Ravnik, and S. Žumer, "Janus nematic colloids with designable valence," *Materials*, vol. 7, pp. 4272–4281, 2014.

[86] L. Giomi, M. J. Bowick, P. Mishra, R. Sknepnek, and M. C. Marchetti, "Defect dynamics in active nematics," *Philosophical Transactions of the Royal Society A*, vol. 372, p. 20130365, 2014.

[87] D. Frenkel and B. Smit, *Understanding Molecular Simulation: From Algorithms to Applications*. Elsevier Science, 2001.

[88] M. Allen and D. Tildesley, *Computer Simulation of Liquids*. Oxford University Press, 1989.

[89] H. Goldstein, C. Poole, and J. Safko, *Classical Mechanics*. Addison Wesley, 2002.

[90] M. Tuckerman, *Statistical Mechanics: Theory and Molecular Simulation*. Oxford University Press, 2010.

[91] A. M. Menzel, "Tuned, driven, and active soft matter," *Physics Reports*, vol. 554, pp. 1–45, 2015.

[92] J. W. Ponder and D. A. Case, "Force fields for protein simulations," *Advances in Protein Chemistry*, vol. 66, pp. 27–85, 2003.

[93] S. L. Altmann, *Rotations, Quaternions, and Double Groups*. Oxford University Press, 1986.

[94] R. Berardi and C. Zannoni, "Computer Simulations of Biaxial Nematics," in *Biaxial Nematic Liquid Crystals*, pp. 153–184, Wiley, mar 2015.

[95] T. F. Miller, M. Eleftheriou, P. Pattnaik, A. Ndirango, D. Newns, and G. J. Martyna, "Symplectic quaternion scheme for biophysical molecular dynamics," *Journal of Chemical Physics*, vol. 116, pp. 8649–8659, 2002.

[96] J. G. Gay and B. J. Berne, "Modification of the Overlap Potential to Mimic a Linear Site-Site Potential," *The Journal of Chemical Physics*, vol. 74, pp. 3316–3319, 1981.

[97] R. Berardi, C. Fava, and C. Zannoni, "A Gay–Berne potential for dissimilar biaxial particles," *Chemical Physics Letters*, vol. 297, pp. 8–14, 1998.

[98] R. Berardi, A. P. J. Emerson, and C. Zannoni, "Monte Carlo investigations of a Gay-Berne liquid crystal," *Journal of the Chemical Society, Faraday Transactions*, vol. 89, pp. 4069–4078, 1993.

[99] G. R. Luckhurst, R. A. Stephens, and R. W. Phippen, "Computer simulation studies of anisotropic systems . XIX . Mesophases formed by the Gay-Berne model mesogen," *Liquid Crystals*, vol. 8, pp. 451–464, 1990.

[100] S. K. Das, S. a. Egorov, B. Trefz, P. Virnau, and K. Binder, "Phase behavior of active swimmers in depletants: Molecular dynamics and integral equation theory," *Physical Review Letters*, vol. 112, pp. 1–5, 2014.

[101] B. Dunweg and P. Wolfgang, "Brownian Dynamics without gaussian random numbers," *International Journal of Modern Physics*, vol. 2, pp. 817–827, 1991.

[102] A. Czirók and T. Vicsek, "Collective behavior of interacting self-propelled particles," *Physica A*, vol. 281, pp. 17–29, 2000.

[103] H. Chaté, F. Ginelli, G. Grégoire, F. Peruani, and F. Raynaud, "Modeling collective motion: Variations on the Vicsek model," *European Physical Journal B*, vol. 64, pp. 451–456, 2008.

[104] H. Chaté, F. Ginelli, G. Grégoire, and F. Raynaud, "Collective motion of self-propelled particles interacting without cohesion," *Physical Review E*, vol. 77, pp. 1–15, 2008.

[105] Y. Fily, S. Henkes, and M. C. Marchetti, "Freezing and phase separation of self-propelled disks.," *Soft Matter*, vol. 10, pp. 2132–40, 2014.

[106] Y. Fily and M. C. Marchetti, "Athermal phase separation of self-propelled particles with no alignment," *Physical Review Letters*, vol. 108, pp. 1–5, 2012.

[107] E. Mani and H. Löwen, "Effect of self-propulsion on equilibrium clustering," *Physical Review E*, vol. 92, p. 032301, 2015.

[108] J. Stenhammar, D. Marenduzzo, R. J. Allen, and M. E. Cates, "Phase behaviour of active Brownian particles: the role of dimensionality.," *Soft Matter*, vol. 10, pp. 1489–99, 2014.

[109] R. Blackwell, O. Sweezy-Schindler, C. Baldwin, L. E. Hough, M. Glaser, and M. D. Betterton, "Microscopic origins of anistropic active stress in motor-driven nematic liquid crystals," *Soft Matter*, vol. 12, pp. 2676–2687, 2015.

[110] S. R. McCandlish, A. Baskaran, and M. F. Hagan, "Spontaneous segregation of self-propelled particles with different motilities," *Soft Matter*, vol. 8, p. 2527, 2012.

[111] D. Loi, S. Mossa, and L. F. Cugliandolo, "Effective temperature of active matter," *Physical Review E*, vol. 77, pp. 1–4, 2008.

[112] D. Loi, S. Mossa, and L. F. Cugliandolo, "Effective temperature of active complex matter," *Soft Matter*, vol. 7, pp. 3726–3729, 2011.

[113] R. Y. Dong and X. Shen, "Rotational diffusion of asymmetric molecules in liquid crystals: A global analysis of deuteron relaxation data," *The Journal of Chemical Physics*, vol. 105, pp. 2106–2111, 1996.

[114] R. Xu and D. C. Wunsch, *Clustering*. Wiley, 2009.

[115] M. Ester, H.-P. Kriegel, J. Sander, and X. Xu, "A Density-Based Clustering Algorithm for Discovering Clusters in Large Spatial Database with Noise," *KDD-96 Proceedings*, pp. 226–231, 1996.

[116] J. Sander, M. Ester, H. P. P. Kriegel, and X. Xu, “Density-based clustering in spatial databases: The algorithm GDBSCAN and its applications,” *Data Mining and Knowledge Discovery*, vol. 194, pp. 169–194, 1998.

[117] T. N. Tran, K. Drab, and M. Daszykowski, “Revised DBSCAN algorithm to cluster data with dense adjacent clusters,” *Chemometrics and Intelligent Laboratory Systems*, vol. 120, pp. 92–96, 2013.